Multiwavelength Studies of X-ray Bright Extragalactic Jets

Leith Edward Hope Godfrey

A thesis submitted for the degree of

Doctor of Philosophy

of The Australian National University

Research School of Astronomy & Astrophysics

May 2009

To my Family.

Disclaimer

I hereby declare that the work in this thesis is that of the candidate alone, except where indicated below or in the text of the thesis.

Chapter 3 has been published as a paper in *The Astrophysical Journal*, 2009, Vol. 695, pg. 707. This paper is co-authored by G. V. Bicknell, J. E. J. Lovell, D. L. Jauncey, J. Gelbord, D. A. Schwartz, H. L. Marshall, M. Birkinshaw, M. Georganopoulos, D. W. Murphy, E. S. Perlman and D. M. Worrall. The paper is the candidate's own work, except for §3.3.1 and Figure 3.4, which were contributed by J. Gelbord.

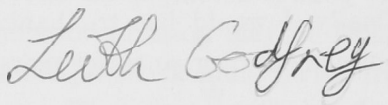

Leith E. H. Godfrey
May 2009

Acknowledgments

I would like to thank my supervisors Geoff Bicknell, Jim Lovell and Dave Jauncey for all their guidance, advice and support over the course of the PhD. I would also like to thank Dan Schwartz, an external advisor to this thesis, for sponsoring a visit to Boston and teaching me the techniques of working with *Chandra* X-ray data.

I am grateful to the ANU Research School of Astronomy and Astrophysics, the Australia Telescope National Facility and the Grote Reber Foundation for financial support.

To my friends here at Mount Stromlo (past and present), thanks for all the good times and breaking the drudgery of the PhD.

To Katie, thank you for your constant support, patience, understanding and encouragement.

Finally, I would like to thank my family for such tremendous support and encouragement over so many years. Without you I would never have made it this far.

Abstract

This thesis comprises two major pieces of work. The first is a study of the radio, optical and X-ray emission from the z=0.663 broad line radio galaxy PKS 1421–490. Long Baseline Array imaging of this object reveals a 400 pc diameter high surface brightness hotspot at a projected distance of approximately 40 kpc from the active galactic nucleus. The isotropic X-ray luminosity of the hotspot, $L_{2-10\,\mathrm{keV}} = 3 \times 10^{44}\,\mathrm{ergs\,s^{-1}}$, is comparable to the isotropic X-ray luminosity of the entire X-ray jet of PKS 0637–752, and the peak radio surface brightness is hundreds of times greater than that of the brightest hotspot in Cygnus A. We model the radio to X-ray spectral energy distribution using a one-zone synchrotron self Compton model with a near equipartition magnetic field strength of 3 mG. There is a strong brightness asymmetry between the approaching and receding hotspots and the hot spot spectrum remains flat ($\alpha \approx 0.5$) well beyond the predicted cooling break for a 3 mG magnetic field, indicating that the hotspot emission may be Doppler beamed. A high plasma velocity beyond the terminal jet shock could be the result of a dynamically important magnetic field in the jet. There is a significant change in the slope of the hotspot radio spectrum at GHz frequencies, which we model by incorporating a cut-off in the electron energy distribution at $\gamma_{\mathrm{min}} \approx 650$, with higher values implied if the hotspot emission is Doppler beamed. We show that a sharp decrease in the electron number density below a Lorentz factor of 650 would arise from the dissipation of bulk kinetic energy in an electron/proton jet with a Lorentz factor $\Gamma_{\mathrm{jet}} \gtrsim 5$.

The second major piece of work is a study of the radio, optical and X-ray emission from the core, jet, hotspot and lobes of the quasar PKS 2101–490. An Fe Kα emission line is observed in the X-ray spectrum of the quasar core, with redshift $z = 1.07 \pm 0.02$. This result is consistent with the "tentative redshift" of z=1.04 claimed by Marshall et al. (2005) based on an optical spectrum from the Magellan telescope. We construct radio to X-ray spectral energy distributions for seven distinct regions along the 13″ jet, and model the X-ray emission in terms of inverse Compton scattering of the cosmic microwave background (IC/CMB). We find that the jet remains highly relativistic hundreds of kpc from the nucleus, with bulk Lorentz factor $\Gamma \sim 8$. The radio to optical spectrum of the brightest X-ray knot is well modeled by a broken power law with a cooling break at $\nu_b \approx 8 \times 10^{12}$ Hz. The observed break frequency is consistent with the predictions of a shock model for the knot in which the jet has bulk Lorentz factor $\Gamma \sim 9$ and is in a state of equipartition between magnetic and particle energy densities. However, we find that the size of the X-ray knot is no greater than the size of the radio knot. This observation may be inconsistent with models involving a single shock in a continuous flow.

In order to provide an additional constraint on models of jet X-ray emission, we combine the observed hotspot parameters with the equations for the conser-

vation of energy and momentum across a strong shock to estimate the jet energy flux. We compare this estimate with the jet energy flux derived from IC/CMB modeling of jet X-ray emission, and find that in the case of a leptonic jet, the two energy flux estimates ($L_j \sim 10^{46}$ ergs/s) are comparable, but in the case of an electron/proton plasma, the energy flux estimate from IC/CMB modeling ($L_j \sim 10^{48}$ ergs/s) is nearly two orders of magnitude greater than the estimate based on the hotspot parameters. There are a number of ways to interpret this result. It may provide evidence in favour of an electron/positron jet, or it may be indicative of the inadequacies of the one-zone IC/CMB model for quasar jet X-ray emission.

Contents

List of Figures

List of Tables

Chapter 1

Introduction

Active galaxies are a class of galaxy in which a significant fraction of the radiated energy is associated with a small bright region at the galactic centre, known as an "active galactic nucleus", or AGN. In some cases, the energy radiated by the AGN can exceed that of the host galaxy's stellar light by several orders of magnitude. The radiation from AGN is believed to be the result of accretion of matter onto a supermassive black hole at the centre of the host galaxy. A sub class of active galaxies, known as radio galaxies, produce highly collimated beams, or jets, of relativistic magnetized plasma that emit strongly at radio wavelengths. In some cases the jets extend several Mpc from the host galaxy, making them the largest known objects in our universe. The scales involved and the energy associated with radio galaxies are truly incomprehensible, and their images are some of the most beautiful and intriguing in all of astronomy (see, for example, Figures 1.2 and 1.3). Radio galaxies are a fascinating phenomenon worth studying in their own right, but the study of radio galaxies also has a much broader context. The energetic jets of relativistic plasma ejected from active galactic nuclei have a strong and lasting impact on their host galaxies and the surroundings, and jet production may influence the growth of the central super-massive black hole. Here I present a brief introduction to radio galaxies from an historical perspective in order to introduce the main concepts and illustrate where this thesis fits into the ~ 60 year history of the study of radio galaxies[1]. I then present a more detailed discussion of some topics relevant to the thesis.

1.1 Radio Galaxies: An Historical Perspective

The discovery of radio emission associated with astronomical objects was somewhat of an accident. Karl Jansky, an employee of Bell Telephone Laboratories, was given the task of investigating sources of static that interfered with transatlantic telephone services. Using a large, purpose built antenna operating at 20 MHz,

[1]A detailed history of the study of active galactic nuclei is given by Shields (1999).

Jansky discovered three major sources of static: nearby thunderstorms, distant thunderstorms, and a steady hiss of unknown origin (Jansky, 1932). Further investigation revealed that the steady hiss was of extraterrestrial origin, and the strongest static came from the direction of the centre of the Milky Way (Jansky, 1933). This discovery marked the beginning of radio astronomy. Grote Reber designed and constructed the first purpose built radio telescope, operating at 160 MHz with a resolution of $\sim 3^\circ$ (Reber, 1940). Reber confirmed the association of strong radio emission with the Milky Way, and also discovered a number of "minor maxima" of cosmic radio emission, one of which was in the direction of the constellation Cygnus (Reber, 1944). The rapid advancement of radar and radio technology during World War II had a great effect on radio astronomy. After the war, the improved radio technology was employed to study the recently discovered "cosmic noise". Hey et al. (1946) discovered a discrete source in the constellation Cygnus. This was the first detection of the now famous archetypal radio galaxy Cygnus A. Bolton & Stanley (1948) observed this discrete source of radio emission using a sea-cliff interferometer and set an upper limit of $8'$ to the source diameter. They calculated the brightness temperature to be more than 4×10^6 K at 100 MHz, and predicted that the radio emission was therefore unlikely to be of thermal origin. Astronomers were puzzled by the fact that the regions of bright radio emission were not associated with bright optical objects (eg. Bolton & Stanley, 1948). Bolton et al. (1949), again using a sea-cliff interferometer, suggested that the radio sources Virgo A (M87) and Centaurus A were associated with large elliptical galaxies.

At around this time, synchrotron radiation was also "discovered" by accident. In 1947, a newly built synchrotron particle accelerator at General Electric was being monitored for sparks, as the equipment was pushed to its limits. Instead of seeing sparks, a bright spot of light was seen where the beam was approaching the observer (Elder et al., 1947; Blewett, 1998). This emission was aptly named synchrotron radiation. The theory of electromagnetic radiation from charged particles on a circular trajectory had been discussed since 1898 (eg. Lienard, 1898; Schott, 1912) and the energy loss by electrons in particle accelerators due to radiation had been predicted (eg. Blewett, 1946), but the serendipitous discovery of synchrotron radiation in 1947 allowed the spectrum and angular distribution to be measured and the theory confirmed (eg. Elder et al., 1948).

Soon after this discovery, Alfvén & Herlofson (1950) suggested that the cosmic noise from the "radio stars" could be due to synchrotron emission from cosmic-ray electrons in stellar magnetic fields. While the association of radio sources with stars was incorrect, this was the first suggestion that the synchrotron mechanism could be responsible for the observed radio emission. Several authors predicted that the optical emission in the Crab Nebula, and in the jet of M87 should have a high degree of linear polarization if it were produced via the synchrotron mechanism. These predictions were confirmed observationally by Dombrovsky (1954)

and Baade (1956). Numerous other studies along these lines provided strong evidence that the cosmic radio noise was due to synchrotron radiation produced by relativistic electrons and positrons gyrating in a magnetic field, and this explanation was widely accepted by the late 1950's (eg. Burbidge, 1956).

As is commonly the case in all fields of astronomy, advancement of the understanding of radio galaxies was largely dictated by improvements in instrumentation. The advent of aperture synthesis radio interferometers had a huge impact on radio astronomy, as the resolution of radio images drastically improved. One of the first aperture synthesis interferometers was built at Cambridge University. The Third Cambridge Catalogue of Radio Sources (3C) was the result of observations with the four-element Cambridge interferometer, and listed a total of 471 discrete sources with a flux density greater than 8 Jy at 159 MHz (Edge et al., 1959). The revised version of this catalogue (3CR — Bennett, 1962) was the definitive catalogue of bright radio sources in the Northern hemisphere, and to this day, many northern radio sources go by their 3C names, eg. 3C 273. The radio images did not however have high enough resolution or dynamic range to reveal the presence of beams or jets in radio galaxies — at that stage only the lobes were distinguishable. Baade & Minkowski (1954) first used the term "jet" to describe the thin linear feature in optical images of M87 (which was in fact first detected in 1918 (Curtis, 1918)), and suggested that the jet was ejected from the nuclues. Radio emission associated with the optical jet of M87 was reported by Miley et al. (1970). However, the nature of radio galaxies remained a mystery.

The year 1974 saw many dramatic developments in the study of radio galaxies, largely due to the publication of the first high resolution (2″) map of Cygnus A from the 5-km Cambridge interferometer shown in Figure 1.1(a) (Hargrave & Ryle, 1974). This high resolution map of Cygnus A revealed compact, high surface brightness sources near the end of the radio lobes, described as "hotspots". The synchrotron lifetimes of the electrons responsible for the observed emission were estimated to be shorter than the light travel time from the active nucleus to the hotspot, and it was therefore argued that these hotspots required a continuous supply of energy (Hargrave & Ryle, 1974). (Scheuer, 1974) had proposed a "continuous supply" model for radio galaxies, and the new radio map of Cygnus A by Hargrave & Ryle (1974) led Blandford & Rees (1974) to postulate the "twin exhaust" model, which clearly established the basic paradigm for the understanding of radio galaxies. In this model, the active galactic nucleus generates two oppositely directed beams of light fluid with large bulk velocities. Each beam terminates and converts much of its bulk energy into relativistic particles and magnetic fields at a "working surface" where the jet meets the ambient medium, and this working surface is identified with the hotspots. The working surface advances outward at a speed determined by the balance of momentum flux in the beam and ram pressure of the intergalactic medium. The impact of the jet on the ambient medium generates a reverse shock that propagates upstream into the beam material, and this

shock is responsible for the conversion of bulk kinetic energy into random particle energy and turbulence. The beam material flows through the hotspots and back towards the nucleus, spreading out to form the extended radio lobes. The situation envisaged by Blandford & Rees (1974) to explain the obseved radio morphology of Cygnus A (Figure 1.1(a)) is illustrated in Figure 1.1(b).

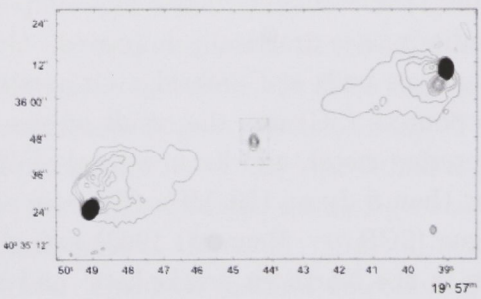

(a) Image of Cygnus A at 5 GHz from Hargrave & Ryle (1974). Resolution $2'' \times 3.2''$. The black blobs at the ends of the lobes are closely spaced contours marking the location of the hotspots.

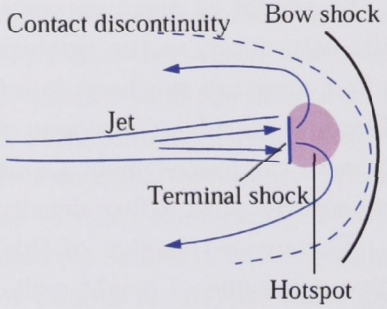

(b) Cartoon diagram of the basic paradigm for the understanding of high power (FRII) radio galaxies. Image Credit: Geoff Bicknell

Figure 1.1:

Also in 1974, Fanaroff and Riley identified two characteristic radio galaxy morphologies, and made the very important discovery that the morphological classification is related to the radio luminosity. This important classification scheme is discussed further in §1.2

As mentioned above, Blandford & Rees (1974) predicted the existence of beams of matter in all radio galaxies, but limited resolution and dynamic range meant that very few of these beams were detected in early radio images. In those objects where jets were detected, only limited information could be gained by studying the radio emission alone. As discussed later in §2.3.4, the study of optically thin synchrotron emission does not allow a unique determination of the magnetic field strength and electron density — an additional constraint is required. In this context, the advent of X-ray astronomy was of great importance. The detection of inverse Compton X-rays provides an additional constraint on the relativistic electron density, and in some cases allows the source properties to be uniquely determined.

X-ray astronomy began in the early 1960's, and the first X-ray jet was detected by Schreier et al. (1979). By the mid-1990's, several hundred extragalactic jets had been observed at radio wavelengths (Liu & Xie, 1992; Liu & Zhang, 2002), but only four of the nearest and brightest extragalactic jets had been detected at X-ray wavelengths (Stawarz, 2003, and references therein). Similarly, only a handful of hotspots had been detected in the X-ray band (eg. Harris et al., 1994). The *Chandra* X-ray Observatory (formerly known as the Advanced Astrophysics X-ray

Facility, or AXAF) was launched in mid-1999, with sensitivity and resolution much greater than that of previous X-ray facilities such as Einstein and ROSAT. It was hoped that *Chandra* would provide many new detections of extragalactic jets at X-ray wavelengths. In fact, during *Chandra*'s initial design stages one of the major science goals was to compare the X-ray structure of AGN jets with their radio images[2]. With such great improvement in the capability of X-ray astronomy, the launch of *Chandra* marked the beginning of a new era in the study of extragalactic jets.

1.1.1 The Chandra Era

Chandra's very first observations produced an amazing discovery. The quasar PKS 0637–752 was believed to be a moderate strength point source at X-ray wavelengths, and was therefore used for focusing *Chandra*'s mirrors. However, the first calibration observations revealed a surprisingly strong X-ray jet[3] extending 12 arcseconds (80 kpc projected) from the quasar core, coincident with the previously known radio jet (Schwartz et al., 2000; Chartas et al., 2000). The strong X-ray emission from the kpc-scale jet of PKS 0637–752 was hard to explain in terms of standard emission mechanisms such as thermal brehmstralung or synchrotron self Compton emission (Chartas et al., 2000; Schwartz et al., 2000). This led Tavecchio et al. (2000b) to propose a model for the kpc-scale jet in which the flow velocity is highly relativistic and directed close to the line of sight. Introducing a relativistic velocity increases the energy density of the cosmic microwave background (CMB) in the rest frame of the jet plasma, thereby increasing the X-ray emissivity produced via inverse Compton scattering of CMB photons (Tavecchio et al., 2000b; Celotti et al., 2001). This is the so-called IC/CMB model. This model can account for the observed radio to X-ray spectral energy distribution in the jet of PKS 0637–752, while minimizing the total (radiative plus kinetic) power of the jet (Ghisellini & Celotti, 2001). *Chandra*'s very first observations had produced a surprising discovery, and suggested that the number of X-ray jet detections would be much greater than anticipated.

Following these somewhat surprising results, two teams independently initiated systematic studies of the X-ray emission from extragalactic jets by surveying well defined samples of radio jets (Sambruna et al., 2002, 2004; Marshall et al., 2005). These surveys involved relatively short "snapshot" exposures of arcsecond scale jets, in order to assess the properties of the population, and identify candidate sources for follow-up observations with much longer integration times. The samples were selected based on well defined selection criteria, but were essentially chosen to

[2]Scientific Requirements for the Calibration of AXAF, MSFC-RQMT-2229, August 2 1995 `http://cxc.harvard.edu/cal/docs/cal_sci_req.html`

[3]The term "jet" is used to refer to a feature in an image of a radio galaxy. For example, the term "radio jet" refers to an elongated jet-like feature observed in a radio image, and the term "X-ray jet" refers to a feature observed in an X-ray image.

include sources with relatively bright, and relatively long radio jets — sources most likely to exhibit X-ray emission bright enough, and far enough from the nucleus, to be detected in short *Chandra* exposures.

These snapshot surveys found that X-ray emission is common in kpc-scale quasar jets; the majority of X-ray jets have structures that closely match structures in the corresponding radio jets; the X-ray spectral indices are generally flat ($\alpha_x \sim 0.5 - 1$)[4]; detected X-ray jets tend to be one-sided; and, in most cases, the X-ray emission can be interpreted in terms of inverse Compton scattering of CMB photons, but cannot be interpreted in terms of synchrotron emission from the same electron population responsible for the radio synchrotron emission (Sambruna et al., 2002, 2004; Marshall et al., 2005).

In addition to the snapshot surveys of extragalactic jet sources, longer *Chandra* observations of individual sources were combined with optical, infra-red and radio observations in order to study the evolution of the spectral energy distribution along the jets. These detailed studies of individual sources revealed problems associated with the IC/CMB interpretation of jet X-ray emission. Several alternative models have been proposed, and debate about the X-ray emission mechanism, as well as other fundamental questions regarding extragalactic jets, continues. The issues relating to the quasar jet X-ray emission mechanism are discussed further in §1.6.

1.1.2 The Contribution of this Thesis

My PhD thesis is based around the ongoing work of an international collaboration of astronomers using high resolution radio, optical and X-ray imaging to study the dynamics of large scale quasar jets. This collaboration (the Marshall et al. quasar jet survey team) is undertaking a *Chandra* X-ray survey of flat spectrum radio quasars with arcsecond scale radio jets. At the time of my enrolment in the PhD program at Mount Stromlo Observatory, the Marshal et al. X-ray survey was two thirds complete, and from the preliminary results of the survey, a sample of seven quasar jets had been selected for detailed follow-up study with deep integrations in both X-ray and optical bands. This thesis involves analysis and detailed physical modeling of two of the seven quasar jet sources for which follow-up *Chandra* observations were obtained.

My thesis began with an observing campaign using the new 12mm system at the Australia Telescope Compact Array to observe 14 of the X-ray survey targets. I was responsible for the observations, data reduction and analysis of these data which will be of great importance in multi-wavelength studies of these objects. The direction of the thesis subsequently took many twists and turns. However, investigations eventually revealed some great surprises and very intriguing results.

[4]Throughout this thesis, the spectral index α is defined such that $F_\nu \propto \nu^{-\alpha}$

1.2 The Fanaroff and Riley Classification Scheme

As noted above, Fanaroff & Riley (1974) identified two characteristic radio galaxy morphologies. The Fanaroff and Riley classification is based on a single morphological criterion: the ratio (R_{FR}) of the distance between the regions of highest surface brightness on opposite sides of the galaxy, to the total size of the source. If the ratio $R_{FR} < 0.5$ (i.e. the jets are brightest closest to the core), then the source is classified as a Fanaroff and Riley type I object (FRI). If the ratio $R_{FR} > 0.5$ (i.e. the brightest emission is near the end of the jet furthest from the core), the object is classed as a Fanaroff and Riley type II object (FRII). Classic examples of each class are shown in Figures 1.2 and 1.3. Fanaroff & Riley (1974) found that the total source luminosity at 178 MHz was generally greater for FRII sources than for FRI sources, with the transition from class I to class II occuring at $L_{178\,\mathrm{MHz}} \approx 2 \times 10^{25}$ W Hz^{-1} sr^{-1}. Owen (1993) and Owen & Ledlow (1994) have shown that the dividing line between FRI and FRII radio galaxies is dependent on the host galaxy optical luminosity.

In one class of models for FRI radio sources, an initially supersonic jet is decelerated to transonic speeds on kpc-scales, resulting in diffuse "plumes" of emission in the outer regions of the source (Bicknell, 1994; Perucho & Martí, 2007). Other models for FRI radio galaxies (Meier, 1999) suggest that the jets in these objects are launched at a slower speed than the jets of FRII radio sources.

In FRII radio galaxies, it is understood that the supersonic jets remain highly collimated and do not decelerate substantially until reaching the outer extremes of the source where the jets are decelerated in a strong shock that is produced due to the interaction of the jet with the external medium.

In this thesis I focus on the study of large-scale jets in high power sources with the characteristic FRII morphology.

1.3 A Broader Context

Before providing more in depth discussion of some selected topics relating to extragalactic jets, it is important to put the study of large-scale FRII jets into a broader context. In this section I give a very brief discussion of some basic questions about the significance and place of extragalactic jets in the universe.

1.3.1 Where are Extragalactic Jets Found?

Extragalactic jets have been observed over a wide range of redshifts, from as close as 3.4 Mpc (Centaurus A) out to at least $z = 4.3$ (Cheung, 2004). While high redshift ($z > 2$) radio galaxies are relatively rare (Miley & De Breuck, 2008), large, powerful radio sources with total projected linear extents up to 150 kpc have been observed at redshifts $z \gtrsim 3.8$ (Miley & De Breuck, 2008; Wardle et al., 2008).

Figure 1.2: The FRII radio galaxy Cygnus A (3C405) at 6cm (Image Credit: C. Carilli).

Figure 1.3: The FRI radio galaxy 3C31 (Image Credit: A. Bridle)

Host Galaxies

FRI and FRII radio sources are almost exclusively associated with giant elliptical galaxies. The hosts of nearby radio sources in clusters are not significantly different to "normal" elliptical galaxies in clusters, and typically host low power sources (FRIs) (Ledlow & Owen, 1995a; McLure et al., 1999, 2004). However, up to one third of powerful radio sources show peculiar optical morphology, suggestive of recent galaxy merger (Heckman et al., 1986). The host galaxies of FRI

radio sources are more luminous than the host galaxies of FRIIs (Heckman et al., 1986; Ledlow & Owen, 1996). This is a puzzling result, since, as described by de Young (2002, pg. 316) "...a more luminous galaxy could be assumed to have a more massive black hole, which naively might be thought to produce a more powerful radio source, but instead the opposite is seen." This finding may suggest the environment plays a key role in determining the class of radio galaxy that is formed (see eg. Bicknell, 1995).

Seymour et al. (2007) studied a sample of radio galaxies out to redshift 5.2 and found that the host galaxies lie at the upper end of the stellar mass function even at high redshift, with stellar masses around $10^{11} - 10^{12}$ M$\odot$.

The lifetimes of radio sources ($\sim 10^7$ years, eg. Shabala et al., 2008) are relatively short compared to the age of the universe, and it is suggested that radio sources may be a transient phenomenon that occurs in all giant elliptical galaxies at some time (or several times) throughout their life.

Large Scale Environment

In the local universe, the large scale environment of FRI radio galaxies is significantly different to that of FRII radio galaxies. Nearby FRI radio galaxies are typically found in rich clusters, while, in general, FRII radio galaxies inhabit poor clusters or rich groups (Heckman et al., 1986; Prestage & Peacock, 1988; Zirbel, 1997). Supporting this claim is the finding that nearby low power radio sources are frequently associated with extended X-ray emission, while high power sources are not (Miller et al., 1999). However, studies of high redshift radio galaxies indicate that beyond $z \sim 0.5$, both FRI and FRII sources are associated with clusters (Hill & Lilly, 1991; Bahcall & Chokshi, 1992).

The probability of hosting a radio source increases with the optical luminosity of the host galaxy. The radio source detection rate is largely independent of cluster morphology or richness, hence the probability of hosting a radio source is almost entirely determined by the galaxy's optical luminosity (Ledlow & Owen, 1995b).

Radio galaxies are preferentially located at small cluster radii. This result can be explained by the fact that brighter galaxies are located at small cluster radii, and the probability of hosting a radio source increases with optical luminosity (Ledlow & Owen, 1995b).

Brightest cluster galaxies (BCGs) are very large luminous elliptical galaxies that lie at the centers of galaxy clusters. BCGs are up to a factor of ten times more likely to host radio loud AGN than other galaxies of the same mass (Best et al., 2007). Two of the most luminous radio galaxies, Cygnus A and 3C 295, are located at the centre of rich galaxy clusters.

1.3.2 How Common are Extragalactic Jets?

Liu & Zhang (2002) compiled a list of all known extragalactic jets as of December

2000. The list comprised a total of 661 objects and included jets associated with quasars, radio galaxies, seyferts and BL Lacs.

All radio loud AGN are understood to be associated with jet activity (Urry & Padovani, 1995). The probability of a galaxy hosting a radio loud AGN is a strong function of the galaxies stellar mass, rising from nearly zero below a stellar mass of $10^{10} M_{\odot}$ to more than 30 per cent at stellar masses of $5 \times 10^{11} M_{\odot}$ (Best et al., 2005). That is, nearly one third of the most massive galaxies exhibit at least some level of jet activity. It is estimated that approximately 5% of giant elliptical galaxies host FRII radio sources (Schmidt, 1972).

The frequency of occurrence of extragalactic jets is a function of their radio power. This is described by the radio luminosity function. High power (FRII) objects are less common than lower power (FRI) objects. In fact, nearby FRI radio sources are almost 100 times more numerous than nearby FRII objects (de Young, 2002).

To get an idea of the relative abundance of jets in the universe, it is interesting to compare the space density of low redshift FRI sources ($\sim 3 \times 10^{-4}$ Mpc^{-3}) to the space density of common (i.e. spiral) galaxies ($\sim 3 \times 10^{-2}$ Mpc^{-3}) (de Young, 2002, and references therein). Radio galaxies constitute about 1% of all galaxies.

1.4 FRII Jets In Detail

I now discuss in detail the major features of FRII jets: knots and hotspots.

1.4.1 Jet Knots

FRII jets often exhibit localized brightness enhancements, commonly referred to as "knots". The knotty structure is generally more pronounced in quasar jets than radio galaxy jets. Figure 1.4 (particularly the optical image) clearly shows the knots of bright emission along the jet of 3C273. The production of knots and the particle acceleration mechanism within the knots are still topics for debate (eg. Stawarz et al., 2004; Niemiec et al., 2006). Models for the production of jet knots are closely linked to the discussion of quasar jet X-ray emission mechanisms and the understanding of extragalactic jets. In this section I consider some of the models for the production of jet knots and the problems these models face.

In one class of models, knots are identified with strong shocks in a uniform and continuous flow. At the shock, particles are accelerated via the first order Fermi mechanism to produce a power-law energy distribution. Such internal shocks could be formed due to intrinsic velocity irregularities in the jet (Rees, 1978; Sahayanathan & Misra, 2005), by interactions between the jet and dense clouds in the external medium (Blandford & Koenigl, 1979), they could be re-confinement/re-collimation shocks (Sanders, 1983; Komissarov & Falle, 1998; Aloy et al., 1999), or they could be associated with large scale instabilities in the flow (eg. Bicknell &

Begelman, 1996). However, Tavecchio et al. (2003) have argued that the interpretation of jet knots in terms of strong shocks in a continuous flow is incompatible with the observation that the brightness profile of knots is largely frequency independent. The frequency independence of knot brightness profiles is unexpected because of the difference in cooling time-scales for particles of different energies. In the IC/CMB model for X-ray emission, it is the low energy electrons ($\gamma \sim 100$) responsible for the X-ray emission. The radiative cooling time scale for $\gamma \sim 100$ electrons is extremely long compared to that of the particles responsible for the radio ($\gamma \sim 1000$) and optical ($\gamma \sim 10^4 - 10^5$) emission. If adiabatic cooling dominates over radiative cooling, the cooling timescale is energy independent, so that frequency independent knot profiles are produced. However, Tavecchio et al. (2003) argue that if a knot is homogeneously filled by a single relativistic particle population, radiative and adiabatic losses alone cannot account for the rapid drop in brightness outside the knot, and cannot explain the frequency independent brightness profiles. They propose that knots in kpc-scale jets are composed of many small (unresolved) clumps, associated with sites of particle acceleration, that are hotter and more dense than their surroundings. These clumps can expand much faster than a single homogenous knot, thereby allowing for rapid adiabatic cooling that produces a rapid drop in brightness outside the knots, and frequency independent knot profiles. It should be noted that in such a model, synchrotron self Compton emission could produce the observed X-ray flux, so that the IC/CMB model would no longer be required to explain the high level of X-ray emission (Stawarz et al., 2004).

Stawarz et al. (2004) have suggested an alternative explanation for the existence of jet knots with frequency independent brightness profiles. They suggest that the knots represent separate moving portions of a relativistic jet with excess kinetic power and argue that such a situation is expected if the activity of central engine is intermittent or highly modulated (see also Bridle et al., 1986, 1989; Clarke et al., 1992; Siemiginowska et al., 2007; Kataoka et al., 2008). In this model, Stawarz et al. (2004) postulate a synchrotron origin for the X-ray emission in quasar jets. Such a model requires particle acceleration acting over an extended volume rather than occurring at a single shock front, since the synchrotron X-ray emitting electrons have extremely short cooling timescales. In this case, the knot sizes are related to the size of the particle acceleration sites and not to the cooling length of the electrons, as in the single-shock IC/CMB and SSC models.

Kataoka et al. (2008) have suggested a similar model in which the central engine ejects heavy knots in flare-like activity periods, with a continuous lighter, faster jet produced in between the flares. The lighter, faster jet material collides with the slower, heavy knots and causes a reverse shock to propagate upstream into the lighter, faster jet material. In this case the radio knots are associated with the heavy portions of the jet flow, while the X-ray knots are associated with the freshly accelerated particles downstream of the reverse shock. This model was

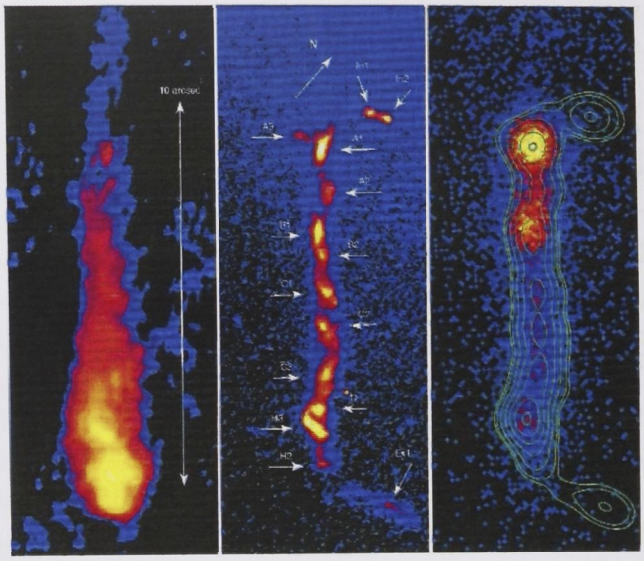

(a) Images of the jet of 3C273 in different observing bands (from Marshall et al., 2001). From left to right: radio, optical and X-ray (with optical contours overlaid).

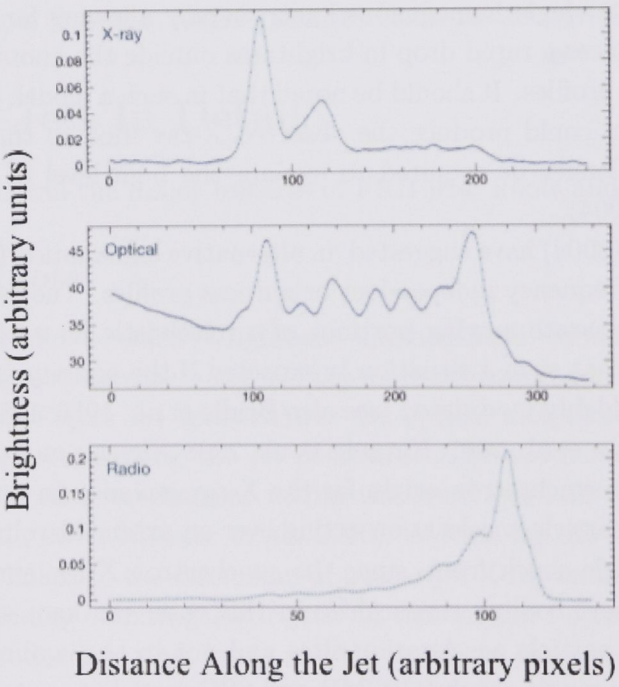

(b) Surface brightness profiles along the jet of 3C273 in different observing bands (from Harris & Krawczynski, 2006). From top to bottom: X-ray, optical and radio.

Figure 1.4: These figures serve to illustrate the knotty structure that is common among FRII and quasar jets, and that jets can appear significantly different in different observing bands.

developed to account for the apparent offsets between radio and X-ray peaks in the jet of 3C 353.

The transverse structure of quasar jet knots is generally unknown. However, (Marshall et al., 2006) report that in 3C 273 the X-ray emission from the knots is narrower than the X-ray emission from the inter-knot regions and is also narrower than the associated optical emission in the knots. Similarly, Kataoka et al. (2008) find that the X-ray emission from the jets of the FRII radio galaxy 3C 353 is narrower than the associated radio emission.

In some cases spatial offsets between the peak brightness of the X-ray and radio knots has been observed (see below), and the polarization position angle in X-ray bright knots often appears perpendicular to the jet direction, indicating the magnetic field is aligned with the jet flow (eg. Schwartz et al., 2000). These observational characteristics must be considered when discussing the knot production mechanism in large-scale quasar jets.

Offsets Between Radio and X-ray Knots

Offsets between the radio and X-ray peaks in the order of tens of parsecs have been observed in a number of nearby FRI radio galaxy jets including Centaurus A, M87, 3C 66B and 3C 31 (see Hardcastle, 2003, and references therein). In these objects the X-ray emission is interpreted as synchrotron emission from the same electron population responsible for the radio to optical continuum. The linear resolution in Chandra images of powerful quasar jets (generally with $z \gtrsim 0.5$) is not sufficient to detect sub-kpc scale offsets, and it is not clear whether similar offsets exist in the knots of powerful quasar jets whose X-ray emission is interpreted as IC/CMB. Offsets between the peaks of X-ray and radio emission in the knots of quasar jets have been reported in the nearby quasar 3C 273 and FRII radio galaxy 3C 353 (Marshall et al., 2001; Kataoka et al., 2008, respectively). However, in each case it has been argued that the X-rays are synchrotron in origin.

In the case of quasar jets with an IC/CMB interpretation of X-ray emission, the existence of large offsets has not been clearly demonstrated. Siemiginowska et al. (2002) identified offsets of between $1''$ to $2''$ between the peaks of the radio and X-ray knots in the 300 kpc jet of PKS 1127-145. However, deeper observations revealed that the offsets are in fact due to substructure in the X-ray jet that was not detected in the initial observations (Siemiginowska et al., 2007). Siemiginowska et al. (2003) reported that in the GPS quasar B2 0738+313 "...a slight shift between X-ray and radio knot emission can be noticed. With the current data we cannot really quantify the amount of shift." Hence, it is not clear that the large X-ray/radio offsets exist in quasar jets.

1.5 Hotspots

1.5.1 Morphology

A hotspot is a radio bright (and sometimes optical and X-ray bright) region at the end of an extragalactic jet, understood to be associated with the jet termination (see Figure 1.2). The basic paradigm for the understanding of hotspots envisaged by Blandford & Rees (1974) is illustrated in Figure 1.1(b). The hotspot marks the location where the jet encounters the ambient medium at the end of the radio lobes. At this point, the jet is decelerated via a strong reverse shock propagating into the jet material and the bulk kinetic energy is converted to internal energy of the plasma, turbulence, and magnetic fields. The hotspot is identified with the plasma downstream of the reverse shock. To first order, this model works very well. However, as the resolution and sensitivity of radio telescopes improved, double and sometimes multiple regions of high surface brightness were identified near the jet head and it was observed that the hotspot regions were often more complex than expected from the idealized situation described above. It turns out that at high resolution there is no common hotspot morphology, and the complexity of hotspots makes it very difficult to define exactly what is meant by the term "hotspot". Perley (1989) write, in a section titled "Just What IS a Hotspot?", "In fact, I believe it may not even be possible to define a hotspot in terms of observed parameters alone". At least qualitatively a hotspot is a region of high surface brightness close to the end of a radio lobe furthest from the active nucleus (Laing, 1989). Laing (1989) analysed a set of 60 high resolution (0.″1) images of nearby FRII radio galaxies and described the characteristic hotspot morphologies in terms of "primary hotspot" and "secondary structures". Primary hotspots are defined as the most compact (and usually brightest) components near the leading edge of the radio lobes. The sizes of the primary hotspots are generally 0.5 — 2 kpc in diameter. The more diffuse secondary structures near the primary hotspot were recognized to have a variety of complex morphologies, but two characteristic forms are identified: double hotspots where a larger, less bright hotspot accompanies the primary, and flaring hotspot, where, "...instead of being separated into two discrete components, the structure consists of a primary hotspot and a curved emitting region expanding away from it." The wide range of complex hotspot morphologies suggest that the hotspot structure is transient on relatively short timescales. Indeed, simulations of radio galaxies indicate that the hotspot structure changes on a flow crossing timescale (Saxton et al., 2002).

1.5.2 Hotspot Radio to X-ray Spectra

Synchrotron Spectra: Hotspot spectra from radio to optical wavelengths are often well described by a power-law or broken power-law with a high energy cutoff (Heavens & Meisenheimer, 1987; Meisenheimer et al., 1997). Example synchrotron

spectra are shown in Figure 1.5.

In a small number of cases, the hotspot radio spectrum is observed to flatten at low frequency. An example of this behaviour is illustrated in Figure 1.5(b). In this figure, two of the low frequency data points lie below an extrapolation of the power-law spectrum. Such behaviour is often taken as evidence for a low energy cutoff in the electron energy distribution. The low energy cutoff in hotspot spectra is a major topic of study in this thesis, and is discussed in more detail in §3.1.

Models for hotspot synchrotron spectra, specifically broken power-law distribution functions, are further discussed in §2.5.

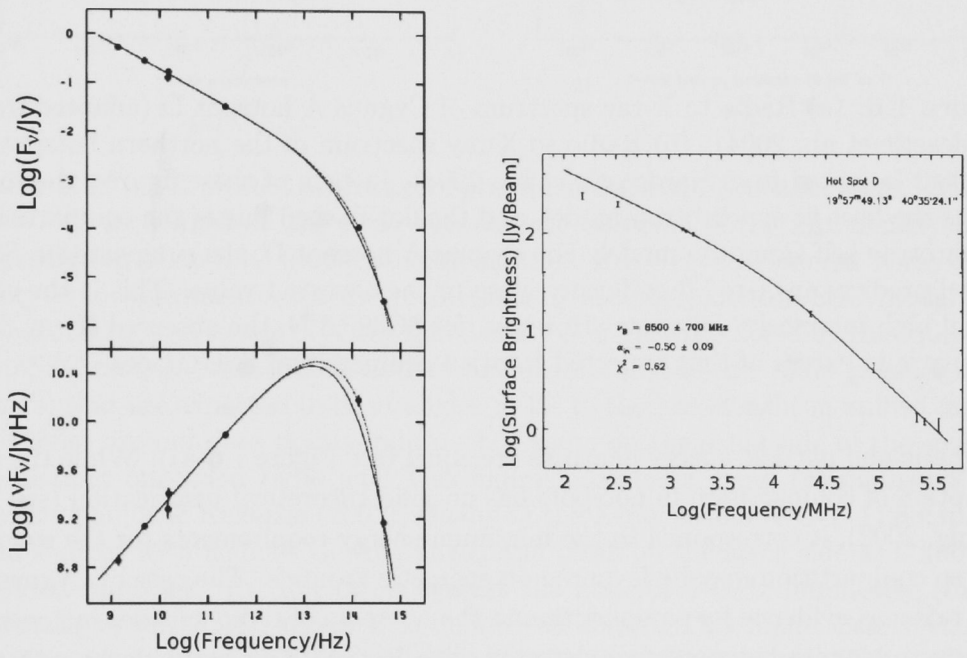

(a) (b)

Figure 1.5: (a) Radio spectrum (top) and spectral energy distribution (bottom) of the Eastern hotspot of 3C111 from Meisenheimer et al. (1989). This spectrum is well described by a power law (spectral index $\alpha = 0.55$) with an exponential cutoff above $\nu_c = 8 \times 10^{13}$ Hz (b) Radio spectrum of Cygnus A hotspot D from Carilli et al. (1991). This spectrum clearly exhibits a broken power-law form, with the spectral index changing from $\alpha = 0.5$ to $\alpha = 1.0$ at $\nu_b \approx 6.5$ GHz. At low frequency the spectrum begins to turn down. This may be evidence for a low-energy cutoff in the electron distribution.

X-ray Spectra: The hotspots of Cygnus A were the first to be detected at X-ray wavelengths with the ROSAT Satellite (Harris et al., 1994). The observed X-ray flux densities in these hotspots were found to be consistent with the equipartition synchrotron self Compton (SSC) model: that is, a SSC model in which the

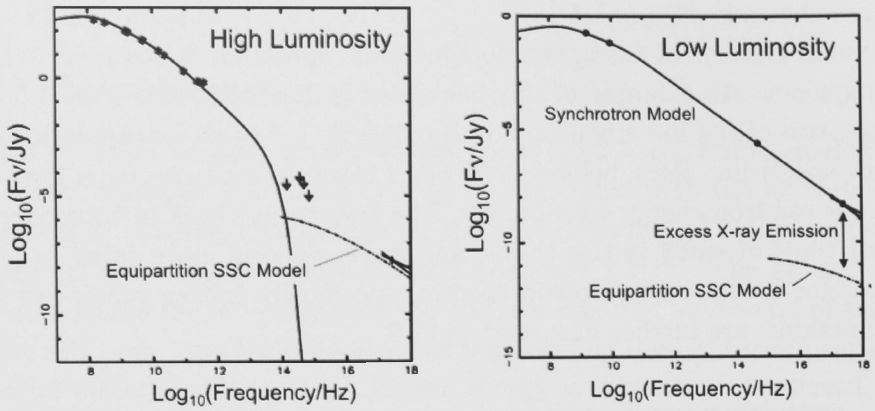

(a) (b)

Figure 1.6: (a) Radio to X-ray spectrum of Cygnus A hotspot D (adapted from Hardcastle et al., 2004). (b) Radio to X-ray spectrum of the northern hotspot of 3C390.3 (adapted from Hardcastle et al., 2004). In each of these figures, the solid line is the best fit synchrotron model, and the dot-dashed line is the equipartition synchrotron self Compton model. For Cygnus A hotspot D, the equipartition SSC model predicts an X-ray flux density close to the observed value. This is the case for all high luminosity hotspots. However, for 3C390.3 N, the observed X-ray flux density is in excess of that expected from an equipartition SSC model.

magnetic and particle energy densities are equal (see Figure 1.6(a)). While the assumption of equipartition in hotspots has no solid theoretical justification (see De Young, 2002), it corresponds to the minimum energy requirements for the source, and so equipartition may be favoured on energetic grounds. The case of Cygnus A was taken as evidence for equipartition in the hotspots of radio galaxies in general. However, as more hotspots were detected with ROSAT and particularly with the *Chandra* X-ray Observatory, many hotspots were found to have an excess of X-ray emission relative to the equipartition SSC model prediction (see Figure 1.6(b)). Either these hotspots have magnetic field strengths well below the equipartition value, or another emission mechanism is responsible for the observed X-ray flux. The question is, why do some hotspots have X-ray emission at a level consistent with the equipartition SSC model, while others require an additional component or a lower than equipartition field strength?

Georganopoulos & Kazanas (2003) showed that the amount of excess X-ray emission relative to the equipartition SSC model is related to the jet viewing angle: hotspots with excess X-ray emission are typically associated with small jet viewing angles, while hotspots with no excess X-ray emission typically lie in the plane of the sky (see Figure 1.7(a)). Georganopoulos & Kazanas (2003) postulated that the excess X-ray emission is due to so-called "upstream-Compton" (UC) scattering. In the UC model, particles in the relativistic jet approaching the hotspot inverse Compton scatter the synchrotron photons produced within the hotspot, and this

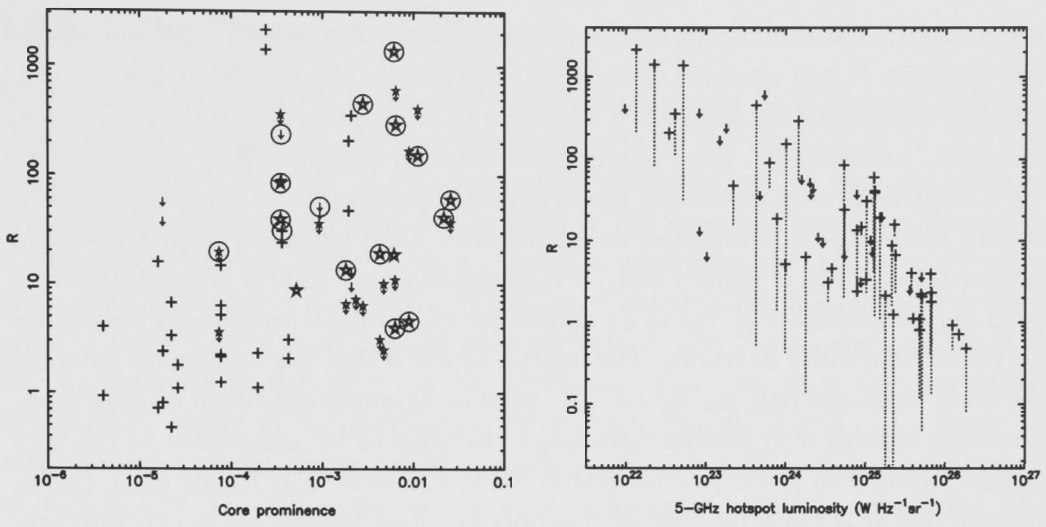

Figure 1.7: (a) R plotted against core prominence (from Hardcastle et al., 2004), where R is as defined as the ratio between the observed X-ray flux density and the prediction of an SSC model at equipartition. If R=1, the observed X-ray flux density is in agreement with the predictions of the equipartition SSC model. If $R >> 1$, there is an excess of X-ray flux density over that predicted by the equipartition SSC model. Stars indicate broad-line objects (broad-line radio galaxies and quasars) that are expected to lie at angles $\gtrsim 45°$ to the line of sight in unified models. Circles around data points indicate hot spots on the same side of the source as a distinct one-sided radio jet. This figure indicates a trend (as discussed by Georganopoulos & Kazanas (2003)): many of the X-ray excess ($R >> 1$) hotspots are in sources with a small viewing angle, and often on the same side as a known one-sided radio jet. (b) R plotted against the hotspot 5 GHz luminosity (from Hardcastle et al., 2004), where R is defined as above. This figure clearly shows that the amount of excess X-ray radiation relative to an equipartition SSC model is anti-correlated with hotspot radio luminosity, and that high luminosity hotspots have X-ray flux density that is in good agreement with the equipartition SSC model.

emission is strongly Doppler beamed along the direction of jet motion. In objects with small viewing angles, the "upstream-Compton" emission is enhanced, while for objects in the plane of the sky, the upstream-Compton emission is de-beamed, so that synchrotron self Compton is the dominant emission mechanism. Such a model can explain the apparent correlation illustrated in Figure 1.7(a).

However, Hardcastle et al. (2004) have argued against such an interpretation, claiming that the the apparent relationship between proxies for viewing angle (eg. core spectral classification (broad line/narrow line) and core prominence) and the X-ray brightness of the hotspot may be explained by a selection effect in the available X-ray data. Hardcastle et al. (2004) show that the amount of excess X-ray radiation relative to an equipartition SSC model is anti-correlated

with hotspot radio luminosity (Figure 1.7(b)). In other words, high luminosity hotspots have X-ray emission consistent with a near equipartition SSC model, while low luminosity hotspots have an excess of X-rays relative to the SSC model prediction. Interestingly, some of the low luminosity hotspot SEDs are consistent with a single or broken power-law spectrum connecting radio to X-ray data-points, and can therefore be interpreted as synchrotron X-ray emission from a standard electron population (Figure 1.6(b)). Hardcastle et al. (2004) suggest that the excess hotspot emission is due to an additional synchrotron component that exists only in low luminosity hotspots. The interpretation is that low luminosity hotspots have lower magnetic field strengths and therefore slower synchrotron cooling rates. The slower synchrotron cooling rates allow electrons to be accelerated to the high energies required to produce synchrotron X-ray emission. Hardcastle et al. (2004) conclude that it is plausible that all hotspots are close to equipartition conditions.

The results of Chapter 3 support the model of Hardcastle et al. (2004). The object studied in Chapter 3, PKS 1421–490, is a broad line radio galaxy with a large apparent jet bend, indicating that the source has a small viewing angle. Moreover, this object has a high hotspot/counter-hotspot flux density ratio at both radio and X-ray wavelengths, similar to Pictor A. The model of Georganopoulos & Kazanas (2003) predicts that significant excess X-ray flux should be observed in this hotspot due to the upstream Compton process, while the model of Hardcastle et al. (2004) predicts that the X-ray flux should be consistent with the equipartition SSC model, because the hotspot has a high radio luminosity. In chapter 3 we show that the X-ray flux density of the high luminosity hotspot in PKS 1421–490 is indeed consistent with the equipartition SSC model, providing further evidence against the upstream Compton model as the dominant contribution to the X-ray flux density in hotspots.

1.6 X-ray Emission Mechanism in kpc-Scale Quasar Jets

As discussed above, the very first Chandra observations posed an interesting question: "Why is the X-ray emission from quasar jets at a level much greater than predicted by synchrotron or synchrotron self Compton models?" Almost ten years after the launch of Chandra, the emission mechanism in quasar jets is still fiercely debated. In this section I discuss the recent literature regarding the X-ray emission mechanism in kpc-scale quasar jets.

In the literature, reference to a so-called "standard electron energy distribution" is often made. Before discussing the arguments for and against various models, it is important to describe exactly what is meant by a "standard" electron energy distribution.

1.6.1 The "Standard" Electron Energy Distribution

Models of the first order Fermi acceleration mechanism at a strong relativistic shock produce power-law electron energy spectra of the form $N(\gamma) \propto \gamma^{-a}$ with energy index $a \sim 2 - 2.2$. If an observed jet spectrum can be well described by a power-law, first order Fermi acceleration is the favoured particle acceleration mechanism (although there is by no means a consensus on this issue (Stawarz et al., 2004; Niemiec et al., 2006)). It should be noted that a full relativistic treatment of shock acceleration has not been performed, and the conclusions based on the approximate models may not be justifiable. The "standard electron energy distribution" refers to the distribution produced in models of first order Fermi acceleration at a single strong shock: a single power-law with an exponential cutoff at high energy. In some cases, synchrotron or inverse Compton cooling may produce a "cooling break" and cause the spectrum to steepen towards higher energy. Thus, a broken power-law that steepens towards higher energy is also regarded as "standard".

In this standard model, there is no process whereby the spectrum can flatten towards higher energies. Therefore a single power-law or downward curving spectrum is considered "standard", whereas any spectrum that flattens towards higher energies is considered non-standard, because some additional process is required to create such a distribution. It should be noted that non-standard electron spectra are not physically impossible, they simply require a different acceleration mechanism, or adjustments to the simple shock acceleration model.

1.6.2 Quasar Jet Spectral Energy Distributions

X-ray emission from the jets of FRI radio galaxies is common (Worrall et al., 2001). Some FRII jets (eg. Pictor A, 3C219, 3C403, and PKS 2152–69) have been detected at X-ray wavelengths. In almost all FRI and FRII radio galaxies, the jet X-ray flux is interpreted as synchrotron emission because the radio, optical and X-ray flux densities can be fit using a standard (single or broken power-law) electron energy distribution (Kataoka & Stawarz, 2005). However, quasar jets often have X-ray luminosities that are much higher than predicted by a simple synchrotron model. Figure 1.8 illustrates the prototypical radio through X-ray spectral energy distribution for a knot in a kpc-scale quasar jet, that of knot WK7.8 in PKS 0637–752. A single or broken power-law spectrum cannot fit the radio, optical and X-ray data-points. For this reason, an interpretation of the SED in terms of synchrotron emission from a single standard electron population is not viable (Schwartz et al., 2000). Thermal Bremsstrahlung is ruled out because the required electron density is not consistent with the upper limit on rotation measure (Schwartz et al., 2000). The synchrotron self-Compton mechanism can provide an adequate fit to the spectrum only if the magnetic field in the jet is orders of magnitude below

the equipartition value, or the jet emission is significantly Doppler de-beamed (Schwartz et al., 2000). Highly sub-equipartition magnetic fields are unfavourable because the energy requirements are much greater than in the equipartition models. Moreover, models of magnetically driven jets predict equipartition between Poynting and kinetic energy flux, and this implies approximate equipartition between the magnetic and particle energy densities (Vlahakis & Königl, 2004). However, in this context it should be noted that the equipartition condition in magnetically accelerated jets is met asymptotically and does not refer necessarily to discrete emitting volumes.

These issues with standard emission mechanisms have led to the development of a model in which the X-ray emission is said to be produced by inverse Compton scattering of cosmic microwave background photons in a jet with bulk Lorentz factor $\Gamma \gtrsim 10$ (Tavecchio et al., 2000b). This is the so-called IC/CMB model of jet X-ray emission.

1.6.3 IC/CMB Model

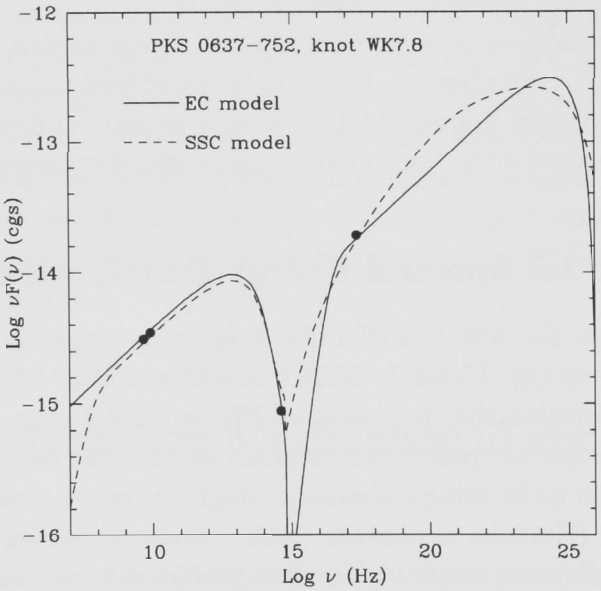

Figure 1.8: Radio to X-ray spectral energy distribution of knot WK7.8 in the kpc-scale jet of the PKS 0637–752 from Tavecchio et al. (2000b)

.

The mathematical description of the IC/CMB model is given in §2.6.1. The IC/CMB model is favoured over the synchrotron self Compton model because it allows the magnetic field in the jet to be near the equipartition value, and it also implies a lower total power than the SSC model (Ghisellini & Celotti, 2001). In addition, the IC/CMB model is favoured over synchrotron models because the

IC/CMB model requires a standard power-law electron energy distribution while the synchrotron models require either two separate electron populations, or a non-standard electron energy distribution that flattens (i.e. turns up) towards higher energy.

While the IC/CMB model has achieved a great deal of support, a number of problems with the simple one-zone IC/CMB model have been identified. Below I discuss each of these problems, and the possible remedies that have been put forward. Some of the following issues are addressed in Chapter 4. While it is true that not all of the following problems are addressed in this thesis, it is important to acknowledge all the major issues. The following provides a brief overview of the major issues relating to the IC/CMB model for quasar jet X-ray emission.

Problem 1: Frequency Independent Knot Profiles As discussed in §1.4.1, an important problem arises from the fact that the size of jet knots at radio, optical and X-ray wavelengths are similar. This is unexpected because the cooling length of the electrons responsible for IC/CMB emission ($\gamma \sim 100$) is comparable to, or longer than the size of the jet, so that virtually continuous jet X-ray emission would be expected in the IC/CMB model. This issue has been discussed in detail in §1.4.1, and will not be repeated here. As has been discussed, the remedies required to solve this problem, i.e. clumping of jet material, may reduce the appeal of the IC/CMB model over other models (Stawarz et al., 2004).

Problem 2: Inconsistent Jet Speed Estimates The IC/CMB model requires jet Lorentz factors of order $\Gamma \sim 5 - 25$ on scales of hundreds of kpc (Kataoka & Stawarz, 2005). However, this estimate of kpc-scale jet Lorentz factor is inconsistent with the estimates of kpc-scale jet speeds obtained in studies of the radio emission from large-scale jets. Wardle & Aaron (1997) analysed jet to counter-jet flux density ratios in images of 3CR quasars. By modeling the distribution of brightness ratios assuming an isotropic distribution of viewing angles, an estimate of the kpc-scale quasar jet speed was obtained, with a best fit value of $\beta \approx 0.7$. In addition, Wardle & Aaron (1997) analysed the jet to lobe brightness ratios in a complete sample of 3C quasars, and found an upper limit to the average jet speed of 0.95c ($\Gamma < 3$). Similarly, Hardcastle et al. (1999) analysed the jet prominences (jet to lobe flux density ratios) of a large sample of FRII radio galaxies with $z < 0.3$. They find $\Gamma \sim 1.2 - 1.4$ provides the best fit to the data.

To reconcile the inconsistent jet speed estimates, transverse velocity structure within the jet is invoked. This is the so-called "spine-sheath model". In this model, most of the radio emission is associated with a slow moving sheath or boundary layer, while the IC/CMB X-ray emission originates in a faster spine. However, if this is the case, the simple one-zone IC/CMB model is not applicable. The exact fraction of radio emission associated with the spine, and the velocity profile of the jet significantly affects the derived jet parameters. In addition, it is possible that

the synchrotron photons produced in the slower moving sheath make a significant contribution to the external radiation field that is inverse Compton scattered by the faster moving spine to produce the observed X-ray emission.

Evidence for transverse velocity structure with radio emission originating in the outer layers of the jet has been found in the nearby FRII radio galaxy 3C 353. The polarization fraction, position angle and total intensity profiles across the jets indicate that most of the radio emission is produced at the jet edges within a boundary shear layer (Swain et al., 1998).

Problem 3: Redshift Dependence The IC/CMB model makes strong, testable predictions about the redshift dependence of kpc-scale X-ray jets. The model predicts that the X-ray surface brightness of a jet should be redshift independent, because the CMB energy density increases as $(1+z)^4$, which counter-acts the usual decrease of surface brightness as $(1+z)^{-4}$. Therefore, the number of high redshift kpc-scale X-ray jet detections should increase with redshift. Moreover, the ratio of X-ray to radio surface brightness should increase with redshift as $(1+z)^4$ (Schwartz, 2002). So far, these predictions of the IC/CMB model have not been observed (Kataoka & Stawarz, 2005). A project is currently underway to image a large number of radio-loud quasars with $z > 2.5$ in the area common to both FIRST (Faint Images of the Radio Sky at Twenty-cm) and SDSS (Sloan Digital Sky Survey). The sample contains 134 objects ranging in redshift up to z = 4.7. One of the major goals of this program is to find new high redshift jets to test the IC/CMB model through observations with Chandra (Wardle et al., 2008).

An anti-correlation between the Doppler factor calculated using the IC/CMB model and redshift has been observed (Kataoka & Stawarz, 2005). It may be possible that the anti-correlation reflects a true evolution of quasar jets. However, the anti-correlation between Doppler factor and redshift may simply be an artefact of inappropriately applying the IC/CMB model to quasar jets (Kataoka & Stawarz, 2005).

Problem 4: High Doppler Factor $\Rightarrow$ Mpc Quasar Jets. As discussed in §3.7.3, the high Doppler factors required by the IC/CMB model imply small angles to the line of sight ($\theta \lesssim 5°$), which in some cases implies the deprojected jet lengths are of order 1 Mpc or greater (eg. PKS 0637–752, PKS 1127–145, B2 0738+313). Such large jet lengths are not common among FRII radio galaxies. In addition, small jet viewing angles are not expected in lobe dominated quasars such as 3C207 and 3C9 (see Kataoka & Stawarz, 2005).

Problem 5: The Exceptional FRII Radio Galaxy 3C 353 X-ray knots have been observed in the jet and counter-jet of the FRII radio galaxy 3C 353 (Kataoka et al., 2008). The SEDs of these knots are similar to quasar jet knots, with X-ray flux densities much higher than the extrapolated radio to optical continuum. The

fact that the emission is observed in both the jet and counter-jet is incompatible with an IC/CMB interpretation, and points to a synchrotron origin for the X-ray jet photons (Kataoka et al., 2008) which would require a non-standard electron distribution.

It should be noted that in this object the X-ray emission appears to originate from a narrower region than the radio emission, and there are significant (kpc-scale) offsets between the peaks of the X-ray and radio knots, with the X-ray emission peaking closer to the core than the associated radio peaks (Kataoka et al., 2008).

1.6.4 Alternative Models for Quasar Jet X-ray Emission

Due to the potential problems with the IC/CMB model, a number of alternative models have been proposed. In this section I present a brief discussion of some of the alternative models. While not all of the following models are addressed in this thesis, it is important to at least briefly acknowledge the variety of models that have been proposed.

Synchrotron Emission from Non-Standard Electron Spectra

Synchrotron models for quasar jet X-ray emission require non-standard electron spectra that flatten towards higher energies. There have been a number of suggestions as to how such an electron spectrum may be produced. Dermer & Atoyan (2002) proposed that the flattening of the spectrum at high energies could be the result of a reduced cooling rate in high energy electrons due to the Klein-Nishina scattering cross section (see §2.4.1). If inverse Compton cooling dominates, a flattening in the electron spectrum is formed at electron energies where Klein-Nishina (KN) effects become important. This results in a flattening of the synchrotron spectrum between optical and X-ray frequencies. However, this model requires that the photon energy density in the jet rest frame is greater than the magnetic energy density. For this to occur, Doppler boosting of the CMB is required, implying a large jet Lorentz factor. With a large jet Lorentz factor the required X-ray emissivity is already produced via the IC/CMB process, so that a flattened synchrotron spectrum is no longer required (Harris & Krawczynski, 2006).

Stawarz & Ostrowski (2002) and Stawarz et al. (2004) proposed that turbulent second-order Fermi acceleration in the jet boundary layer produces a power-law continuum with a bump at high energy where the acceleration timescale equals cooling timescale. Such a particle spectrum would produce an excess of X-rays relative to the radio and optical, as observed in quasar jets.

Two Component Synchrotron Models

Atoyan & Dermer (2004) have suggested that the quasar jet SEDs represent emission from two distinct electron populations: a standard downward curving electron spectrum accounting for the radio to optical continuum, and a second high energy population with a restricted energy range responsible for the observed X-ray emission. They proposed that the broadband radio to X-ray synchrotron emission in quasar jets is powered by collimated beams of ultrahigh energy neutrons and γ-rays formed in the subparsec-scale jets. The decay of the neutral beam in the intergalactic medium drives relativistic shocks to accelerate nonthermal electrons of the ambient medium. A second synchrotron component arises from the injection of leptons with Lorentz factors $\gamma \gtrsim 10^7$ that appear in the extended jet in the process of decay of ultrahigh energy γ-rays.

Aharonian (2002) proposed that the observed X-ray flux could be synchrotron emission from a population of ultra high energy protons ($\gamma_p \gtrsim 10^9$) in a $\gtrsim 1$ mG magnetic field.

1.6.5 Summary

In summary, the X-ray emission mechanism in quasar jets remains a topic for debate, and has important implications for the understanding of extragalactic jets in general. As expressed by Kataoka et al. (2008): "A complete, self-consistent model for the X-ray emission of extragalactic jets still remains elusive."

1.7 Thesis Overview

My thesis is based on the detailed study and interpretation of the spatially resolved radio, optical and X-ray emission from kpc-scale jets and hotspots in high power, Fanaroff-Riley class II objects. As mentioned above, one of the major science goals for the *Chandra* X-ray Observatory is to compare the X-ray structure of AGN jets with their radio images[5]. This thesis provides a significant contribution towards fulfilling that goal.

As part of the Marshall et al. quasar jet survey (Marshall et al., 2005), we observed the southern survey target sources using the new 12mm receivers on the Australia Telescope Compact Array (ATCA). I was involved with the radio observations and data reduction, and in return was given access to X-ray data from the deep follow-up *Chandra* observations of several X-ray jets selected from the snapshot survey. For my thesis, two sources were selected for detailed study: PKS 1421–490 and PKS 2101–490, with the aim of confronting jet models with the highest quality radio, optical and X-ray data for these individual sources.

[5]Scientific Requirements for the Calibration of AXAF, MSFC-RQMT-2229, August 2 1995 `http://cxc.harvard.edu/cal/docs/cal_sci_req.html`

The plan of the thesis is as follows: in chapter 2 I present an overview of the theoretical background required for the following chapters; in chapter 3 I present a detailed physical analysis of the radio to X-ray emission from the radio galaxy PKS 1421–490; in chapter 4 I present a detailed physical analysis of the radio to X-ray emission from the radio galaxy PKS 2101–490; and in chapter 5 I present the conclusions of the thesis.

Chapter 2

Emission Mechanisms

The study of the universe is made possible by the detection of photons, and the measurement of intensity and/or flux density as a function of frequency, angular position and time. In doing so we hope to model the conditions in which the photons were produced, and thereby obtain a physical understanding of the phenomena being studied. It is therefore vitally important to understand in detail the relevant emission mechanisms. The purpose of this chapter is to set out some of the theory of synchrotron and inverse Compton emission, and list some important references on the subject. The derivations presented in this chapter are not original, and are largely based on lecture notes[1] by Geoff Bicknell. However, §2.3.3 and §2.4.5 are my own developments, and are included to aid understanding of the subject, and in the case of §2.4.5, to dispel an apparently common misconception about synchrotron Self Compton emission. Detailed treatment of the relevant emission mechanisms can be found in Rybicki & Lightman (1979).

[1] http://www.mso.anu.edu.au/ geoff/HEA/HEA.html

2.1 Definitions

Throughout this chapter, and the rest of the thesis, I make use of many parameters, constants and abbreviations. Here I list and describe the most common of these, so the reader may refer back to this section if they are unsure of the meaning of a particular symbol.

Description of the Radiation Field

ν	Frequency	
ϵ	Photon energy	$\epsilon = h\nu$
ω	Angular Frequency	$\omega = 2\pi\nu$
j_ν	Emissivity	$\frac{dE}{dt\, d\nu\, dV\, d\Omega}$
$\mathbf{I}_\nu$	Specific Intensity	$\frac{dE}{dt\, d\nu\, dA\, d\Omega}$
$\mathbf{F}_\nu$	Flux Density	$\frac{dE}{dt\, d\nu\, dA}$
$\mathbf{L}_\nu$	Luminosity Density	$\frac{dE}{dt\, d\nu}$
α	Spectral Index	Used to describe power-law spectra of the form $F_\nu \propto \nu^{-\alpha}$

Physical Parameters

B Magnetic field strength

Ω_0 Non-relativistic gyro-frequency

$\Omega_0 = \frac{qB}{m}$ (S.I.) $\Omega_0 = \frac{qB}{mc}$ (cgs)

γ Lorentz factor of an individual electron relative to the jet rest frame

$\gamma = (1 - \beta_e^2)^{-1/2}$

Γ Lorentz factor of the jet bulk flow relative to the lab frame

$\Gamma = \left(1 - \beta_{\text{jet}}^2\right)^{-1/2}$

δ Doppler beaming factor of the jet

$\delta = \frac{1}{\Gamma\left(1-\beta_{\text{jet}} \cos\theta\right)}$ (θ = angle between line of sight and jet velocity).

D_L Luminosity distance. Defined such that:

$L_\nu = F_\nu \, 4\pi D_L^2$

D_A Angular size distance. Defined such that:

$D_A = \frac{d}{\phi} \quad \left(D_A = \frac{D_L}{(1+z)^2}\right)$

where d is the objects' diameter, and ϕ is the measured angular size.

Constants

q_e	Charge of an electron	1.6×10^{-19} C
m_e	Mass of an electron	9.1×10^{-31} kg
σ_T	Thompson cross-section	6.6524×10^{-29} m
ϵ_0	Permittivity of free space	8.854×10^{-12} $s^4A^2kg^{-1}m^{-3}$
r_e	Classical electron radius	$\frac{1}{4\pi\epsilon_0}\frac{q_e^2}{m_e c^2} = 2.818 \times 10^{-15}$ m

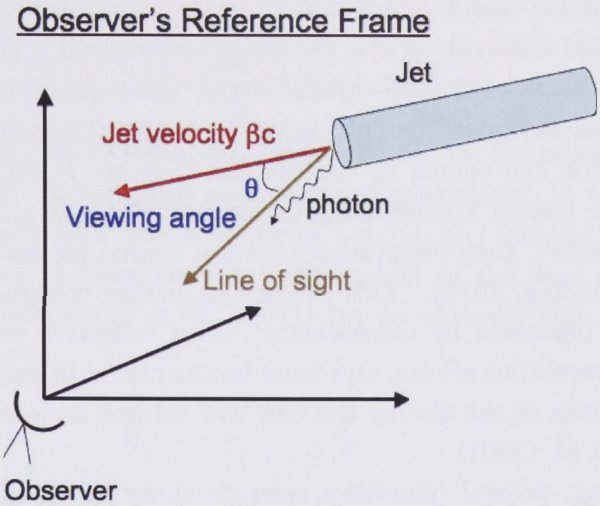

Figure 2.1: Schematic diagram of the observer's reference frame, showing the definition of the jet viewing angle.

2.2 Relativistic Effects on the Observed Properties of the Radiation Field

The effects of relativistic corrections to the radiation field are summarized in Appendix B of Urry & Padovani (1995) and Appendix C of Begelman et al. (1984). In this section I give a detailed description of the relativistic effects and their origins, to aid in understanding the correct application of these formulae.

For an optically thin source of length L along the line of sight subtending solid angle Ω_S,

$$I_\nu = \int_0^L j_\nu ds \tag{2.1}$$

$$F_\nu = \int_{\Omega_S} I_\nu d\Omega \tag{2.2}$$

$$= \int_{\Omega_S} \int_0^L j_\nu ds d\Omega \tag{2.3}$$

When modeling the emission produced by matter with a relativistic velocity, we must consider two distinct effects: Lorentz transformations and light travel time effects. Light travel time effects are not relativistic effects — they arise due to the finite speed of light. Light travel time effects are due to the emitter "chasing" the photons it emits. Light travel time effects often have a significant impact on the appearance of a relativistic source of radiation. Superluminal motion is a good example of a situation in which light travel time effects greatly modify the appearance of a relativistically moving object.

The relationship between the observed intensity distribution and the source can be quite complicated when relativistic velocities are involved. "For inhomogeneous sources in which the velocity and optical depth are a function of position, the distribution of intensity must be calculated by writing the equation of transfer for any point within the source in coordinates that are locally co-moving with that element of the source, transforming these coordinates to a frame at rest with respect to the observer, then integrating over the source volume perceived by the observer. " (De Young, 1972). This process is further complicated by the fact that "the volume perceived by the observer" is an "effective volume", since it is affected by light travel time effects, and must be calculated in terms of the retarded position. The process of calculating the effective volume is described in detail by Georganopoulos et al. (2001).

In the following, primed quantities refer to those in the rest frame. For a source of radiation with Doppler factor δ at redshift z the emitted frequency ν' and observed frequency ν are related by the following equation:

$$\nu = \left(\frac{\delta}{1+z}\right)\nu' \tag{2.4}$$

It can be shown that the ratio j_ν/ν^2 is a general relativistic invariant. That is

$$\frac{j_\nu}{\nu^2} = \frac{j'_{\nu'}}{\nu'^2} \tag{2.5}$$

(Rybicki & Lightman, 1979). Combining equations 2.4 and 2.5 we obtain

$$j_\nu = \left(\frac{\delta}{1+z}\right)^2 j'_{\nu'} \tag{2.6}$$

where $j'_{\nu'}$ is the emissivity measured in the jet frame at the emitted frequency ν', and j_ν is the corresponding emissivity measured in the lab frame at the observed frequency ν. For an optically thin discrete source the specific intensity is

$$I_\nu = \left(\frac{\delta}{1+z}\right)^3 I'_{\nu'} \tag{2.7}$$

(Rybicki & Lightman, 1979). The flux density of a discrete source in relativistic motion is calculated as

$$F_\nu = \int_{\Omega_S}\int_0^L j_\nu ds d\Omega \tag{2.8}$$

$$= \left(\frac{\delta}{1+z}\right)^3 \int_{A_S}\int_0^{L'} j'_{\nu'} ds' \frac{dA'}{d_A^2} \tag{2.9}$$

$$= \frac{\delta^3(1+z)}{D_L^2}\int_{V_S} j'_{\nu'} dV' \tag{2.10}$$

since

$$d\Omega = \frac{dA'}{d_A^2} = (1+z)^4 \frac{dA'}{d_L^2} \tag{2.11}$$

However, in the case of a continuous jet the source boundaries are stationary while the fluid flow within those boundaries is relativistic. In this situation, the fluid emissivity transforms as per equation 2.6, but the integration path between the (stationary) source boundaries is independent of the fluid velocity (see Appendix A of Georganopoulos et al., 2001). For an optically thin continuous jet or stationary pattern

$$I_\nu = \frac{\delta^2}{(1+z)^3} I'_{\nu'} \tag{2.12}$$

$$F_\nu = \frac{\delta^2(1+z)}{D_L^2} \int_{V_S} j'_{\nu'} dV' \tag{2.13}$$

Another interesting relativistic effect relates time intervals between the lab frame and the rest frame. For a relativistic source approaching the observer, a time interval measured in the lab frame Δt is related to the time interval in the rest frame $\Delta t'$ via

$$\Delta t' = \delta \Delta t \tag{2.14}$$

At first this may seem counter-intuitive, since relativistic time dilation suggests that time intervals in the lab frame should be longer than time intervals in the rest frame. However, the time intervals observed in the lab frame are shorter than time intervals in the rest frame (even after taking time dilation into account) as a result of light travel time effects, since the emitting plasma "chases" the photons it has emitted (Urry & Padovani, 1995).

In §4.2.3 we consider the escape time-scale for particles in the jet to travel through a distance L. In this case, the conversion between lab frame and rest frame does not involve light travel time effects, since we are not considering the time between observed photons relative to the time between emitted photons. Hence time dilation is the only effect, and the proper time for electrons in the jet to travel through a distance L is $\tau'_{\rm esc} = L/\Gamma\beta_{\rm jet}c$.

2.2.1 The Doppler Factor

As discussed above, relativistic effects on the radiation field are accounted for by a single factor, the Doppler factor $\delta = [\Gamma(1-\beta\cos\theta)]^{-1}$, where Γ is the bulk Lorentz factor of the emitting material, and θ is the angle between the source velocity and the line of sight. Figure 2.2(a) illustrates the dependence of Doppler factor on Lorentz factor for fixed values of the viewing angle, while Figure 2.2(b) illustrates the dependence of Doppler factor on viewing angle for fixed values of the Lorentz

factor. These plots show that for relatively high Lorentz factors ($\Gamma \gtrsim 5$), the Doppler factor is very sensitive to changes in viewing angle.

Figure 2.2(c) illustrates the relationship between viewing angle and Lorentz factor for fixed Doppler factor. This figure serves to illustrate two points. Firstly, it can be seen that for a given Doppler factor, there is a maximum viewing angle. This maximum angle is given by $\theta_{\max} = \arcsin(1/\delta)$ and corresponds to the situation in which $\Gamma = \delta \iff \beta = \cos\theta$. If $\delta \gtrsim 10$ as calculated for the jet of PKS 0637–752 (Tavecchio et al., 2000b), $\theta_{\max} \approx 6°$. The maximum viewing angle is plotted as a function of Doppler factor in Figure 2.2(d). The second point to note from Figure 2.2(c) is that for a given Doppler factor, relatively small uncertainty in θ results in a large uncertainty in Γ. In other words, the relationship between δ and Γ is very sensitive to the viewing angle. As an example, consider the situation in which $\delta = 10$ and $\theta = 5° \pm 1°$, then $5.8 < \Gamma < 35$. Typically in the analysis of quasar jet SEDs, it is the Doppler factor that is determined, and conversion to Lorentz factor is made via the assumption $\Gamma = \delta$. This assumption is made because in that case $\theta = \theta_{\max}$ and therefore $\Gamma = \delta$ is the most probable situation. For a given Doppler factor $\Gamma > \delta/2$, so that the assumption $\Gamma = \delta$ will be within a factor of 2 of the minimum possible value. However, as noted above, much larger Lorentz factors can be obtained with only small reductions in the viewing angle.

There are two further points to note from Figure 2.2(a). Firstly, for a given viewing angle θ and Doppler factor Γ there are two possible values for the Lorentz factor

$$\Gamma_{1,2} = \frac{1 \pm \sqrt{1 - \sin^2\theta\,(1 + \delta^2\cos^2\theta)}}{\delta \sin^2\theta} \tag{2.15}$$

One final point to note from Figure 2.2(a) is that for a given viewing angle, there is a maximum possible Doppler factor. The maximum Doppler factor is given by $\delta_{\max} = 1/\sin\theta$ and corresponds to the situation in which $\Gamma = \delta \iff \beta = \cos\theta$. The maximum Doppler factor as a function of viewing angle is plotted in Figure 2.2(e). For a given Lorentz factor, the emission will be enhanced for angles smaller than $\theta_{\delta=1} = \arccos\left(\frac{\Gamma-1}{\sqrt{\Gamma^2-1}}\right) \approx 54°, 25°$ for $\Gamma = 2, 10$ respectively. Hence, for moderate Lorentz factors, Doppler beaming can be important even at relatively large angles to the line of sight. However, as can be seen from Figure 2.2(b), at large angles to the line of sight, while Doppler beaming is possible, the Doppler factor will be relatively small.

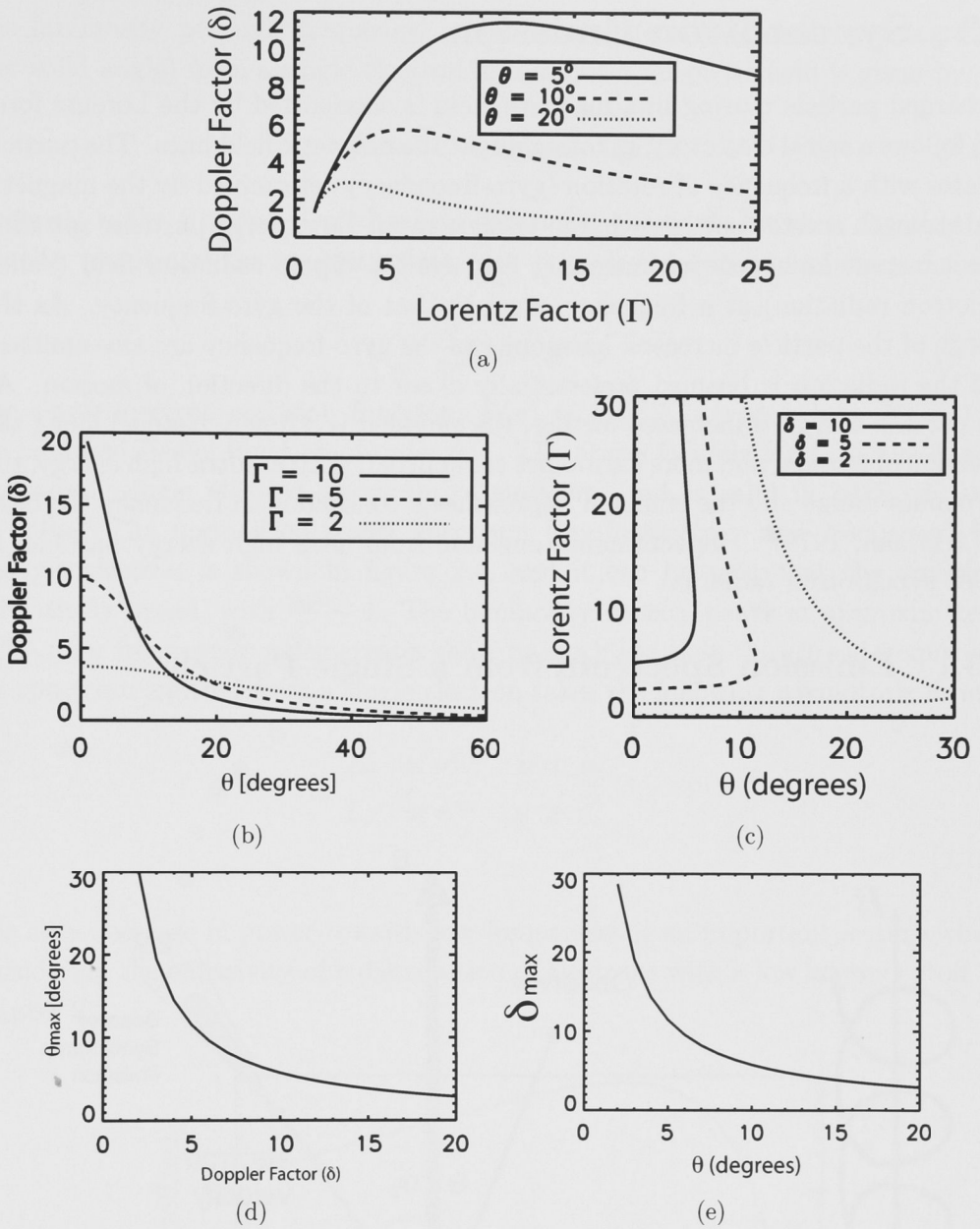

Figure 2.2: (a) Doppler factor as a function of Lorentz factor for fixed values of the viewing angle. This plot is relevant to changes in brightness along a single, straight jet due to changes in the Lorentz factor. (b) Doppler factor as a function of viewing angle for fixed values of the Lorentz factor. This plot is relevant to changes in brightness for a set of jets with the same Lorentz factor but viewed from different angles. (c) Lorentz factor as a function of viewing angle for fixed values of the Doppler factor. This plot is relevant to the conversion from Doppler factor to Lorentz factor. (d) Maximum viewing angle for given Doppler factor. (e) Maximum Doppler factor for given viewing angle.

2.3 Synchrotron Emission

A charged particle moving in a magnetic field is accelerated by the Lorentz force and follows a spiral trajectory, gyrating about the magnetic field lines. The particle gyrates with a frequency of rotation (gyro-frequency) determined by the magnetic field strength and the particles charge-to-mass ratio. Low energy particles spiraling in a constant homogeneous magnetic field emit a dipole radiation field (called cyclotron radiation) at a frequency equal to that of the gyro-frequency. As the energy of the particle increases, harmonics of the gyro-frequency are also emitted, and the radiation is beamed preferentially closer to the direction of motion. As the particle energy is increased further, the emission is strongly beamed along the direction of motion, and more harmonics are emitted, until at ultra-high energy, the harmonics merge and the emission approaches a continuum in frequency (Rybicki & Lightman, 1979). The continuum emission from ultra high energy particles is called synchrotron radiation.

2.3.1 Emission Spectrum from a Single Particle

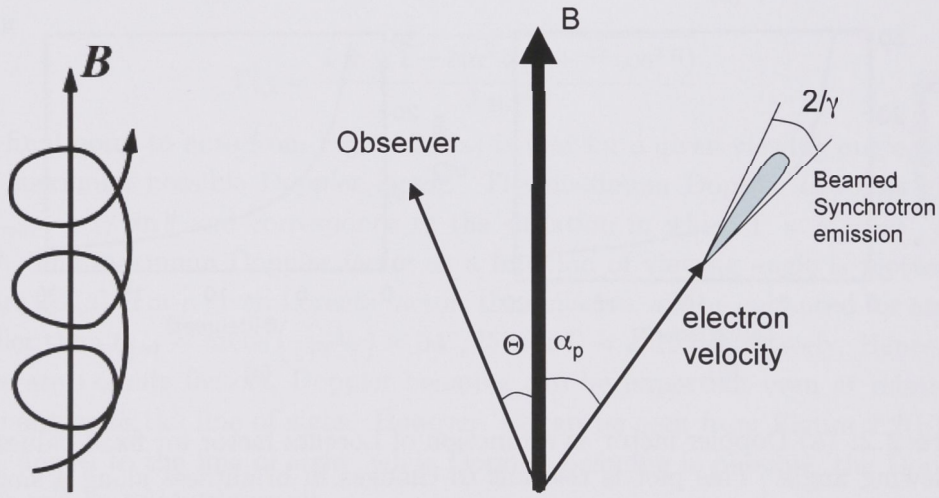

Figure 2.3: (a) Spiral trajectory of electron around magnetic field line. (b) Electron velocity vector relative to magnetic field line, showing the definition of the pitch angle α_p. The emission is beamed into a cone of half angle $1/\gamma$.

Figure 2.3 illustrates the situation of a particle spiraling in a magnetic field, and the notation used to describe the particles trajectory. The forward emission is beamed within a cone of half-angle $1/\gamma$ where γ is the electron Lorentz factor.

The luminosity per unit frequency, or luminosity density (emissivity integrated over solid angle) from a single electron in a uniform magnetic field is given by

$$L_\nu = 2\pi\sqrt{3}\, c\, m_e\, r_e\, \Omega_0 \sin\alpha_p F(x) \tag{2.16}$$

where α_p is the (constant) pitch angle defined as the angle between the electron velocity vector and the magnetic field, $x = \frac{\nu}{\nu_c}$, ν_c is the critical frequency defined as

$$\nu_c = \frac{3}{4\pi}\Omega_0 \gamma^2 \sin\alpha_p \tag{2.17}$$

The single electron emission function, $F(x) = x\int_x^\infty K_{5/3}(z)dz$ where $K_{5/3}(z)$ is the modified Bessel function of order 5/3. The above formula for L_ν is the angle-integrated, single electron spectrum of emission, and is valid in both cgs and SI units. The normalized power spectrum (luminosity per unit frequency) for a single electron is shown in figure 2.4, and it can be seen that the emission is relatively broad, with $\frac{\Delta\nu}{\nu} \sim 1$. The luminosity density peaks at approximately $0.29\nu_c$. For frequencies much greater than, or much less than the critical frequency, the spectrum emitted from a single electron takes the following asymptotic forms.

$$\begin{aligned} L_\nu &\propto \nu^{1/3} \quad \nu \ll \nu_c \\ L_\nu &\propto e^{-\nu} \quad \nu \gg \nu_c \end{aligned} \tag{2.18}$$

The slow decrease in power towards low frequencies is an important feature when considering the emissivity of a distribution of electrons with a low energy cutoff in chapter 3.

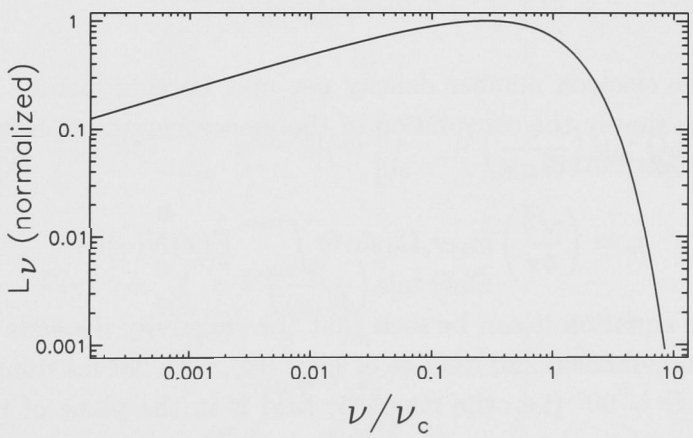

Figure 2.4: Plot of single electron synchrotron power spectrum. This is the spectrum of emission in all directions from a single electron. The integral of this function gives the total luminosity, or energy loss rate, for a single electron.

Integrating equation (2.16) gives the total luminosity, or energy loss rate, for a single electron in a uniform magnetic field (again, valid in cgs and SI units)

$$L = -\frac{dE}{dt} = 2\sigma_T c\gamma^2\beta^2 U_B \sin^2\alpha_p \tag{2.19}$$

where $U_B = B^2/2\mu_0$ (SI) $= B^2/8\pi$ (cgs) is the magnetic energy density. Averaging over an isotropic pitch angle distribution, $P(\alpha_p) = (1/2)\sin\alpha_p d\alpha_p$

$$L = -\frac{dE}{dt} = \frac{4}{3}\sigma_T c\gamma^2\beta^2 U_B \tag{2.20}$$

The radiative cooling timescale, or radiative lifetime $\tau_{\rm rad}$ of an electron is usually defined as

$$\tau_{\rm rad} = \frac{E}{-dE/dt} = \frac{3}{4}\frac{m_e c}{\sigma_T\gamma\beta^2 U_B} \tag{2.21}$$

This is the time taken for any given electron to lose half of its initial energy.

2.3.2 Emission Spectrum from an Electron Population

To calculate the emission spectrum for a distribution of electrons it is first assumed that the pitch angle distribution is isotropic. Let Θ be the angle between the magnetic field and the line of sight. The emission into a solid angle around Θ has contributions from electrons with different pitch angles, but electrons with $\alpha_p \approx \Theta$ will contribute most to the spectrum. By integrating over the pitch angle distribution it can be shown that for a mono-energetic electron population with isotropic pitch angle distribution, the emissivity at an angle Θ to the magnetic field is

$$j_\nu = \left(\frac{\sqrt{3}}{4\pi}\right) n_e m_e c r_e \Omega_0 \sin\Theta F(x) \tag{2.22}$$

Let $N(\gamma)$ be the electron number density per unit Lorentz factor. In that case, the emissivity is simply the convolution of the mono-energetic spectrum with the Lorentz factor distribution

$$j_\nu = \left(\frac{\sqrt{3}}{4\pi}\right) m_e c r_e \Omega_0 \sin\Theta \int_{\gamma_{\rm min}}^{\gamma_{\rm max}} F(x)N(\gamma)d\gamma \tag{2.23}$$

From the above equation it can be seen that the emissivity depends on the angle between the magnetic field and the line of sight (Θ), with the maximum emissivity occuring when $\Theta = 90°$ (i.e. the magnetic field is in the plane of the sky), and dropping to zero when the magnetic field is directed along our line of sight. We must therefore assume some form for the magnetic field distribution. The theory of synchrotron radiation predicts that if the magnetic field does not change direction significantly within the emitting volume, the fractional linear polarization will be of order 55%. Such high fractional linear polarization is rarely, if ever, observed

in kpc-scale radio jets. Polarization fractions of order 5 - 10% are more common. This lower level of linear polarization is ascribed to changes in direction of the magnetic field within the emission region. To account for the changes in magnetic field direction, it is assumed that the magnetic field takes a random, isotropic distribution; that is, the magnetic field is uniformly distributed over solid angle, i.e. $P(\Theta)d\Theta = (1/2)\sin\Theta d\Theta$.

To calculate the angle averaged emission spectrum from a plasma in which the pitch angle and magnetic field are isotropic, the following change of variables is made:

$$\text{Let} \quad y = \frac{2}{3}\frac{\omega}{\Omega_0}\gamma^{-2} = \frac{\nu}{\nu_c}\sin\alpha_p \approx \frac{\nu}{\nu_c}\sin\Theta \tag{2.24}$$

$$\Rightarrow \gamma = \left(\frac{2\omega}{3\Omega_0}\right)^{1/2} y^{-1/2} \tag{2.25}$$

$$\Rightarrow d\gamma = -\frac{1}{2}\left(\frac{2\omega}{3\Omega_0}\right)^{1/2} y^{-3/2}dy \tag{2.26}$$

where we have made the substitution $\Theta \approx \alpha_p$ which is valid provided $\gamma >> 1$. Now making the change of variables in equation (2.23)

$$j_\nu = \left(\frac{m_e r_e c}{4\sqrt{\pi}}\right)\nu^{1/2}\Omega_0^{1/2}\int_{y_2}^{y_1} y^{-3/2}N(\gamma)F\left(\frac{y}{\sin\Theta}\right)\sin\Theta dy \tag{2.27}$$

where

$$y_{1,2} = \left(\frac{4\pi\nu}{3\Omega_0}\right)\gamma_{1,2}^{-2} \tag{2.28}$$

The angle averaged emissivity is calculated as

$$\langle j_\nu\rangle = \frac{1}{4\pi}\int_{4\pi} j_\nu d\Omega = \frac{1}{4\pi}\int_0^{2\pi}\int_0^{\pi} j_\nu \sin\Theta d\Theta d\phi \tag{2.29}$$

$$= \int_0^{\pi/2} j_\nu \sin\Theta d\Theta \tag{2.30}$$

Thus,

$$\langle j_\nu\rangle = \left(\frac{m_e r_e c}{4\sqrt{\pi}}\right)\nu^{1/2}\Omega_0^{1/2}\int_{y_2}^{y_1} y^{-3/2}N(\gamma)\left[\int_0^{\pi/2} F\left(\frac{y}{\sin\Theta}\right)\sin^2\Theta d\Theta\right]dy \tag{2.31}$$

Now, write

$$\bar{F}(y) = \int_0^{\pi/2} F\left(\frac{y}{\sin\Theta}\right)\sin^2\Theta d\Theta \tag{2.32}$$

$$= \int_0^{\pi/2}\left[\frac{y}{\sin\Theta}\int_{\frac{y}{\sin\Theta}}^{\infty} K_{5/3}(z)dz\right]\sin^2\Theta d\Theta \tag{2.33}$$

$$= y\int_y^{\infty}\left(1-\frac{y^2}{t^2}\right)^{1/2} K_{5/3}(t)dt \tag{2.34}$$

Then

$$\langle j_\nu\rangle = \left(\frac{m_e r_e c}{4\sqrt{\pi}}\right)\nu^{1/2}\Omega_0^{1/2}\int_{y_2}^{y_1} y^{-3/2}N(\gamma)\bar{F}(y)dy \tag{2.35}$$

Power-law Synchrotron Spectrum

In the case of a pure power law electron energy distribution with $N(\gamma) = K_e\gamma^{-a}$ for $\gamma_1 < \gamma < \gamma_2$, an analytic expression can be found for frequencies that satisfy $\gamma_1^2\Omega_0 << \nu << \gamma_2^2\Omega_0$

$$\langle j_\nu \rangle = 4\pi m_e c r_e C_2(a) K_e \Omega_0^{\frac{a+1}{2}} \nu^{-\frac{(a-1)}{2}} \tag{2.36}$$

where

$$C_2(a) = \frac{3^{a/2}}{2^{\frac{a+13}{2}}\pi^{\frac{a+2}{2}}} \frac{\Gamma_{\rm fn}\left(\frac{a+1}{4}\right)\Gamma_{\rm fn}\left(\frac{a}{4}+\frac{19}{12}\right)\Gamma_{\rm fn}\left(\frac{a}{4}-\frac{1}{12}\right)}{\Gamma_{\rm fn}\left(\frac{a+7}{4}\right)} \tag{2.37}$$

$$= 4.01 \times 10^{-3} \text{ for } a = 2 \tag{2.38}$$

and $\Gamma_{\rm fn}(z) = \int_0^\infty t^{z-1}e^{-t}dt$ is the Gamma function (not to be confused with the jet Lorentz factor Γ as defined at the start of this chapter).

2.3.3 Synchrotron Emissivity Distribution Function from a Power Law Electron Energy Distribution

I have used equation 2.35 in a Fortran program to numerically calculate model synchrotron spectra. However, it is instructive to take this equation one step further by making another change of variables. For a given observing frequency ν_{obs} and gyrofrequency Ω_0 we can use equation (2.17) to define a corresponding "critical Lorentz factor" $\gamma_c = \sqrt{\frac{4\pi\nu_{obs}}{3\Omega_0}}$. We now change the variable of integration in equation (2.35) to $\eta = \frac{\gamma}{\gamma_c}$.

$$y = \left(\frac{\gamma}{\gamma_c}\right)^{-2} = \eta^{-2}$$

$$dy = -2\eta^{-3}d\eta \tag{2.39}$$

$$N(\gamma) = K_e\gamma^{-a} = K_e\gamma_c^{-a}\eta^{-a} \tag{2.40}$$

$$\langle j_\nu \rangle = \left(\frac{m_e r_e c}{2\sqrt{\pi}}\right)\nu^{1/2}\Omega_0^{1/2}K_e\gamma_c^{-a}\int_{\eta_1}^{\eta_2}\eta^{-a}\bar{F}\left(\eta^{-2}\right)d\eta$$

In figure 2.5 I plot the function $\eta^{-a}\bar{F}\left(L^{-2}\right)$ for some relevant values of the electron energy index $a = 2$ and $a = 3$. The plotted function is proportional to $\partial j_\nu/\partial\gamma$ for a fixed observing frequency. This plot shows the relative contribution to the emissivity at a particular frequency ν_{obs} as a function of Lorentz factor, and serves to illustrate the point that for a given observing frequency, a large section of the electron energy distribution contributes to the observed flux density. In fact, for $a = 2$, 95% of the flux comes from the range $0.58\gamma_c < \gamma < 10.8\gamma_c$ — a range covering nearly a factor of 20 in Lorentz factor.

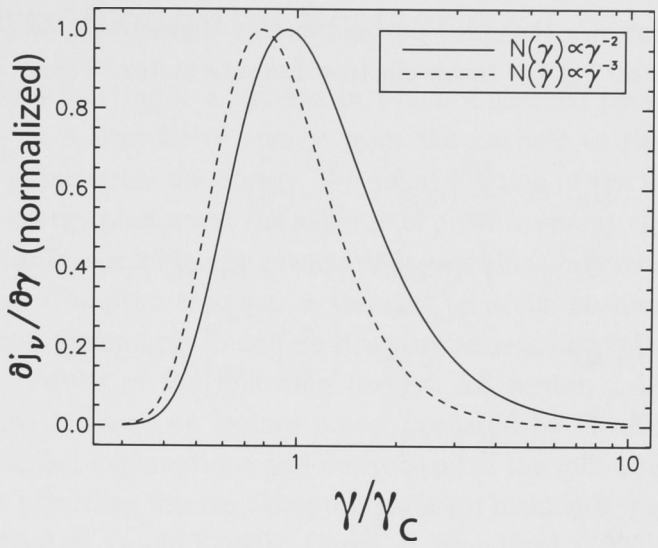

Figure 2.5: The emissivity per unit Lorentz factor as a function of Lorentz factor for two realistic forms of the electron distribution function N(γ). The value of γ_c is dependent on the observing frequency and the magnetic field strength and is given by $\gamma_c = \sqrt{\frac{4\pi\nu_{obs}}{3\Omega_0}}$.

The peak of the emissivity density curve is at 0.93 γ_c for $\alpha = 0.5$ and 0.78 γ_c for $\alpha = 1.0$. Thus, for typical jet spectra ($\alpha \sim 0.8$), to convert from an observed frequency to a characteristic Lorentz factor, it is appropriate to use

$$\gamma \approx \sqrt{\frac{\pi\nu}{\Omega_0}} \tag{2.41}$$

since these particles contribute most to the observed flux density.

2.3.4 Minimum Energy and Equipartition

Two important and related concepts in the study of synchrotron sources are minimum energy and equipartition. In this section I present a brief discussion of these concepts.

For a power-law electron spectrum, the flux density of a non-relativistic source of synchrotron emission of known volume depends on the magnetic field strength and the density of relativistic electrons. Measurements of the synchrotron spectrum alone cannot disentangle the magnetic field and electron density: the characteristics of the source can only be determined by adding another constraint. In the absence of detected inverse Compton emission, which independently constrains the electron density, an additional assumption must be made. For a given flux density and volume, there is a minimum total energy within the source required to produce the observed emission.

Let U_B be the magnetic energy density, U_e the energy density of the relativistic

electron population, U_p the total particle energy density, $C_E = U_e/U_p$, n_e the electron density, and $\langle\gamma\rangle$ the mean electron Lorentz factor. Then

$$U_B = \frac{B^2}{8\pi}(\text{cgs}) = \frac{B^2}{2\mu_0}(\text{SI}) \tag{2.42}$$

$$U_e = \int \gamma m_e c^2 N(\gamma) d\gamma = K_e m_e c^2 f(a, \gamma_1, \gamma_2) \tag{2.43}$$

$$f(a, \gamma_1, \gamma_2) = \frac{\gamma_1^{(2-a)}}{a-2}\left[1 - \left(\frac{\gamma_2}{\gamma_1}\right)^{(2-a)}\right] \quad a > 2 \tag{2.44}$$

$$= \ln\left(\frac{\gamma_2}{\gamma_1}\right) \quad a = 2 \tag{2.45}$$

$$U_p = (1 + C_E)U_e \tag{2.46}$$

$$n_e = \int N(\gamma) d\gamma = K_e \frac{\gamma_1^{(1-a)}}{a-1}\left[1 - \left(\frac{\gamma_2}{\gamma_1}\right)^{(1-a)}\right] \tag{2.47}$$

$$\langle\gamma\rangle = U_e/n_e m_e c^2 \approx \gamma_1 \frac{a-1}{a-2} \quad a > 2,\ \gamma_2 >> \gamma_1 \tag{2.48}$$

The constraint for minimum energy is

$$\frac{\partial}{\partial E}(U_B + U_p) = 0 \tag{2.49}$$

and when combined with the constraint from the observed flux density gives an expression for the magnetic field strength and electron density. An alternative assumption that is often made is that the magnetic and particle energy densities are in equipartition. That is, $U_B = U_p$. The source characteristics obtained using the assumption of equipartition are very close to the values obtained under the assumption of minimum energy, so that the terms "equipartition" and "minimum energy" are often used as synonyms.

Equipartition in a synchrotron source of volume V with a power-law electron energy distribution $N(\gamma) = K_e \gamma^{-a}$ $\gamma_1 < \gamma < \gamma_2$ implies

$$B_{\text{eq}} = \delta^{\frac{m+\alpha}{\alpha+3}}(1+z)^{\frac{\alpha-1}{\alpha+3}}\frac{m_e}{q}\left[(1+C_E)\frac{2c}{m_e}\frac{F_\nu \nu}{V}\frac{f(a,\gamma_1,\gamma_2)}{C_2(a)}D_L^2\right]^{1/(\alpha+3)} \tag{2.50}$$

where m=2 for a jet, and m=3 for a blob. For more sophisticated electron spectra, the equipartition magnetic field strength can be calculated numerically. However, the above expression for a power-law electron energy distribution is useful to show the dependence of the equipartition magnetic field strength on various parameters. In particular, this equation shows how sensitive the results are to the assumed values for γ_{min} and the proton content. From the above equations it can be seen that $B_{\text{eq}} \propto \gamma_1^{(1-2\alpha)/(3+\alpha)} C_E^{1/(3+\alpha)}$, provided $\gamma_2 >> \gamma_1$.

2.4 Inverse Compton Scattering

Inverse Compton scattering is a process in which a charged particle and photon collide resulting in a transfer of energy from the particle to the photon. This scattering process increases the energy of a small fraction of the ambient photons to produce high energy photons at the expense of particle energy. Inverse Compton scattering necessarily occurs in any plasma that contains photons and high energy particles. Inverse Compton emission is thought to occur in many astrophysical contexts including gamma-ray bursts, extragalactic jets and lobes, intra-cluster gas, and so on. Much of the following (except for section 2.4.5, which is my own development) is based on lecture notes[2] prepared by Geoff Bicknell, which provide more detailed explanations and derivations of the following results. Some useful references regarding inverse Compton emission include Rybicki & Lightman (1979); Blumenthal & Gould (1970); Coppi & Blandford (1990). For the case of inverse Compton scattering of an anisotropic radiation field see eg. Reynolds (1982); Dermer & Schlickeiser (1993); Brunetti (2000); Brunetti et al. (2002)

2.4.1 Single Scattering Event

When considering the collision between a photon and particle, the conservation of 4-momentum gives an expression describing the change in photon energy for a given scattering angle in the rest frame of the particle.

$$\epsilon_s = \frac{\epsilon_i}{1 + \frac{\epsilon_i}{m_e c^2}(1 - \cos\Theta)} \tag{2.51}$$

where ϵ_i and ϵ_s are the energies of the incident and scattered photons respectively, and Θ is the scattering angle. For a single scattering event in the rest frame of the particle, the probability distribution for the scattering angle is given by the differential scattering cross-section

$$\frac{d\sigma}{d\Omega} = \frac{r_e^2}{2}\frac{\epsilon_s^2}{\epsilon_i^2}\left(\frac{\epsilon_s}{\epsilon_i} + \frac{\epsilon_i}{\epsilon_s} - \sin^2\Theta\right) \quad \text{(Klein-Nishina cross-section)} \tag{2.52}$$

$$\approx \frac{r_e^2}{2}\left(1 + \cos^2\Theta\right) \quad \epsilon_i \ll m_e c^2 \quad \text{(Classical (Thompson) Limit)} \tag{2.53}$$

It can be seen from equation (2.51) that in the Thompson limit ($\epsilon_i << m_e c^2$), the photon energy is not altered by the collision. However, if the particle is moving relativistically towards the observer with Lorentz factor γ, the scattered photon energies are increased, on average, by a factor of $\epsilon_s/\epsilon_i \approx \gamma^2$. The increase of energy in the case of a relativistically moving particle is due to the fact that, in transforming from the lab frame to the particle rest frame, the incident photons

[2] http://www.mso.anu.edu.au/ geoff/HEA/HEA.html

are Doppler (blue) shifted by a factor $\gamma(1-\beta\cos\psi_i)$, where ψ_i is the angle between the particle velocity and incident photon direction observed in the lab frame. In addition, transforming the scattered photons from the electron rest frame to the lab frame results in a Doppler (blue) shift by a factor $\gamma(1+\beta\cos\psi'_s)$ where ψ'_s is the angle between the particle velocity and the scattered photon direction observed in the particle rest frame.

The maximum increase in photon energy occurs when the incident photon direction is anti-parallel to the particle velocity and the scattered photon direction is parallel to the velocity. In that case $\epsilon_s = 4\gamma^2\epsilon_i$, and this sets an upper limit to the scattered photon energy. Oblique collision angles ψ and scattering angles ψ' result in lower scattered frequencies ν, hence the distribution in luminosity density illustrated in figure 2.6.

2.4.2 Emission from a Single Particle

As with synchrotron emission, inverse Compton scattered radiation is strongly beamed in the direction of the particle's motion. The luminosity per unit frequency produced by a single particle with Lorentz factor γ scattering an isotropic, monochromatic radiation field of frequency ν_0 and photon number density $n_{\rm ph}$ is given by

$$L_\nu = h\,c\,\sigma_T\,n_{\rm ph}\,qF_C(q) \tag{2.54}$$

where

$$q = \frac{\nu}{4\gamma^2\nu_0} \qquad \left[\frac{1}{4\gamma^2} < q < 1\right] \tag{2.55}$$

$$F_C(q) = 2q\ln q + q + 1 - 2q^2 \tag{2.56}$$

This power spectrum is plotted in Figure 2.6. The mean frequency of scattered photons is

$$\langle\nu\rangle = \frac{4}{3}\gamma^2\nu_0 \tag{2.57}$$

The spectrum in Figure 2.6 is highly peaked around the frequency $\nu \approx 2.4\gamma^2\nu_0$. Let $q = \nu/4\gamma^2\nu_0$. 95% of the power comes from the range $0.13 < q < 1$, and 99% from the range $0.05 < q < 1$. However, the power emitted at a frequency ν is only dependent on the product $\nu_0\gamma^2$, not on γ or ν_0 individually. Therefore, if a broad range of incident photon frequencies is present along with a broad range of electron energies (for example when considering synchrotron self Compton scattering), a wide range of electron energies will contribute to the observed flux at a given frequency ν. On the other hand, if a narrow range of incident photon energies are present, for example when considering inverse Compton scattering of the cosmic microwave background, then only a narrow range of electron energies contribute to the observed flux.

The total inverse Compton luminosity (cooling rate) of a single particle in an isotropic radiation field of total energy density $U_{\rm rad}$ is

$$L_{IC} = -\frac{dE}{dt} = (4/3)\sigma_T c\gamma^2\beta^2 U_{\rm rad} \tag{2.58}$$

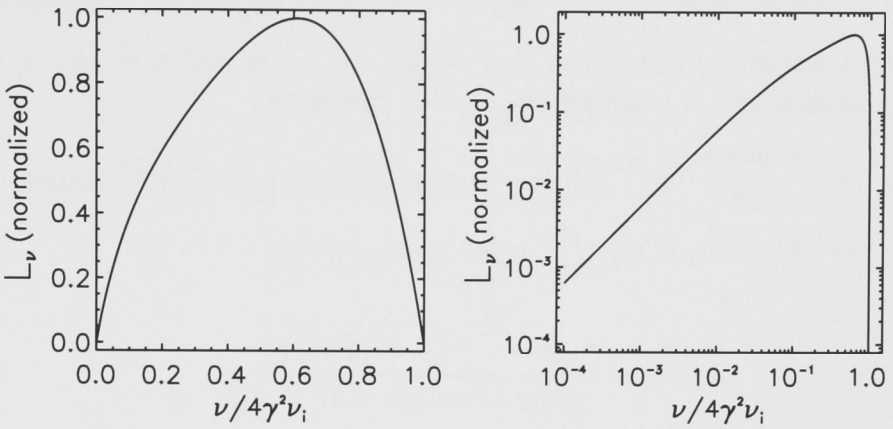

Figure 2.6: The inverse Compton power spectrum of a single electron with Lorentz factor γ scattering photons of frequency ν_0.

2.4.3 Emission Spectrum from a Distribution of Particles

Isotropic radiation field and particle distribution

The emissivity from an isotropic distribution of electrons with number density per unit Lorentz factor $N(\gamma)$ in an isotropic photon field with photon number density per unit frequency $n(\nu_0)$ is given by

$$j_\nu = \frac{3hc\sigma_T}{4\pi}\int_{\nu_{0_1}}^{\nu_{0_2}} n(\nu_0)\left[\int_{\gamma_1}^{\gamma_2} N(\gamma)\, qF_C(q)d\gamma\right] d\nu_0 \tag{2.59}$$

$$\tag{2.60}$$

This is a general expression, and is valid for any particle distribution and any photon distribution, provided they are both isotropic (Blumenthal & Gould, 1970). Now, changing the integration variable from γ to q, we obtain

$$j_\nu = \frac{3hc\sigma_T}{16\pi}\nu^{1/2}\int_{\nu_{0_1}}^{\nu_{0_2}} n(\nu_0)\,\nu_0^{-1/2}\left[\int_{q2}^{q1} N(\gamma)q^{-1/2}F_C(q)dq\right] d\nu_0 \tag{2.61}$$

$$q_1 = \mathrm{Min}\left[1, \frac{\nu}{4\gamma_1^2\nu_0}\right] \tag{2.62}$$

$$q_2 = \mathrm{Min}\left[1, \frac{\nu}{4\gamma_2^2\nu_0}\right] \tag{2.63}$$

Analytic Approximation for Power-law Electron Distribution

Let the number density per unit Lorentz factor be

$$N(\gamma) = K_e \gamma^{-a} \quad \text{for } \gamma_1 < \gamma < \gamma_2 \tag{2.64}$$

$$\text{then} \quad N(q(\gamma)) = K_e 2^a \left(\frac{\nu}{\nu_0}\right)^{-a/2} q^{a/2} \quad \text{for } \frac{\nu}{4\gamma_2^2\nu_0} < q < \frac{\nu}{4\gamma_1^2\nu_0} \tag{2.65}$$

For a given scattered frequency ν, if $q_2 = \frac{\nu}{4\gamma_2^2\nu_0} << 1 \; \forall \; \nu_0$ and $q_1 = \frac{\nu}{4\gamma_1^2\nu_0} \gtrsim 1 \; \forall \; \nu_0$ then the integral over q is a constant, and we can write

$$j_\nu = \frac{2^a 3hc\sigma_T}{16\pi} K_e \nu^{(1-a)/2} \int_{\nu_{0_1}}^{\nu_{0_2}} n(\nu_0)\, \nu_0^{(a-1)/2} d\nu_0 \left[\int_0^1 q^{(a-1)/2} F_C(q) dq\right] \tag{2.66}$$

$$= f_c(a) hc\sigma_T K_e \nu^{-\alpha} \int_{\nu_{0_1}}^{\nu_{0_2}} n(\nu_0)\, \nu_0^{\alpha} d\nu_0 \tag{2.67}$$

where

$$f_c(a) = \frac{3 \cdot 2^{a-2}}{\pi} \frac{(a^2 + 4a + 11)}{(a+1)(a+3)^2(a+5)} \tag{2.68}$$

It can be seen that the analytic inverse Compton spectrum is a power-law with spectral index $\alpha = (a-1)/2$, the same as the synchrotron spectrum. This analytic spectrum is accurate provided the frequency range of ambient photons is relatively narrow. If the ambient photon field is broad and the range of electron energies is relatively narrow, the inverse Compton spectrum will have the same spectral slope as the ambient radiation field. These features are discussed further below.

The above is relevant only to a situation in which the particle velocities and ambient radiation field are both isotropic.

2.4.4 Synchrotron Self Compton

Synchrotron self Compton (SSC) emission is the process in which relativistic particles inverse Compton scatter the locally generated synchrotron photons to produce higher energy photons.

Homogeneous, Spherical, Power-law SSC Model

Assuming a power-law electron energy distribution and using equation (2.67) we find

$$F_\nu = \frac{\delta^m (1+z)}{D_L^2} f_c(a) hc\sigma_T K_e \nu'^{-\alpha} \int_{\nu'_{0_1}}^{\nu'_{0_2}} \nu_0'^{\alpha} \left[\int n(\nu'_0)\, dV\right] d\nu'_0 \tag{2.69}$$

$$= \frac{\delta^{m+\alpha} (1+z)^{1-\alpha}}{D_L^2} f_c(a) hc\sigma_T K_e \nu^{-\alpha} \int_{\nu'_{0_1}}^{\nu'_{0_2}} \nu_0'^{\alpha} \left[\int n(\nu'_0)\, dV\right] d\nu'_0 \tag{2.70}$$

where m=2 for a jet and m=3 for a blob (as per §2.2). In order to calculate the volume integral, we assume a spherical source. Note that even for a spherical

source, the radiation field at any point except the centre of the sphere will have an anisotropic radiation field. While this is true, the spherical symmetry of the model means that the effects of anisotropic radiation field are cancelled, so that the emission is indeed isotropic, and equal to the emission calculated assuming an isotropic radiation field is present at each point of the sphere. The volume integral of photon number density is related to the integral of the radiation energy density via

$$\int n(\nu_0')dV = \frac{1}{h\nu_0'}\int u'(\nu_0')dV$$

For a spherical blob of homogeneous plasma, we have

$$\begin{aligned}\int u'(\nu_0')dV &= \frac{3}{4}u'_{R=0}(\nu_0')V \\ u'_{R=0}(\nu_0') &= \frac{2\pi}{c}I'_{\nu_0'} \\ &= \frac{2\pi}{c}2Rj'_{\nu_0'}\end{aligned}$$

So now,

$$\int n(\nu_0')dV = \frac{3\pi RV}{h\nu_0'c}j'_{\nu_0'} \tag{2.71}$$

Hence,

$$F_\nu = \frac{\delta^{m+\alpha}(1+z)^{1-\alpha}}{D_L^2}f_c(a)\sigma_T K_e\nu^{-\alpha}3\pi RV\int_{\nu'_{0_1}}^{\nu'_{0_2}}\nu_0'^{\alpha-1}j'_{\nu_0'}d\nu_0' \tag{2.72}$$

$$= \frac{\delta^{m+\alpha}(1+z)^{1-\alpha}}{D_L^2}f_c(a)\sigma_T K_e\nu^{-\alpha}3\pi RV\nu'^{\alpha}_{obs}j'_{\nu'_{obs}}\ln\left(\frac{\nu_{0_2}}{\nu_{0_1}}\right) \tag{2.73}$$

$$= f_c(a)\sigma_T K_e\nu^{-\alpha}3\pi R\nu^{\alpha}_{obs}F_{\nu_{obs}}\ln\left(\frac{\nu_{0_2}}{\nu_{0_1}}\right) \tag{2.74}$$

where $F_{\nu_{obs}}$ is the observed synchrotron flux density at an arbitrary observing frequency ν_{obs}, and equation (2.10) has been used to relate the observed synchrotron flux density to rest frame emissivity.

2.4.5 Comparison of Analytic and Numerical SSC Spectrum

There is a common misconception that the SSC spectrum will precisely match the analytic power-law approximation over some range of frequencies. For example, the NRAO Essential Radio Astronomy course website[3] states that "[The spectrum of monoenergetic electrons inverse Compton scattering a monochromatic radiation field] is more peaked than the synchrotron spectrum of monoenergetic electrons.

[3]NRAO Essential Radio Astronomy Course Website available at `http://www.cv.nrao.edu/course/astr534/InverseCompton.html`

Therefore we don't really need to use the detailed Compton scattering spectrum of monoenergetic electrons to calculate the inverse-Compton spectrum of an astrophysical source containing a power-law distribution of electrons. If the electron energy distribution is $N(E) = KE^{-\delta}$, the scattered spectrum will also be a power-law with spectral index $\alpha = (1 - \delta)/2$". Erlund et al. (2008) state "SSC emission has the same spectral shape as the synchrotron spectrum that has been upscattered." and Tavecchio et al. (2000b) write "Note that the X-ray spectrum also has the same spectral index as the radio spectrum, as expected in either EC or SSC models." These are just a few examples of incorrect or misleading statements in the literature regarding the shape of the SSC spectrum.

This section has been included to show the work I have done in analysing the power-law synchrotron self Compton model in order to test SSC modeling software that I have written, and to show in a clear way that the SSC spectrum is not simply a power law spectrum with the same slope as the synchrotron spectrum over a wide range of frequencies.

As shown above, in order that the SSC spectrum match the power-law model, the inner integral over q must be constant for all values of the ambient photon frequency. In order that the integral over q be constant for all values of the ambient photon frequency, there are two requirements:

$$q_2 = \frac{\nu}{4\gamma_2^2\nu_0} << 1 \; \forall \; \nu_0 \tag{2.75}$$

$$\text{and} \quad q_1 = \frac{\nu}{4\gamma_1^2\nu_0} \gtrsim 1 \; \forall \; \nu_0 \tag{2.76}$$

These two conditions imply that

$$\frac{\nu}{4\gamma_2^2\nu_{0_1}} \lesssim \epsilon \tag{2.77}$$

$$\text{and} \quad \frac{\nu}{4\gamma_1^2\nu_{0_2}} \gtrsim 1 \tag{2.78}$$

where ν_{0_1} and ν_{0_2} are the minimum and maximum frequencies of the ambient photon field and I have made the substitution $q_2 << 1 \iff q_2 \lesssim \epsilon$ and ϵ is a sufficiently small number below which the contribution to the integral over q is negligible. The value of ϵ depends on the spectral index, and for $a = 2$, $\epsilon \sim 0.02$. Let us first consider a scenario in which a broad range of electron energies are present, but only a narrow range of ambient photon frequencies, so that $\nu_{0_1} \approx \nu_{0_2}$. In that case, the above requirements will be satisfied (and hence the scattered spectrum will be a power-law) for frequencies in the range $4\gamma_1^2\nu_0 \lesssim \nu \lesssim \epsilon \times 4\gamma_2^2\nu_0$.

Let us now consider the case of synchrotron self Compton emission. In that case, $\nu_{0_1} \approx \Omega_0\gamma_1^2/\pi$ and $\nu_{0_2} \approx \Omega_0\gamma_2^2/\pi$. Hence, the requirements for the power-law spectrum are:

$$\nu << 4\gamma_2^2\gamma_1^2\frac{\Omega_0}{\pi} \tag{2.79}$$

$$\text{and} \quad \nu \gtrsim 4\gamma_1^2\gamma_2^2\frac{\Omega_0}{\pi} \tag{2.80}$$

Clearly these two requirements cannot be satisfied simultaneously. The SSC spectrum will be closest to the analytic power-law spectrum at some frequency in the range $\epsilon \times 4(\gamma_1\gamma_2)^2\Omega_0/\pi < \nu < 4(\gamma_1\gamma_2)^2\Omega_0/\pi$, and at that point, the SSC spectral index will match the power-law. Above and below that frequency, the spectrum will curve away from the power-law, as shown in Figure 2.7(a). This occurs because there is a significant contribution to the emissivity from a wide range of particle energies, which in turn is due to the broad range of ambient photon frequencies present. Figure 2.7 illustrates the reasons why the SSC spectrum curves away from the power-law approximation. At frequency $\nu_b \sim (\gamma_1\gamma_2)^2\Omega_0$ the SSC spectrum meets the power-law approximation. At this frequency there is a significant contribution to the emissivity from all particle energies. At ν_a there is a reduced contribution to the emissivity from high energy particles scattering high energy photons. At ν_c, the low energy particles cannot scatter the low frequency photons to ν_c because of the condition $\nu < 4\gamma^2\nu_0$. It is interesting to note that the maximum contribution to the emissivity comes from the lowest energy particles.

The low and high energy cutoffs in the SSC spectrum are, respectively

$$\nu_{\min} = 4\gamma_1^2\nu_{0_1} \approx \gamma_1^4\Omega_0 \tag{2.81}$$

$$\nu_{\max} = 4\gamma_2^2\nu_{0_2} \approx \gamma_2^4\Omega_0 \tag{2.82}$$

The upper cutoff is a true cutoff in the sense that no photons can be produced above this frequency. The lower cutoff is simply a low energy turnover.

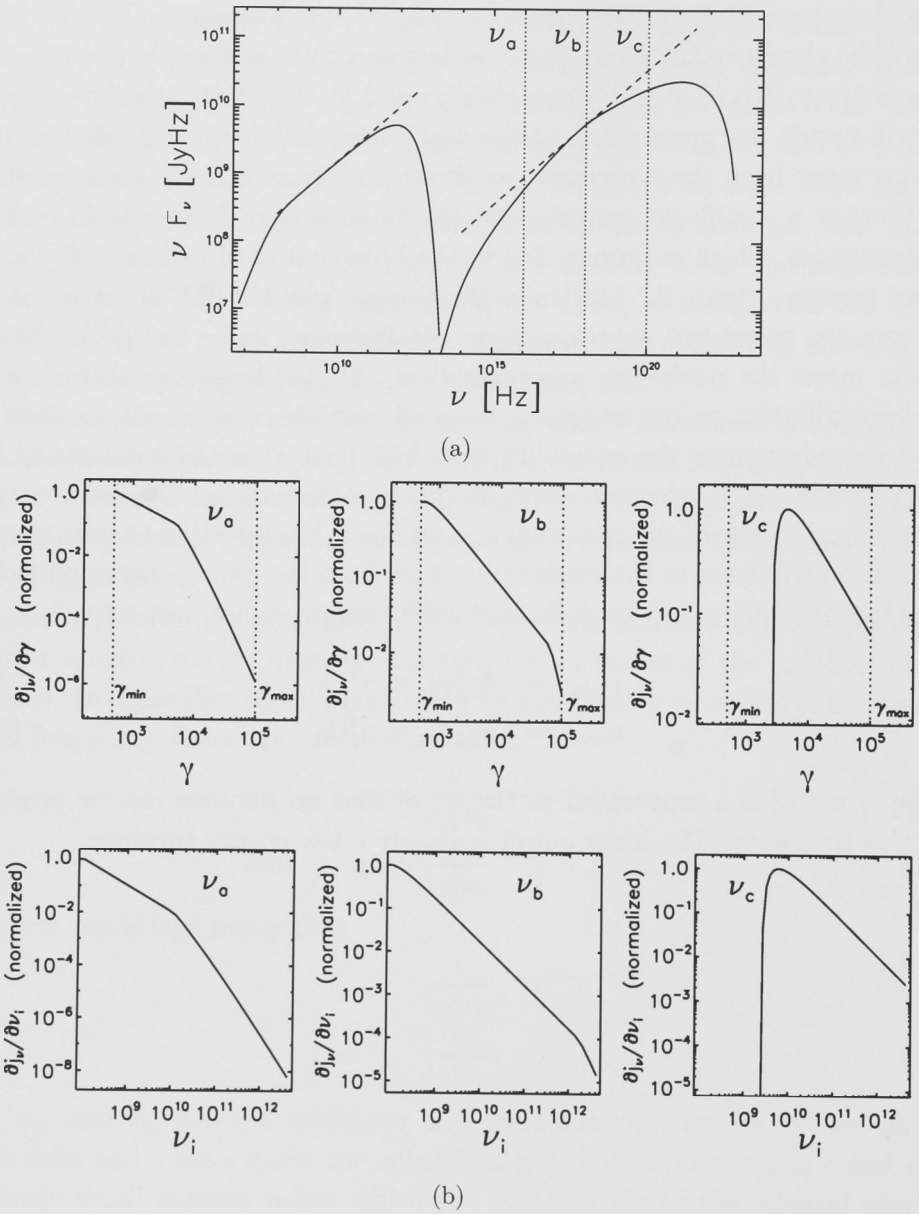

Figure 2.7: (a) Example synchrotron plus SSC spectral energy distribution produced by a power law spectrum of relativistic electrons. (b) Plots of the SSC emissivity density at fixed observing frequencies ν_a, ν_b and ν_c which correspond to the vertical lines marked in Figure (a) above. These plots illustrate the reasons for the curvature in the SSC spectrum. At $\nu_b \approx \gamma_1^2\gamma_2^2\Omega_0/\pi$, where the SSC spectrum meets the power law approximation, there is a significant contribution to the SSC emissivity from all electrons and all soft photons. At ν_a, there is a decrease in the contribution to the emissivity from the highest energy electrons as well as the highest energy photons. At ν_c, the emissivity density is cutoff at low electron energies and low soft photon frequencies due to the constraint $q < 1$. Hence, the SSC spectrum curves away from the analytic power law approximation at frequencies above and below ν_b.

2.5 Synchrotron Self Compton Modeling of Hotspot Spectra

Synchrotron emission from radio galaxies, supernovae remnants and gamma ray bursts often exhibit power law radio spectra (i.e. $F(\nu) \propto \nu^{-\alpha}$). This implies that the underlying particle distribution is also a power law, having a spectrum of the form $N(\gamma) = K_e \gamma^{-a}$ where $a = 2\alpha + 1$ (Rybicki & Lightman, 1979). Such power law spectra are naturally produced via First order Fermi acceleration at a shock (see eg. Kirk & Duffy, 1999; Drury, 2004, for a review of shock acceleration). In a number of hotspots, the radio spectrum breaks from a spectral index of $\alpha \sim 0.5$ to $\alpha \gtrsim 1.0$ (Meisenheimer et al., 1989, 1997; Brunetti et al., 2003; Cheung et al., 2005). This broken power law arises because emission is integrated over an area in which synchrotron cooling is important for the higher energy electrons, but does not affect the lower energy electrons. The production of a broken power law particle distribution downstream of a shock is discussed in the following section.

2.5.1 Volume Averaged Electron Energy Distribution Arising from a Shock

Consider a simple model in which plasma enters a shock at x=0, at which point a power-law electron energy distribution (EED) of the form $N(\gamma) = N_0 \gamma^{-a}$ for $\gamma_1 < \gamma < \infty$ is injected into the flow. The power-law EED is advected downstream with the post-shock flow and is affected by synchrotron and inverse Compton cooling. Neglecting diffusion, the evolution of the momentum space distribution function $f(p,t)$ is governed by the equation:

$$\frac{\partial f(p,t)}{\partial t} - \frac{1}{3}\mathrm{div}\mathbf{v}p\frac{\partial f(p,t)}{\partial p} - \frac{1}{p^2}\frac{\partial}{\partial p}\left(\frac{A}{m_e c}p^4 f(p,t)\right) = 0 \tag{2.83}$$

where

$$A = \frac{4}{3}\frac{\sigma_T \beta^2 (U_B + U_{\mathrm{rad}})}{m_e c} \tag{2.84}$$

U_B is the magnetic energy density, U_{rad} is the energy density of the ambient radiation field, and the electron number density per unit Lorentz factor is related to the momentum space distribution via

$$N(\gamma) = 4\pi m_e c p^2 f(p,t) \tag{2.85}$$

The EED is affected by energy dependent synchrotron and inverse Compton cooling such that at a point $x = x(t)$ downstream of the shock, the EED is

$$N(\gamma) = N_0 \gamma^{-a}\left[1 - \frac{\gamma}{\gamma_2(t)}\right]^{a-2} \quad \gamma > \gamma_1 \tag{2.86}$$

where the cutoff Lorentz factor $\gamma_2(t)$ at position $x = x(t)$ is

$$\gamma_2(t) = [At]^{-1} \tag{2.87}$$

Assuming a constant velocity, v, downstream of the shock, $\gamma_2(t) = v/[A\,x(t)]$. Let L be the length of the region being considered. The average number density per unit Lorentz factor in the range $0 < x < L$ is

$$\bar{N}(\gamma) = \begin{cases} 0 & \gamma < \gamma_{\rm min}, \quad \gamma > \gamma_{\rm max} \\ \frac{K_e \gamma_b}{(a-1)} \gamma^{-(a+1)} g\left(\frac{\gamma}{\gamma_b}\right) & \gamma_{\rm min} < \gamma < \gamma_{\rm max} \end{cases} \tag{2.88}$$

where

$$g\left(\frac{\gamma}{\gamma_b}\right) = \begin{cases} 1 - \left(1 - \frac{\gamma}{\gamma_b}\right)^{a-1} & \gamma < \gamma_b \\ 1 & \gamma > \gamma_b \end{cases} \tag{2.89}$$

The above distribution is a broken power-law spectrum with the electron spectral index smoothly changing from -a to -(a+1) at $\gamma \approx \gamma_b$. The break in the electron spectrum at γ_b corresponds to the electron energy at which the synchrotron cooling half-life is equal to the time taken for electrons to travel the distance L.

$$\gamma_b = \frac{v}{AL} = \frac{3 m_e c^2 \beta_f}{4 L \sigma_T \left(U_B + U_{\rm rad}\right)} \tag{2.90}$$

where β_f is the plasma flow velocity behind the shock in units of c. The idea of a broken power-law describing emission from a region containing a shock was first presented by Heavens & Meisenheimer (1987), and has had some success in fitting the radio spectra of a number of hotspots (Meisenheimer et al., 1989, 1997). However, not all hotspot spectra exhibit a synchrotron cooling break (Meisenheimer et al., 1997).

2.5.2 The Emission Spectrum from a Shock

Using the volume averaged shock distribution function $\bar{N}(\gamma(y))$ defined by equations (2.88) and (2.89) the angle averaged emission spectrum is

$$\langle F_\nu \rangle = \frac{\delta^{(a+3)/2} (1+z)^{(3-a)/2} V}{D_L^2} A(a) \nu^{-a/2} \nu_b^{1/2} A_{\rm syn} \int_{\nu/\nu_2}^{\nu/\nu_1} y^{\frac{a-2}{2}} \bar{F}(y)\, g\left(y, \frac{\nu}{\nu_b}\right) dy \tag{2.91}$$

where

$$g\left(y, \frac{\nu}{\nu_b}\right) = \begin{cases} 1 - \left[1 - \left(\frac{\nu}{y \nu_b}\right)^{1/2}\right]^{a-1} & y > \frac{\nu}{\nu_b} \\ 1 & y < \frac{\nu}{\nu_b} \end{cases} \tag{2.92}$$

$$\nu_{1,b,2} = \frac{\delta}{(1+z)} \frac{3}{4\pi} \Omega_0 \gamma^2_{\rm min,b,max} \tag{2.93}$$

$$A_{\rm syn} = K_e \Omega_0^{\frac{a+1}{2}} \tag{2.94}$$

$$A(a) = \frac{r_e m_e c\, 3^{a/2}}{(a-1)\, 2^{a+2}\, \pi^{\frac{a+1}{2}}} \tag{2.95}$$

The shape of the model synchrotron spectrum is determined by the parameters ν_1, ν_b, ν_2 and a. The amplitude is governed by the parameter $A_{\rm syn}$. The parameters ν_1, ν_b and ν_2 correspond to the characteristic frequency emitted by electrons with Lorentz factor $\gamma_{\rm min}$, γ_b and $\gamma_{\rm max}$ in a magnetic field of flux density B, and are therefore identified with the low frequency turn-over, synchrotron cooling break and high frequency cutoff respectively. In equation (2.91) we have assumed the emission is produced by plasma flowing at a relativistic speed βc at an angle θ to the line of sight with corresponding Lorentz factor $\Gamma = (1-\beta^2)^{-1/2}$ and Doppler factor $\delta = [\Gamma(1-\beta\cos\theta)]^{-1}$ through a stationary volume or pattern, so that $F_\nu \propto \delta^{(a+3)/2}$ as appropriate for extragalactic jets (Lind & Blandford, 1985). If the volume in which the flux is produced is moving relativistically, an extra factor of δ enters, so that the leading factor of $\delta^{(a+3)/2}$ in equation (2.91) becomes $\delta^{(a+5)/2}$.

The synchrotron self Compton flux density is given by

$$F_\nu^{\rm ssc} = \left(\frac{9\cdot 2^{(a-3)} R\,\sigma_T}{a-1}\right)\nu^{-a/2} A_{\rm ssc}\int_{\nu_1}^{\nu_2}\nu_i^{(a-2)/2}F_{\nu_i}^{\rm syn}\left[\int_{q_2}^{q_1} q^{a/2}F_C(q)g\left(\frac{q_b}{q}\right)dq\right]d\nu_i \tag{2.96}$$

where

$$\begin{aligned} A_{\rm ssc} &= K_e\gamma_b \\ q_b &= \frac{\epsilon_s}{4\epsilon_i\gamma_b^2} \end{aligned} \tag{2.97}$$

$$g\left(\frac{q_b}{q}\right) = \begin{cases} 1-\left(1-\left(\frac{q_b}{q}\right)^{1/2}\right)^{a-1} & q > q_b \\ 1 & q < q_b \end{cases} \tag{2.98}$$

and $F_{\nu_i}^{\rm syn}$ is calculated using equation (2.91). In equation (2.96) we have assumed

$$\int n(\nu_i')dV' = \frac{3\pi}{h\nu_i' c}Rj_{\nu_i'}^{\prime\,\rm syn}V' \tag{2.99}$$

$$= \frac{3\pi R}{h\nu_i c}\frac{F_{\nu_i}^{\rm syn}D_L^2}{\delta(1+z)} \tag{2.100}$$

as appropriate for a spherical region of homogenous plasma. In the above expression ν_i' is the incident photon frequency in the rest frame of the plasma, and $j_{\nu_i}^{\rm syn}$ is the synchrotron emissivity at frequency ν_i' in the rest frame of the plasma.

In chapter 3, modeling of the hotspot spectrum is performed using the above expressions for synchrotron and self Compton emission. The advantage of this formulation is that it allows the model to be specified in terms of the observed values of ν_1, ν_b and ν_2, while the parameters $A_{\rm syn}$ and $A_{\rm ssc}$ are normalization factors for the synchrotron and SSC spectral components respectively.

2.6 Modeling the Spectral Energy Distribution of Jet Knots

2.6.1 Inverse Compton Scattering of the CMB (IC/CMB)

The one-zone IC/CMB model assumes a jet of plasma with bulk Lorentz factor Γ makes an angle to the line of sight θ and carries a relativistic electron/positron population with number density per unit Lorentz factor given by $N(\gamma) = K_e\gamma^{-a}$ for $\gamma_1 < \gamma < \gamma_2$.

Dermer (1995) gives an expression for the Inverse Compton flux density produced by a jet with Lorentz factor Γ and angle to the line of sight θ in an isotropic, monochromatic radiation field of energy density $u^*_{\rm iso}$ and photon energy ϵ^*:

$$F^{\rm IC}_{\epsilon_{\rm obs}} = \delta^{4+2\alpha}\frac{c\sigma_T u^*_{\rm iso}K_eV}{8\pi D_L^2\epsilon^*}(1+z)^{1-\alpha}\left(\frac{1+\mu_{\rm obs}}{1+\beta_{\rm jet}}\right)^{1+\alpha}\left(\frac{\epsilon_{\rm obs}}{\epsilon^*}\right)^{-\alpha} \tag{2.101}$$

where $\mu_{\rm obs} = \cos\theta_{\rm obs}$ is the cosine of the angle between the beaming direction and the line of sight to the observer.

Dermer (1995) compares this expression for inverse Compton flux density with a similar expression for the synchrotron flux density derived using a δ-function approximation for the synchrotron photon energy

$$F^{\rm syn}_{\epsilon_{\rm obs}} = \delta^{3+\alpha}\frac{c\sigma_T U_B K_eV}{6\pi D_L^2\epsilon_B}(1+z)^{1-\alpha}\left(\frac{\epsilon_{\rm obs}}{\epsilon_B}\right)^{-\alpha} \tag{2.102}$$

where $U_B = B^2/8\pi$ is the energy density of the magnetic field in the jet frame, and $\epsilon_B = B/4.414\times10^{13}G$. In each of these expressions, it has been assumed that emission is from a moving blob. In the case of emission from a continuous jet, one factor of δ must be dropped from each expression. Taking the ratio of these two expressions gives an expression for the Doppler factor in terms of the magnetic field strength in the jet and the ratio of inverse Compton to synchrotron flux densities. Let $B^{\delta=1}_{\rm eq}$ be the equipartition magnetic field strength calculated under the assumption $\delta = 1$. The Doppler factor is calculated assuming equipartition in the jet following Dermer (1995) and Harris & Krawczynski (2002)

$$\delta_{\rm jet} = \left[B^{\delta=1}_{eq}\left(\left(\frac{F_{ic}\nu^\alpha_{ic}}{F_{syn}\nu^\alpha_{syn}}\right)a_1a_2^{1-\alpha}(1+z)^{-(3+\alpha)}\right)^{\frac{1}{\alpha+1}}\right]^{\frac{3+\alpha}{5+2\alpha}} \tag{2.103}$$

$$\delta_{\rm blob} = \left[B^{\delta=1}_{eq}\left(\left(\frac{F_{ic}\nu^\alpha_{ic}}{F_{syn}\nu^\alpha_{syn}}\right)a_1a_2^{1-\alpha}(1+z)^{-(3+\alpha)}\right)^{\frac{1}{\alpha+1}}\right]^{\frac{1}{2}} \tag{2.104}$$

where a_1 and a_2 are constants. Dermer (1995) and Harris & Krawczynski (2002) give slightly different values for these constants, with $(a_1, a_2) = (1.326\times10^{11}\mathrm{G}^{-2}, 5.713\times$

10^4 G) and $(a_1, a_2) = (9.947 \times 10^{10}\,\mathrm{G}^{-2}, 3.808 \times 10^4$ G) for Dermer (1995) and Harris & Krawczynski (2002) respectively. The different values for these constants do not introduce significant errors in the model parameters relative to the other sources of error. In this analysis I use the values for a_1 and a_2 given by Harris & Krawczynski (2002), in order to be consistent with recent studies in this area (eg. Marshall et al., 2005). The different beaming patterns produced by a continuous jet and a moving blob result in a different dependence of Doppler factor on the observables. The subscript "jet" refers to a model that assumes the source is a stationary pattern in a continuous jet (for which $F_\nu^{\mathrm{syn}} \propto \delta^{2+\alpha}$) while the subscript "blob" refers to a model in which the source is assumed to be a discrete moving source (for which $F_\nu^{\mathrm{syn}} \propto \delta^{3+\alpha}$). The differences in beaming pattern for different source geometries was discussed in §2.2. The magnetic field for each model is calculated as

$$B_{\mathrm{jet}} = B_{eq}^{\delta=1}\delta_{\mathrm{jet}}^{-\frac{2+\alpha}{3+\alpha}} \tag{2.105}$$

$$B_{\mathrm{blob}} = B_{eq}^{\delta=1}\delta_{\mathrm{blob}}^{-1} \tag{2.106}$$

and the electron density as

$$n_e = \frac{(a-1)}{(a-2)} \frac{\left[\frac{B}{\mathrm{Tesla}}\right]^2}{2\mu_0(1+C_E)m_e c^2} \gamma_{\mathrm{min}}^{-1} \quad \mathrm{m}^{-3} \tag{2.107}$$

$$\tag{2.108}$$

Chapter 3

A Multi-Wavelength Study of the High Surface Brightness Hotspot in PKS 1421–490

3.1 Introduction

PKS 1421–490 was first reported as a bright, flat spectrum radio source by Ekers (1969). Subsequent VLBI imaging revealed 10mas scale structure within the brightest component of this source (Preston et al., 1989). Studies at the Australia Telescope Compact Array (ATCA) later revealed significant radio emission on arcsecond scales extending south-west from the brightest component (Lovell, 1997). For this reason, PKS 1421–490 was included in a *Chandra* survey of flat spectrum radio quasars with arcsecond scale radio jets (Marshall et al., 2005). Gelbord et al. (2005) (from here on G05) reported on recent X-ray (*Chandra*), optical (Magellan) and radio (ATCA) imaging of this source. We refer the reader to that paper for the details of these observations and images.

Figure 3.1 illustrates the arcsecond scale radio structure of PKS 1421–490; it is annotated to show the naming convention for different components in the radio image used by G05, as well as the correct interpretation of each of these components brought out in this study. G05 obtained an optical spectrum of region B, and suggested it was not associated with an active galactic nucleus (AGN) in view of the apparent lack of spectral lines (due to poor signal to noise ratio in that spectrum). Region A was known to contain bright VLBI scale radio structure (Preston et al., 1989) and had a flat radio spectrum ($\alpha < 0.5$). Region B was also known to be much weaker than region A at radio wavelengths. Consequently region A was thought to be an AGN, while region B was (erroneously) interpreted by G05 as a jet knot. In this chapter we show that in fact region B *is* the active galactic nucleus (see §3.3), and that region A contains a high surface brightness hotspot. The main focus of this chapter is the interpretation and modeling of the exceptional hotspot in region A which has until now been interpreted as an AGN.

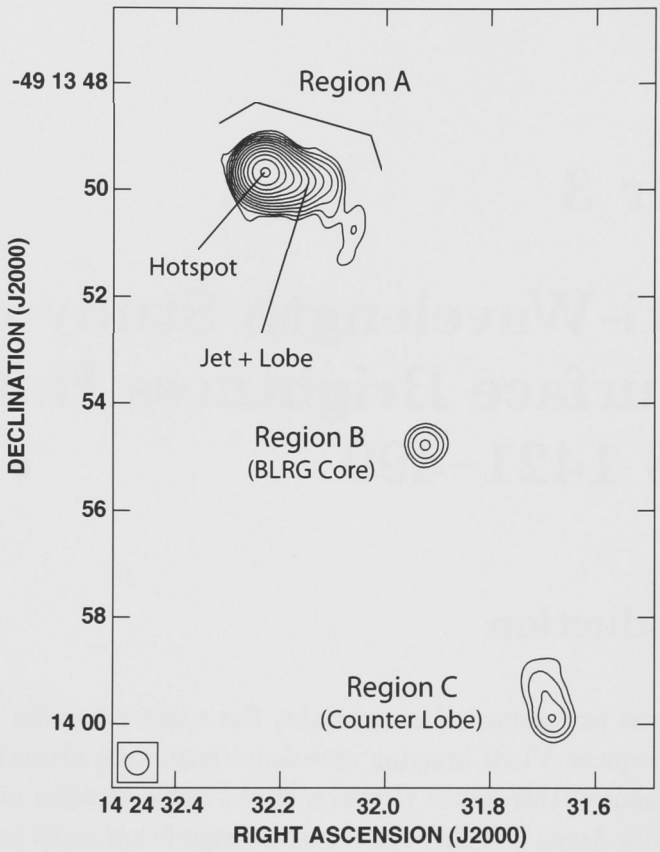

Figure 3.1: ATCA 20.2GHz image of PKS 1421–490 with source components labeled. This image was first presented in G05. To avoid confusion, the naming convention used by G05 is also included. Contour levels: 1.5 mJy/beam × (1, 2, 4, 8, 16, 32, 64, 128, 256, 512, 1024). Peak surface brightness: 2.11Jy/beam. Beam FWHM: 0.54 × 0.36 arcsec. The scale of the image is 7.0 kpc/arcsecond.

One of the major results of this chapter relates to an observed low frequency flattening in the hotspot radio spectrum at GHz frequencies, which indicates that the underlying electron energy distribution flattens towards lower energies. The low energy electron distribution is not only important for calculating parameters such as the number density and energy density, it also provides important constraints on the particle acceleration mechanism. In this chapter I argue that measuring and understanding the low energy cutoff may also help to address more fundamental issues such as jet composition and speed. We now present a brief overview of the literature relating to the low energy electron distribution in jets and hotspots.

In a small number of objects, flattening of the hotspot radio spectra towards lower frequencies has been observed. In most cases, synchrotron self absorption and

free-free absorption can be ruled out, and the observed flattening is interpreted in terms of a turn-over in the electron energy distribution (Leahy et al., 1989; Carilli et al., 1988, 1991; Lazio et al., 2006). When modeling hotspot spectra, the turn-over in the electron energy distribution is usually approximated by setting the electron number density equal to zero below a cutoff Lorentz factor $\gamma_{\rm min}$. In each case where flattening of the hotspot radio spectrum has been directly observed, estimates of $\gamma_{\rm min}$ are of the order of several hundred: Cygnus A, $\gamma_{\rm min} \sim 300$ - 400 (Carilli et al., 1991; Lazio et al., 2006; Hardcastle, 2001); 3C295, $\gamma_{\rm min} \sim 800$ (Harris et al., 2000; Hardcastle, 2001); 3C123, $\gamma_{\rm min} \sim 1000$ (Hardcastle et al., 2001; Hardcastle, 2001); PKS 1421–490, $\gamma_{\rm min} \sim 650$ (this work).

Leahy et al. (1989) presented evidence for a low energy cutoff in two other hotspots; 3C268.1 and 3C68.1. In both these ojects, the hotspot radio spectra are significantly flatter between 150 MHz and 1.5GHz than they are above 1.5GHz, which suggests a similar value of $\gamma_{\rm min}$ to those listed above, provided the hotspot magnetic field strengths are similar. More recently Hardcastle (2001) reported on a possible detection of an optical inverse Compton hotspot in the quasar 3C196. By modeling the synchrotron self Compton emission and assuming a magnetic field strength close to the equipartition value, they inferred a cutoff Lorentz factor $\gamma_{\rm min} \sim 500$. All of the above listed $\gamma_{\rm min}$ estimates appear to be distributed around a value of $\gamma_{\rm min} \sim 600$. However, Blundell et al. (2006) and Erlund et al. (2008) have inferred the existence of a low energy cutoff at $\gamma_{\rm min} \gtrsim 10^4$ in the hotspots of the giant radio galaxy 6C 0905–3955. Their method of detecting the low energy cutoff is quite different to those described above, and is based on the interpretation of an absence of X-ray emission from the eastern hotspot and radio lobe in that source.

In §3.8 we show that a turn-over in the electron energy distribution at $\gamma_{\rm min} \sim 100 - 1000$ arises naturally from the dissipation of jet energy if the jet has a high proton fraction and a bulk Lorentz factor $\Gamma_{\rm jet} \gtrsim 5$. However, Stawarz et al. (2007) have suggested that the low frequency flattening in the radio spectrum of a Cygnus A hotspot is not related to the turn-over in electron energy distribution. Rather, they argue, it indicates a transition between two different acceleration mechanisms.

Electron energy distributions with a low energy cutoff have also been discussed in relation to pc-scale jets. The absence of significant Faraday depolarization in compact sources suggests that the number density of electrons with Lorentz factor $\gamma \gtrsim 100$ greatly exceeds that of lower energy particles (Wardle, 1977; Jones & Odell, 1977). Gopal-Krishna et al. (2004) have argued that some statistical trends in superluminal pc-scale jets may be understood in terms of effects arising from a low energy cutoff in the electron energy distribution. Tsang & Kirk (2007) have suggested that a low energy cutoff in the electron spectrum can alleviate several theoretical difficulties associated with the inverse Compton catastrophe in compact radio sources, including anomalously high brightness temperatures and the apparent lack of clustering of powerful sources at 10^{12} K. However, circular

polarization in the pc-scale jet of 3C279 requires a minimum Lorentz factor $\gamma_{\rm min} < 20$ (Wardle et al., 1998).

Observational constraints on the low energy electron distribution in extragalactic jets on kpc-scales are rare. A low energy cutoff in the electron energy distribution at $\gamma_{\rm min} \sim 20$ has been estimated for the jet of PKS 0637–752 (500 kpc from the nucleus) through modeling of the radio to X-ray spectral energy distribution in terms of inverse Compton scattering of the cosmic microwave background (Tavecchio et al., 2000b; Uchiyama et al., 2005).

This chapter is structured as follows: In §3.2 we discuss our observations and data reduction. In §3.3 we discuss the active galactic nucleus - in particular the optical spectrum and broad band spectral energy distribution. In §3.4 we present the VLBI image of the northern hotspot and derive plasma parameters by modeling the broad band spectral energy distribution. In §3.5 we independently estimate the hotspot plasma parameters by modeling the radio spectrum of the entire radio galaxy. In §3.6 we discuss the incompatibility of the observed spectrum with the standard continuous injection plus synchrotron cooling model for hotspots. In §3.7 we consider Doppler beaming as a possible cause of the high radio surface brightness and various other properties of the hotspot. In §3.8 we consider the dissipation of energy associated with a cold proton/electron jet and present an expression that relates the energy of the peak in the electron energy distribution to the jet bulk Lorentz factor. We then consider the implications of this expression in the case of the northern hotspot of PKS 1421–490 and other objects. In §3.9 we summarize our findings.

Throughout this chapter we assume cosmology $\Omega_\Lambda = 0.73, \Omega_M = 0.27, H_0 = 71\,{\rm km\,s^{-1}\,Mpc^{-1}}$, and we define the spectral index as $\alpha = -\frac{\log(F_1/F_2)}{\log(\nu_1/\nu_2)}$ so that the flux density $F_\nu \propto \nu^{-\alpha}$.

3.2 Observations and Data Reduction

3.2.1 Summary

We observed PKS 1421–490 with the Long Baseline Array (LBA) at 2.3 and 8.4 GHz and with the ATCA at 2.3, 4.8, 8.4 and 93.5 GHz. We have also made use of ATCA radio data (4.8, 8.6, 17.7 and 20.2 GHz) previously published in Gelbord et al. (2005) as well as archival 1.4 GHz ATCA data. We combined these data with previously published infra-red, optical and X-ray flux densities to construct radio to X-ray spectra for the northern hotspot and the core as well as an accurate radio spectrum of the entire radio galaxy. Table 3.1 lists the observation information and references for all data used in this study. Figure 3.2 presents the spectra and indicates the source of each data point. It should be noted that these observations are not all contemporaneous. However, the light crossing time for the hotspot is over 1000 light years (see §3.4.1). Therefore, variability on a time-scale of decades

is not possible unless the hotspot is ultra relativistic, with Doppler factor in the order of 100. Such a high Doppler factor is not plausible given the estimates of jet speeds in both pc and kpc-scale jets of radio galaxies and quasars.

In addition to these data, we obtained an optical spectrum of region B in order to confirm the classification of that region as an active galactic nucleus. The spectroscopic observations are described in §3.2.5.

As well as describing the observations and data reduction steps, this section includes a description of some non-standard procedures that were required to construct the hotspot radio spectrum. Specifically, non-standard procedures were required to determine the hotspot flux density from the 8.4GHz LBA data-set due to limited (u, v) coverage. These non-standard procedures are described in §3.2.2. Non-standard procedures were also used to obtain a lower limit to the hotspot flux density at 93.5GHz. This procedure is described in §3.2.4.

Table 3.1. Observation Information and Flux Densities

Flux Density of...	Instrument	Frequency	Date Observed	Configuration	Resolution [a]	Flux Density [Jy]	Reference
Entire Source	MOST	408 MHz	1968 - 1978	—	2′.8	13.1 ± 0.7	1
Entire Source	Parkes	468 MHz	1965 - 1969	—	54′	11.9 ± 0.1	2
Entire Source	Parkes	635 MHz	1965 - 1969	—	30′.5	10.9 ± 0.5	2
Entire Source	MOST	843 MHz	1990 - 1993	—	1′.1	9.9 ± 0.5	3
Entire Source	ATCA	1.38GHz	Feb 24 2000	6A[b]	2′.2 [c]	8.5 ±0.2	4
Entire Source	ATCA	2.28GHz	Mar 23 2006	6C[b]	3′[c]	7.15±0.15	4
Entire Source	ATCA	4.80GHz	May 19 2005	H168	3′.5 [c]	5.5±0.1	4
Entire Source	ATCA	8.425GHz	May 19 2005	H168	2′[c]	4.25±0.1	4
Entire Source	ATCA	8.64GHz	Feb 4 2002	6C[b]	47″[c]	4.1±0.1	4
Entire Source	ATCA	17.73GHz	May 9 2004	6C[b]	30″[c]	2.74±0.06	4
Entire Source	ATCA	20.16GHz	May 9 2004	6C[b]	26″[c]	2.54±0.05	4
Entire Source	ATCA	93.5GHz	Aug 21 2005	H214[b]	10″[c]	1.0±0.1	4
Northern Hotspot	LBA	2.28GHz	Mar 23 2006	Tidbinbilla, ATCA Mopra, Parkes Hobart, Ceduna	13.5 × 11.6 mas	4.3 ± 0.2	4
Northern Hotspot	LBA	8.425GHz	May 19 2005	Parkes, Mopra, ATCA	33 × 13 mas	$3.2\ ^{+0.2}_{-0.3}$	4
Northern Hotspot	ATCA	17.73GHz	May 9 2004	6C	0″.58 × 0″.43	< 2.3	4
Northern Hotspot	ATCA	20.16GHz	May 9 2004	6C	0″.51 × 0″.37	< 2.1	4
Northern Hotspot	ATCA	93.5GHz	Aug 21 2005	H214	10″[c]	$0.8 < F_{93.5\ \mathrm{GHz}} < 1.1$[d]	4
Northern Hotspot	2MASS	1.38×10^{14} Hz	1998 - 2001	—	∼4″	$< 3.7 \times 10^{-4}$	5
Northern Hotspot	2MASS	1.82×10^{14} Hz	1998 - 2001	—	∼4″	$< 2.7 \times 10^{-4}$	5
Northern Hotspot	2MASS	2.4×10^{14} Hz	1998 - 2001	—	∼4″	$< 2.1 \times 10^{-4}$	5
Northern Hotspot	Magellan	3.93×10^{14} Hz	Apr 26 2003	MagIC	∼0″.6	$(3.9 \pm 0.8) \times 10^{-6}$	5
Northern Hotspot	Magellan	4.82×10^{14} Hz	Apr 26 2003	MagIC	∼0″.6	$(3.0 \pm 0.9) \times 10^{-6}$	5
Northern Hotspot	Magellan	6.29×10^{14} Hz	Apr 26 2003	MagIC	∼0″.6	$(1.9 \pm 0.8) \times 10^{-6}$	5
Northern Hotspot	Chandra	2.41×10^{17} Hz	Jan 16 2004	ACIS-S	0″.5	$(1.3 \pm 0.16) \times 10^{-8}$	5
Core	ATCA	4.8GHz	Feb 4 2002	6C		$< 7 \times 10^{-3}$	5
Core	ATCA	8.64GHz	Feb 4 2002	6C		$(9.6 \pm 0.6) \times 10^{-3}$	5
Core	ATCA	17.73GHz	May 9 2004	6C		$(9.8 \pm 0.3) \times 10^{-3}$	5
Core	ATCA	20.16GHz	May 9 2004	6C		$(9.2 \pm 0.2) \times 10^{-3}$	5
Core	2MASS	1.38×10^{14} Hz	1998 - 2001	—	∼4″	$(1.00 \pm 0.07) \times 10^{-3}$	5
Core	2MASS	1.82×10^{14} Hz	1998 - 2001	—	∼4″	$(8.8 \pm 0.6) \times 10^{-4}$	5
Core	2MASS	2.4×10^{14} Hz	1998 - 2001	—	∼4″	$(9.1 \pm 0.7) \times 10^{-4}$	5
Core	Magellan	3.93×10^{14} Hz	Apr 26 2003	MagIC	∼0″.6	$(8 \pm 1) \times 10^{-4}$	5

Table 3.1 (cont'd)

Flux Density of...	Instrument	Frequency	Date Observed	Configuration	Resolution [a]	Flux Density [Jy]	Reference
Core	Magellan	4.82×10^{14} Hz	Apr 26 2003	MagIC	$\sim 0\farcs6$	$(8 \pm 1.5) \times 10^{-4}$	5
Core	Magellan	6.29×10^{14} Hz	Apr 26 2003	MagIC	$\sim 0\farcs6$	$(7 \pm 2) \times 10^{-4}$	5
Core	Chandra	2.41×10^{17} Hz	Jan 16 2004	ACIS-S	$0\farcs5$	$(4.9 \pm 0.3) \times 10^{-8}$	5

Note. — The uncertainties in ATCA flux density are dominated by the uncertainty in the absolute flux calibration, which is estimated to be 2% (Reynolds, 1994), except for 93.5 GHz, where the uncertainty is estimated to be 10%. The lower limit on the hotspot flux at 93.5GHz comes from making an assumption about the non-hotspot spectrum extrapolated to higher frequencies from 8.4 GHz. See section 3.2.4 for details. References: (1) Large et al. (1981), (2) Wills (1975), (3) Campbell-Wilson & Hunstead (1994), (4) This work, (5) Gelbord et al. (2005).

[a]Convert to linear resolution using 7.0 kpc/arcsecond

[b]Only short baselines on which the radio galaxy is unresolved were used to measure the flux density.

[c]Resolution of shortest baseline.

[d]See section 3.2.4.

3.2.2 VLBI

LBA Observations at 2.3GHz

PKS 1421–490 was observed with 6 elements (ATCA, Mopra, Parkes, Tidbinbilla 70m, Hobart and Ceduna) of the Australian Long Baseline Array (LBA) on March 23 2006. A full 12 hour synthesis was obtained, recording a single 16 MHz bandwidth in both left and right hand circular polarization. Regular scans on a nearby phase calibrator, PKS 1424–418, were scheduled throughout the observation, as well as scans on a point like source, PKS 1519–273 (Linfield et al., 1989), used for gain calibration. Unfortunately, due to hardware issues, we were only able to process right hand circular polarization. However, this will not affect our results as we do not expect the hotspot emission to be significantly circularly polarized. Circular polarization in AGN seldom exceeds a few tenths of 1% (Rayner et al., 2000). Data were recorded to VHS tapes using the S2 system and correlated using the LBA hardware correlator with 32 channels and 2 second integration time. The data were correlated twice: once with the phase tracking centre located at the position of the radio peak in region A, and once with the phase tracking centre located ~ 5 arcseconds away, at the position of the core (region B).

The initial calibration of the visibility amplitudes was performed in AIPS, using the measured system temperatures and antenna gains. We obtained simultaneous ATCA data during our observation, and this allowed us to bootstrap the LBA flux scale to the ATCA flux scale by comparing simultaneous measurements of the point like source PKS 1519–273. After scaling the gains using this bootstrapping method, and correcting the residual delays and rates via fringe fitting, the data-set from the phase reference source was exported to DIFMAP (Shepherd, 1997) where it was edited and imaged. Amplitude and phase self calibration corrections obtained from imaging the phase reference source were imported into AIPS using the *cordump*[1] patch kindly supplied to us by Emil Lenc. These phase and amplitude corrections were then applied to PKS 1421–490, and the data exported to DIFMAP for deconvolution and self calibration. The resulting image is shown in figure 3.3. We measure a hotspot flux density of 4.3 ± 0.2 Jy at 2.3 GHz. Preston et al. (1989) obtained a flux density of 4.1 Jy at 2.3 GHz for the northern hotspot by model fitting SHEVE (Southern Hemisphere VLBI Experiment) data with the simplest model consistent with the data (two circular Gaussians).

We attempted to detect compact structure within region B (the core) using the data-set that had been correlated with the phase centre at that position. The time-averaging- and bandwidth-smeared emission from region A in this dataset was first cleaned to remove the side-lobes, but we were unable to detect any emission from the location of the core to a limit of approximately 8 mJy ($5\ \sigma$). The upper limit to the flux density of region B at 4.8 GHz is 7 mJy (Gelbord et al., 2005)

[1]The *cordump* patch is available for DIFMAP at `http://astronomy.swin.edu.au/$\sim$elenc/DifmapPatches/`

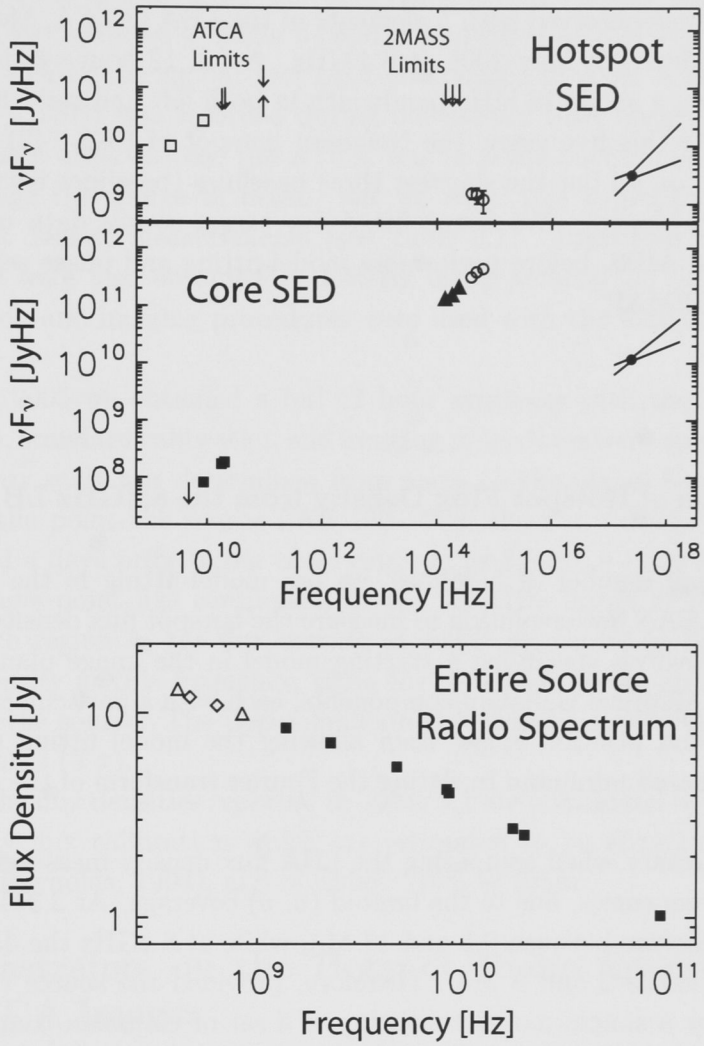

Figure 3.2: Spectral energy distribution of the core and Northern hotspot of PKS 1421–490, as well as the radio spectrum of the entire radio galaxy. Symbols indicate the source of the data as follows: Filled squares, ATCA; open squares, LBA; open circles, Magellan (taken from G05); filled triangles, 2MASS (taken from G05); open triangles, MOST (taken from Large et al. (1981) and Campbell-Wilson & Hunstead (1994)), open diamonds, Parkes (taken from Wills (1975)); filled circles, Chandra (taken from G05). The solid lines through the filled circles indicate the 1σ range of X-ray spectral index permitted by the *Chandra* data. Tips of arrows mark upper and lower limits (see section 3.2.4 for discussion of methods used to obtain ATCA limits). Symbol sizes are greater than or approximately equal to error bars except for those points where error bars have been plotted.

LBA Observations at 8.4GHz

PKS 1421–490 was observed with 5 elements of the LBA (ATCA, Mopra, Parkes, Hobart and Ceduna) in May 2005 at 8.4 GHz. A full 12 hour synthesis was obtained, recording a single 16 MHz bandwidth in both left and right hand circular polarization. At this frequency, the Northern hotspot of PKS 1421–490 is completely resolved on all but the shortest three baselines (baselines between Parkes, the ATCA and Mopra). We fringe fitted our target source data using a point source model in AIPS, before performing model-fitting and phase self calibration iterations in DIFMAP.

Determination of Hotspot Flux Density from the 8.4GHz LBA Data Set

Due to the small number of baselines, we use model-fitting in the (u, v)-plane rather than CLEAN deconvolution to measure the hotspot flux density at 8.4GHz. Model-fitting involves specifying a starting model in the image plane, consisting of a number of elliptical Gaussian components, each with a particular flux density, position, size and position angle, then allowing the model fitting algorithm to locate a chi-squared minimum by fitting the Fourier transform of the model to the (u, v)-data.

Care is necessary when comparing the LBA flux density measurements at the two different frequencies, due to the limited (u, v) coverage. At 2.3 GHz, the data cover (u, v) spacings between 0.5 and 13 Mλ, while at 8.4GHz the data cover (u, v) spacings between 2 and 9 Mλ. Therefore, provided the source structure can be described by a simple model consisting of a set of Gaussian components, the comparison of model flux densities will be valid.

In order to determine the range of allowable flux densities in the 8.4 GHz dataset, we specified a wide range of different models consisting of 3, 4 or 5 elliptical Gaussian components, broadly consistent with the 2.3 GHz image, then let the model-fitting algorithm adjust the model to fit the 8.4 GHz data. While it is not possible to precisely constrain the flux density of the hotspot with only three baselines, we found that the total flux density of all acceptable models (using between three and five elliptical Gaussian components and a wide range of initial model parameters) was never less than 2.9 Jy, and the flux density of the best-fitting model was 3.2 Jy. The 8.6GHz ATCA image contains an unresolved source of 3.3 Jy at the position of the hotspot, and this provides an upper limit to the hotspot flux density at 8.6 GHz. We therefore adopt a hotspot flux density at 8.4 GHz of $F_{8.4\,\mathrm{GHz}} = 3.2^{+0.2}_{-0.3}$ Jy.

3.2.3 ATCA Observations

ATCA observations of PKS 1421–490 were made simultaneously during our LBA observations. We recorded a single 64 MHz bandwidth at 8.4GHz and 128 MHz bandwidth at 4.8GHz during our first LBA observation in 2005. A single 128 MHz bandwidth at 2.3GHz was recorded during our second LBA observation in 2006. For each of these observations, the ATCA was in a compact configuration so we could not image the source in detail, but we were able to obtain accurate total source flux density measurements (see Table 3.1). Total source flux density measurements were also obtained at 1.4GHz using archival ATCA data. Standard calibration and imaging procedures were used with the MIRIAD processing software.

In August 2005 we obtained a full 12 hour synthesis with the new 3mm receivers. Again, standard calibration and imaging procedures were used in MIRIAD. The flux density scale was determined from scans on the planet Uranus and confirmed using the point-like source PKS 1921–293, the flux density of which had been measured 4 days prior to our observing run as 8.8 ± 0.9 Jy at 93.5 GHz. We detected a single point like component in the 93.5GHz image of PKS 1421–490 coincident with region A, the flux density of which we regard as being the total source flux density at this frequency, since the resolution of the shortest baseline is larger than the source. The upper limit on flux density at 93.5 GHz for region B and C is 5 mJy (5 σ).

Errors in the flux densities reported in Table 3.1 are dominated by uncertainties in the primary flux calibration which are estimated to be of order $\sim$2% at cm wavelengths (Reynolds, 1994), and of order $\sim$10% at 3mm.

3.2.4 Constraints on the Hotspot Radio Spectrum from ATCA Images

The hotspot is unresolved in the ATCA images, and is blended with emission from the surrounding regions. We are therefore unable to directly measure the flux density of the hotspot from the ATCA data. However, we are able to constrain the flux density of the hotspot, and we now discuss the methods used to obtain upper and lower limits.

Using radio data that was first presented in Gelbord et al. (2005), we find upper limits on the hotspot flux density at 17.7GHz and 20.2GHz by summing the CLEAN components at the position of the hotspot. Similarly, we obtain an upper limit to the hotspot flux density at 93.5GHz from the measurement of total source flux density at that frequency. We obtain a lower limit on the hotspot flux density at 93.5 GHz via the following steps:

1. We subtract the LBA-measured hotspot flux density from the total source flux density at 2.3GHz and 8.4GHz to obtain two estimates of the non-

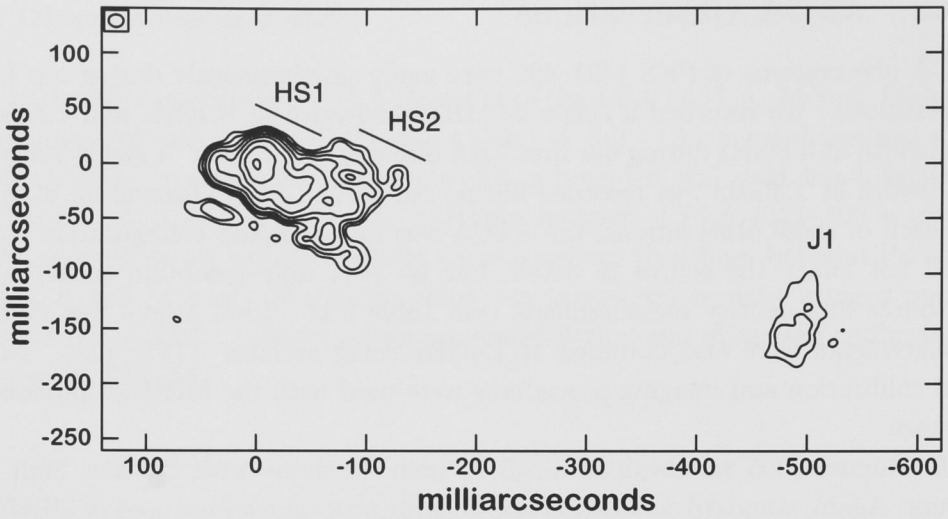

Figure 3.3: VLBI image of the Northern Hotspot of PKS 1421–490 at 2.3 GHz. Contour levels: 3.5 mJy/beam × (1, 2, 4, 8, 16, 32, 64, 128). Peak surface brightness: 0.47 Jy/beam. Beam FWHM: 13.5mas × 11.6mas. The scale of this image is 7.0 pc/milli-arcsecond.

hotspot flux density, from which we calculate a non-hotspot spectral index ($\alpha^{8.4\,\mathrm{GHz}}_{2.3\,\mathrm{GHz}}$(non-hotspot) = 0.78).

2. We extrapolate the non-hotspot power law to 93.5 GHz.

3. We reasonably assume that the non-hotspot spectrum becomes steeper towards higher frequencies. Therefore the extrapolated flux density from step 2 is an upper limit to the non-hotspot flux density.

4. We subtract the non-hotspot upper limit from the observed entire source flux density to obtain a lower limit on the hotspot flux density at 93.5 GHz.

The assumption in step 3 is based on the observation that the non-hotspot emission arises in the lobes, jets and the southern hotspot (the core is negligible). Jet and lobe spectra are often observed to steepen towards higher frequency. Indeed, the 17.7GHz and 20.2GHz ATCA images indicate that the spectral index of the northern lobe region steepens significantly at higher frequency. The limits on hotspot flux density obtained from the ATCA images are represented by the tips of the arrows in Figure 3.2, and are listed in Table 3.1.

3.2.5 Optical Spectroscopy

Optical spectra were taken with the Magellan IMACS camera on 14 May 2005 in service mode. Three ten minute exposures were obtained using a long slit (0.″9

width) aligned with regions A and B. The 300 lines/mm grism was used, to yield a spectral resolution of $R \sim 1000$ spanning roughly 4000–10000 Å. The spectra were reduced with IRAF. No standard stars were observed, so no effort was made to flux calibrate the spectra or to remove telluric absorption features.

No significant spectral features were detected in the spectrum of region A, consistent with synchrotron emission from a hotspot. However, only a very high equivalent width emission line could have been detected due to the low signal to noise ratio of these data.

The spectrum of region B contains several broad and narrow emission lines, which allowed a precise determination of the redshift (see §3.3.1). This is not the first spectrum of the nucleus to be published — a spectrum of region B was presented in G05. However, the spectrum presented in G05 did not allow identification of any spectral lines because the strongest spectral features fell beyond the wavelength coverage, and the spectrum was taken as a single short exposure with a high background due to the pre-dawn sky.

3.3 Region B: The Active Galactic Nucleus

3.3.1 Optical Spectrum of Region B

The normalized optical spectrum of region B is displayed in Figure 3.4. We detect several broad and narrow emission lines: Mg II 2799, [Ne V] 3346 and 3426, the blended [O II] 3726,3729 doublet, [Ne III] 3869 and 3967, Hδ (marginal), Hγ, [O III] 4363, Hβ, and [O III] 4959 and 5007. Hβ has both a broad and narrow component; their measured FWHM values (uncorrected for instrumental resolution) are 6500 km/s and 516 km/s respectively. The narrow Hβ line width is consistent with that of the OIII lines (510 km/s). From these features we measure the redshift $z = 0.6628 \pm 0.0001$.

3.3.2 Spectral Energy Distribution of the Core

We did not detect the active galactic nucleus with the LBA, but obtain an upper limit on the flux density of approximately 8mJy at 2.3GHz. This is consistent with the ATCA core flux density measurements (see Table 3.1). The core is completely dominated by its optical emission. In fact, the optical flux density is so great relative to the radio ($\alpha_{8.6\,\mathrm{GHz}}^{662.4\,\mathrm{nm}} = 0.23 \pm 0.02$), the core would be classified as radio quiet in the strictest sense. The radio to optical spectral index cannot be explained in terms of standard synchrotron self absorption models for flat radio spectra (eg. Marscher, 1988), since this would require at least part of the jet to be self absorbed at optical wavelengths and would imply an unrealistically high magnetic

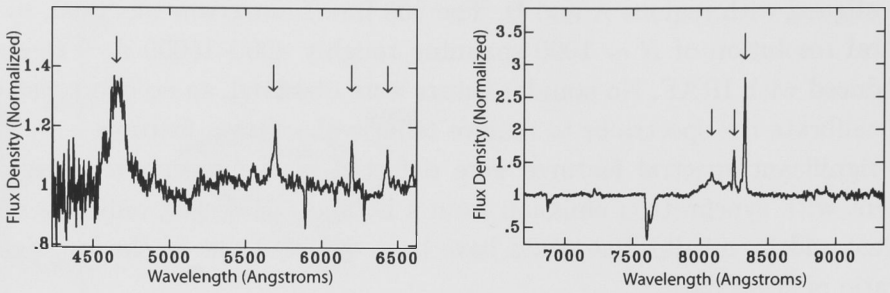

(a) (b)

Figure 3.4: The normalized optical spectrum of region B. This spectrum clearly shows that region B is a broad line AGN at redshift 0.6628. Increasing in wavelength, the arrows indicate the positions of the following emission lines: Mg II 2799, [Ne V] 3426, [O II] 3726/3729, [Ne III] 3869, Hβ, [O III] 4959, [O III] 5007.

field strength. This region has an optical spectral index $\alpha_o = 0.2 \pm 0.1$, in the range typical of quasars (Francis et al., 1991), suggesting that the strong optical emission may be due to an unusually large contribution from the accretion disk thermal component. The radio to X-ray spectral index ($\alpha^{1\,\mathrm{keV}}_{8.6\,\mathrm{GHz}} = 0.710 \pm 0.005$) is typical of radio galaxies and quasars at similar redshift (eg. Belsole et al., 2006; Padovani et al., 2003). The optical to X-ray spectral index is $\alpha_{ox} = 1.62$ (G05). There is clearly an excess of optical flux relative to the radio and X-ray flux when compared to samples of other radio galaxies (eg. Gambill et al., 2003). Note that measurements of the B-band magnitude have shown no variability, to within 0.6 magnitudes, over the past 35 years (GO5).

3.4 The Northern Hotspot

3.4.1 Morphology

Figure 3.3 shows the LBA image of the Northern hotspot at 2.3 GHz. The resolution of this image is 13.5mas × 11.6mas, corresponding to a spatial resolution of approximately 90 pc. Less than 0.2 Jy (5% of the hotspot flux density) remains on the longest baseline ($\sim$ 12.9Mλ), implying that there is little structure on scales smaller than 15 mas (100 pc). This limit on substructure within the hotspot is relevant to possible synchrotron self absorption models for the hotspot spectrum, which we discuss further in §3.4.2.

To place this object in context, I now provide a brief review of the literature involving VLBI studies of the hotspots of radio galaxies and quasars. The following is based on a literature review given in Tingay et al. (2008). There have been relatively few studies of radio galaxy hotspots using VLBI techniques. Kapahi & Schilizzi (1979) presented single-baseline VLBI observations of hot spots in 35 high luminosity, distant ($z \gtrsim 0.5$) FRII radio galaxies and quasars. Compact

components smaller than 150mas, accounting for a significant fraction of the total source flux density were detected in several objects.

Lonsdale & Barthel (1998) presented total intensity and linear polarization VLBA images of a hot spot in 3C 205 (redshift of 1.534), with angular resolution 6.9×8.8 mas (spatial resolution 60 pc). These images revealed a complex structure approximately 300 mas (2.5 kpc) across. Lonsdale & Barthel (1998) interpret the complex VLBI scale structure in terms of a collision between the jet and a dense gaseous obstacle, such as a galaxy in the cluster of 3C 205.

Gurvits et al. (1997) presented VLBI observations of the hot spot in 4C 41.17 (z = 3.8), located at a distance of 2.9kpc from the galaxy nucleus. These images revealed a component of size not more than 15 mas (approximately 110 pc at this redshift) that accounts for 30 percent of the integrated flux density of the hotspot in VLA images. Gurvits et al. (1997) speculate that the VLBI-scale radio structure is associated with an interaction between the jet and a massive clump in the interstellar medium (ISM), causing a deflection in the jet direction.

Young et al. (2005) reported on VLBI observations of the southern lobe hot spot of the nearby radio galaxy PKS 2153?69 (z = 0.028). The hot spot is marginally resolved into three components of between 100220 mas, within a 400 mas diameter area. The spatial resolution of the PKS 2153?69 image was approximately 50 pc.

More recently, Tingay et al. (2008) presented VLBA images of the hotspot of the nearby radio galaxy Pictor A at 23mas resolution, corresponding to spatial resolution of 16pc - more than three times greater spatial resolution than previous VLBI studies of radio galaxy hotspots. The northwest hotspot of Pictor A is resolved into a complex set of compact components. These compact components are identified with strong shocks in the fluid flow, and are suggested to be the sites of synchrotron X-ray emission. The VLBI radio imaging has had a significant impact on the understanding of the X-ray emission from the hotspots of Pictor A (Tingay et al., 2008).

The flux density of the hotspot in our LBA image is 60 % of the total source flux density at 2.3 GHz, and 75 % at 8 GHz. The peak surface brightness is $I^{\rm peak}_{2.3\,{\rm GHz}} = 2600$ Jy/arcsec^2. Extrapolating to 8 GHz assuming $I_\nu \propto \nu^{-0.2}$ (the spectral index of $\alpha \sim 0.2$ between these frequencies is calculated in §3.4.2) and accounting for cosmological dimming and redshifting, we find that the peak surface brightness of the northern hotspot of PKS 1421-490 would be more than 1000 times brighter than the brightest hotspot of Cygnus A if they were at the same redshift (Carilli et al., 1999). The monochromatic hotspot luminosity is $L_{2.3\,{\rm GHz}} = 8 \times 10^{27}$ WHz^{-1}.

A protrusion on the Eastern edge of the hotspot resembles the "compact protrusions" seen in numerical simulations (eg. Norman, 1996). According to Norman (1996), a compact protrusion is produced in their 3-D non-relativistic hydrodynamic simulations when the light, supersonic jet reaches the leading contact discontinuity. At this point, the jet is generally flattened to a width substantially

less than the inlet jet diameter, and the compact protrusion arises where the jet impinges on the contact discontinuity surface.

The width of the hotspot at the peak (region HS1) is 400pc measured perpendicular to the inferred jet direction. The lower surface brightness emission behind the hotspot peak (region HS2) is 700pc measured perpendicular to the jet direction. The length of the hotspot (regions HS1 and HS2) is approximately 1kpc. The geometric mean of the major and minor axes (calculated for comparison with Hardcastle et al. (1998) and Jeyakumar & Saikia (2000)) is 0.63 kpc. This is a factor of 4 below the median value (2.4 kpc) of hotspot sizes given in Hardcastle et al. (1998). However, the size of the hotspot relative to the linear size of the source is consistent with the correlation between these parameters given in Hardcastle et al. (1998) and Jeyakumar & Saikia (2000).

The jet exhibits a bend of almost 60 degrees (projected) approximately 5 arcseconds (35kpc) from the core at the western end of the ridge of emission extending west from the hotspot in Figure 3.1. Bridle et al. (1994) showed that hotspot brightness is anti-correlated with apparent jet deflection angle. They found that, for the twelve quasars in their sample, the ratio of hotspot flux density to lobe flux density decreases with larger jet bending angles, particularly when the deflection occurs abruptly. PKS 1421–490 does not follow this trend.

We detect what appears to be a jet knot (region J1) 512 mas ($\sim$ 3.5 kpc projected) at position angle -107 degrees (North through East) from the hotspot peak. The knot is extended along a position angle almost perpendicular to the apparent jet direction. The major axis of the knot is poorly constrained due to the low signal to noise of this component, but the data suggests a width of approximately 400 - 600pc.

Interpretation of Region HS2

We now consider the interpretation of the lower surface brightness region HS2 just behind the hotspot peak. As mentioned above, the diameter of region HS2 perpendicular to the jet direction (700pc) is much larger than the diameter of region HS1 (400pc). The surface brightness of region HS2 is more than a factor of 10 times the peak surface brightness of the brightest hotspot of Cygnus A. In addition, the flux density from region HS2 alone ($\sim$ 0.6 Jy at 2.3GHz) is more than 4 times the total flux density of the whole counter lobe and hotspot. There are two possible interpretations for region HS2, and the interpretation of this region has implications for the interpretation of region HS1.

The first interpretation is in terms of emission from turbulent back-flow in the cocoon. If this interpretation is correct, we cannot appeal to Doppler beaming to account for the high surface brightness of region HS2 relative to other hotspots, and the high flux density relative to the counter hotspot and lobe. If we cannot appeal to Doppler beaming for region HS2, it would seem unreasonable to appeal

to Doppler beaming to explain the high surface brightness of region HS1. The arm length symmetry places a tight upper limit on the expansion velocity of the lobes at $v_{\rm expansion} < 0.1c$, indicating that the whole complex (region HS1 and HS2) cannot be advancing relativistically.

The second possible interpretation for region HS2 is that the emission is associated with oblique shocks in the jet as it approaches the hotspot. In this case, we may appeal to Doppler beaming to explain the high surface brightness of both regions HS1 and HS2. However, this interpretation would imply that the jet diameter at HS2 (∼700pc) is significantly greater than the diameter of the hotspot at HS1 (∼400pc) and also greater than the jet diameter at J1 ($\sim 400 - 600$pc). It should be noted that the width of region J1, presumably associated with a jet knot, is poorly constrained due to the low signal to noise of this component. Future LBA observations at 1.4GHz may provide better constraints on the size of regions J1 and HS2.

3.4.2 Modeling the Hotspot Spectral Energy Distribution

Low Frequency Flattening

Figure 3.5 illustrates that the hotspot radio spectrum changes slope at GHz frequencies, becoming flatter towards lower frequency. We now discuss this feature in more detail and consider the possible causes.

The hotspot spectral index calculated from our LBA flux density measurements is relatively flat at GHz frequencies ($\alpha^{8.4\,\rm GHz}_{2.3\,\rm GHz} = 0.22^{+0.08}_{-0.05}$). The hotspot spectrum cannot continue with this slope to millimeter wavelengths, since it would substantially over-predict the observed 93.5GHz flux density. We therefore require that the hotspot spectrum be steeper at frequencies above 8GHz, with spectral index $\alpha \gtrsim \alpha^{\rm ATCA\ 93.5\,GHz}_{\rm LBA\ 8.4\,GHz} = 0.48$.

Our conclusion of a flat spectral index at GHz frequencies based on the LBA flux density measurements is strengthened by inspection of the whole source spectrum (see Figure 3.5). The flux density of the entire radio galaxy has a spectral index of 0.58 above 8.4 GHz, but flattens to a spectral index of 0.34 below 4.8 GHz. The northern hotspot is the dominant component at GHz frequencies, hence, the flattening of the total source spectrum implies there is flattening in the hotspot spectrum. There are a number of possible causes of this GHz frequency flattening, but most of them are implausible. We now consider a number of such explanations.

If synchrotron self absorption were responsible for the flattening, the required magnetic field strength is $B_{\rm G} \sim 10^{-5}\nu_p^5\phi^4F_p^{-2}(1+z)^{-1}$ where $B_{\rm G}$ is the magnetic field strength in Gauss, F_p is the peak flux density in Jy, ν_p is the frequency in GHz at the peak and ϕ is the angular size in milliarcseconds (de Young, 2002, pg. 325). In the case of the Northern hotspot of PKS 1421–490 we estimate (conservatively) $\nu_p \sim 1$ GHz, $\phi \sim 100$ mas, $F_p \sim 5$ Jy and z = 0.663. Therefore, a magnetic field strength of $B \sim 20$ G is required to produce the observed flattening — four orders

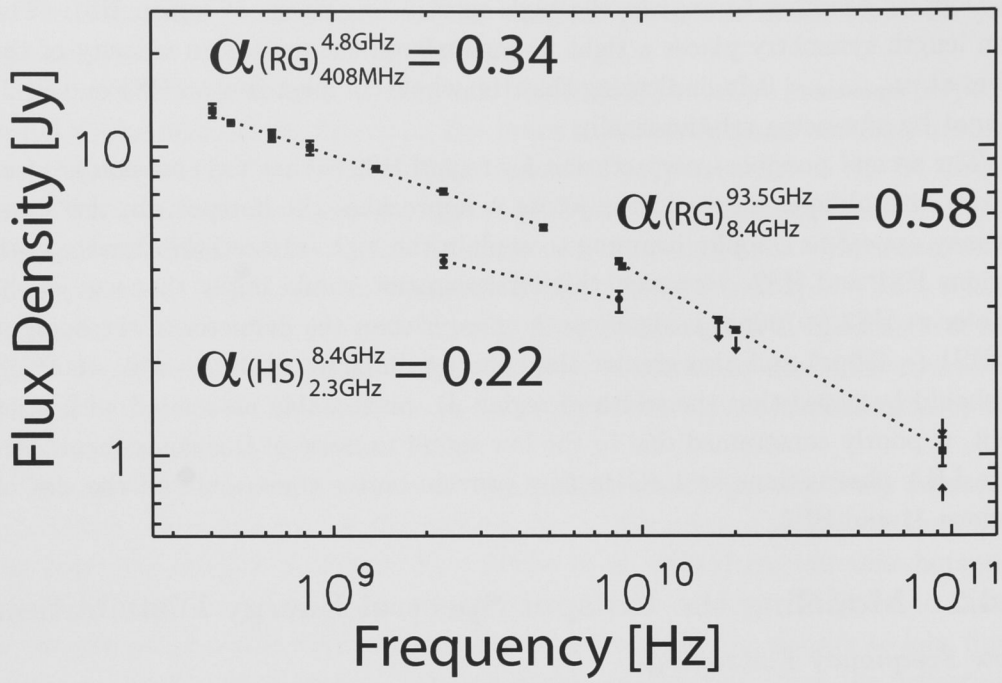

Figure 3.5: Radio spectrum of the entire radio galaxy (filled squares) and hotspot (filled circles and tips of arrows). This figure serves to illustrate the low frequency flattening in the hotspot radio spectrum referred to in the text (§3.4.2 and §3.8). The dotted lines illustrate power law fits to specific sections of the data.

of magnitude greater than the equipartition magnetic field strength. Less than 0.2Jy (5% of the hotspot flux density) remains on the longest baselines (12.9 Mλ $\Rightarrow$ 15 mas resolution), implying that the hotspot cannot be composed of many small self-absorbed sub-components. Therefore, we do not consider synchrotron self absorption to be a viable explanation for the flattening.

We next consider free-free absorption by interstellar clouds in the hotspot environment as a possible mechanism for the observed flattening of the radio spectrum. Consider a cloud of size $L_{\rm kpc}$ kpc, temperature $\mathrm{T}_4 \times 10^4$ K, electron number density n_e cm^{-3} and pressure $p_{-12} \times 10^{-12}$ dyn/cm^2. The optical depth τ to free-free absorption at a frequency $\nu_{\rm GHz}$ GHz is given by (eg. de Young, 2002, pg.326)

$$\tau = 3.3 \times 10^{-4} n_e^2 L_{\rm kpc} \nu_{\rm GHz}^{-2.1} T_4^{-1.35} \quad (3.1)$$

$$= 2 \times 10^{-4} L_{\rm kpc}\, \nu_{\rm GHz}^{-2.1}\, p_{-12}^2 \left(\frac{n_e}{n}\right)^2 T_4^{-3.35} \quad (3.2)$$

Assuming a characteristic pressure in the outer regions of an elliptical galaxy $p \sim 10^{-12}$ dyn/cm^2, a characteristic temperature for an ionized cloud $T \sim 10^4$ K and a reasonable cloud size $L \lesssim 1$ kpc, the optical depth to free-free absorption above 1GHz is less than 5×10^{-5}.

We therefore interpret the change of slope in the hotspot radio spectrum in terms of a change in the underlying electron energy distribution. To account for this feature, we model the SED by incorporating a low energy cutoff in the electron energy distribution. A low-energy cutoff at some minimum Lorentz factor $\gamma_{\rm min}$ produces a spectrum with $F_\nu \propto \nu^{1/3}$ at frequencies below the characteristic emission frequency of electrons with Lorentz factor $\gamma_{\rm min}$ (see eg. Worrall & Birkinshaw, 2006). We must emphasize that an instantaneous cutoff in number density is not physical - it is merely an approximation to a sharp turn-over in the electron energy distribution. In §3.8 we show that interpreting the observed flattening in terms of a turn-over in the electron energy distribution has considerable implications.

Low frequency flattening in hotspot spectra has been observed in a small number of other objects (see §3.1).

The High Frequency Synchrotron Spectrum

The hotspot spectrum remains relatively flat between 8GHz and 93.5GHz, having spectral index $0.4 < \alpha < 0.6$ (based on the two point spectral index from the 8.4GHz LBA data point to the ATCA upper and lower limits at 93.5GHz). The synchrotron spectrum above 93 GHz is poorly constrained, but the simplest model — a power law spectrum with spectral index $0.4 < \alpha < 0.6$ and an exponential cutoff at high frequency (i.e. a synchrotron spectrum from a power law electron energy distribution with number density set to zero above $\gamma_{\rm max}$), is unable to satisfy the optical data and the 2MASS infra-red upper limits simultaneously. Either a break to a steeper spectrum somewhere between $\sim 10^{11} - 10^{13}$ Hz is required, or a gradual cutoff at high electron energy, rather than an abrupt cutoff at $\gamma_{\rm max}$, must exist. Given the high radio luminosity, hence high magnetic field strength, synchrotron losses are likely to be important. We therefore allow for a synchrotron cooling break at an arbitrary break frequency in order to fit the radio through optical spectrum. Different choices of model spectrum are possible, but they would not significantly affect our major results. We discuss the model electron energy distribution in §3.4.2, and further discuss the self-consistency of this model in §3.6.

Hotspot X-ray Emission

Figure 3.6 shows the spectral energy distribution (SED) of the northern hotspot. The level of X-ray flux density relative to the optical flux density indicates the presence of two distinct spectral components: synchrotron emission from radio to optical frequencies, and inverse Compton emission at X-ray frequencies and above.

The energy density of the locally generated synchrotron emission within the hotspot (assuming no Doppler beaming) is more than 10^4 times the energy density of the cosmic microwave background (CMB) at this redshift. If the hotspot plasma is moving relativistically with velocity $v = \beta c$ at an angle θ to the line of sight, the

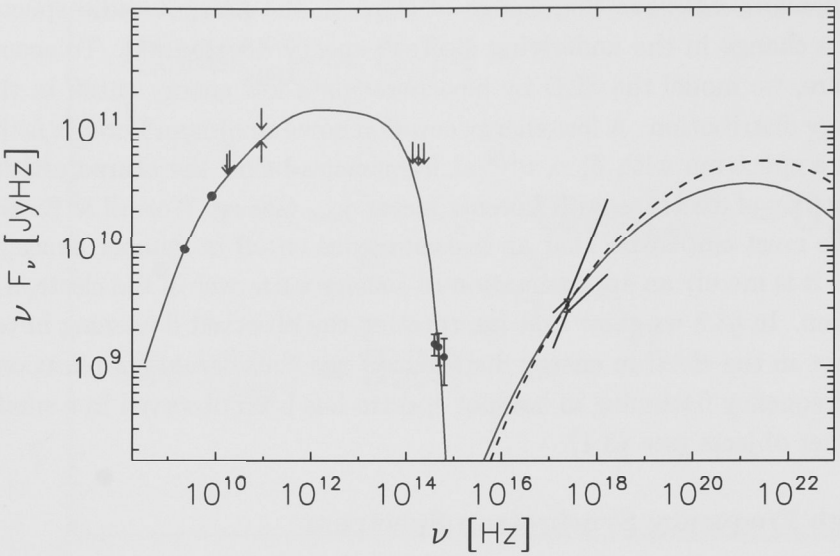

Figure 3.6: Hotspot Spectral Energy Distribution with SSC model overlaid. The "bow-tie" around the X-ray data point indicates the 1σ range of X-ray slopes. The solid line is the best fit synchrotron plus self Compton model spectrum with the Doppler factor fixed at $\delta = 1$. The dashed line is the best fit SSC component with the Doppler factor fixed at $\delta = 3$. The model synchrotron spectra for $\delta = 3$ and $\delta = 1$ are exactly the same, and so do not appear as separate curves in the plot. The LBA data points (plotted as filled circles) have error bars smaller than the symbol size. Tips of arrows mark the position of upper and lower limits. X-ray, optical and infra-red points are taken from Gelbord et al. (2005).

ratio of synchrotron to CMB energy density is reduced by a factor of $\sim \Gamma^{-2}\delta^{-3}$ where $\delta = [\Gamma(1 - \beta\cos\theta)]^{-1}$ is the Doppler factor and $\Gamma = (1-\beta^2)^{-1/2}$ is the bulk Lorentz factor, and we have assumed the hotspot is associated with plasma moving through a stationary volume/pattern rather than a moving blob, so that $I_\nu = \delta^2 I'_{\nu'}$ (Lind & Blandford, 1985). Therefore, if $\delta \lesssim 6$ (assuming $\Gamma \sim \delta$), inverse Compton scattering of locally generated synchrotron photons is the dominant source of inverse Compton X-ray emission. While a Lorentz factor of $\Gamma \sim 6$ is not ruled out, such a high Lorentz factor is not required by the data, and we consider only Lorentz factors $\Gamma \lesssim 3$. We therefore ignore the inverse Compton scattering of CMB photons in the following treatment. We also ignore any contribution to the X-ray flux density from "upstream Compton" scattering (Georganopoulos & Kazanas, 2003), whereby electrons in the jet upstream from the hotspot inverse Compton scatter synchrotron photons produced within the hotspot. We note that if the upstream Compton process makes a significant contribution to the observed X-ray flux density, the SSC flux density must be less than the observed flux density, in which case the magnetic field strength in the hotspot would be greater than that

reported in Table 3.2, and therefore greater than the equipartition value.

Table 3.2. Synchrotron Self Compton Model Parameters for Northern Hotspot

Fixed Parameters					Derived Parameters						
δ	R [pc]	α	ν_b [Hz]	$\nu_{\rm max}$ [Hz]	B [mG]	$B/B_{\rm eq}$	n_e $[\times 10^{-5}{\rm cm}^{-3}]$	$\gamma_{\rm min}$	$\gamma_{\rm b}$ $[\times 10^4]$	$\gamma_{\rm max}$ $[\times 10^5]$	$\alpha_{0.5{\rm keV}}^{7.0{\rm keV}}$
1.0	320	0.53	5×10^{11}	10^{14}	3.2 ± 0.5	$1.5^{+0.3}_{-0.2}$	2.7 ± 0.4	650 ± 80	$\gtrsim 0.8$	1.1 ± 0.1	0.5 ± 0.1
2.0	320	0.53	5×10^{11}	10^{14}	1.0 ± 0.2	0.75 ± 0.15	2.2 ± 0.3	800 ± 100	$\gtrsim 1$	1.4 ± 0.2	0.45 ± 0.1
3.0	320	0.53	5×10^{11}	10^{14}	0.5 ± 0.1	0.5 ± 0.1	1.9 ± 0.3	950 ± 100	$\gtrsim 1.1$	1.6 ± 0.2	0.45 ± 0.1

Note. — The quoted uncertainties on model parameters are an estimate of the level of uncertainty from model fitting, and correspond to the range of parameter values in the set of models having $\chi^2 < \chi^2_{min} + 2.71$.

Synchrotron Self Compton Modeling

To model the radio to X-ray spectral energy distribution we use the standard one-zone SSC model: a spherical region of plasma with uniform density and magnetic field strength. We assume that the magnetic field is "tangled" with an isotropic distribution of field direction. We further assume that the number density of electrons per unit Lorentz factor is described by

$$\bar{N}(\gamma) = \begin{cases} 0 & \gamma < \gamma_{\rm min}, \quad \gamma > \gamma_{\rm max} \\ \frac{K_e \gamma_b}{(a-1)} \gamma^{-(a+1)} g\left(\frac{\gamma}{\gamma_b}\right) & \gamma_{\rm min} < \gamma < \gamma_{\rm max} \end{cases} \tag{3.3}$$

where

$$g\left(\frac{\gamma}{\gamma_b}\right) = \begin{cases} 1 - \left(1 - \frac{\gamma}{\gamma_b}\right)^{a-1} & \gamma < \gamma_b \\ 1 & \gamma > \gamma_b \end{cases} \tag{3.4}$$

$\bar{N}(\gamma)$ is the volume averaged energy distribution produced by continuous injection of a power-law energy distribution $N(\gamma) = K_e \gamma^{-a}$ at a shock with synchrotron cooling in a uniform magnetic field downstream. It describes a broken power-law spectrum with the electron spectral index smoothly changing from -a to -(a+1) at $\gamma \approx \gamma_b$. The break in the electron spectrum at γ_b corresponds to the electron energy at which the synchrotron cooling timescale is comparable to the dynamical timescale for electrons to escape from the hotspot. The synchrotron cooling break is discussed further in §3.6.

For the electron energy distribution described by $\bar{N}(\gamma)$, and given a particular radius, redshift, Doppler factor and spectral index, the synchrotron plus self Compton spectrum is characterized by the five parameters $K_e, B, \gamma_{\rm min}, \gamma_b, \gamma_{\rm max}$. In calculating the model spectrum, these parameters appear in the following combinations (see §2.5.2):

$$A_{\rm syn} = K_e \Omega_0^{\alpha+1} \tag{3.5}$$

$$A_{\rm ssc} = K_e \gamma_b \tag{3.6}$$

$$\nu_1 = \frac{\delta}{(1+z)} \frac{3}{4\pi} \Omega_0 \gamma_{\rm min}^2 \tag{3.7}$$

$$\nu_b = \frac{\delta}{(1+z)} \frac{3}{4\pi} \Omega_0 \gamma_b^2 \tag{3.8}$$

$$\nu_2 = \frac{\delta}{(1+z)} \frac{3}{4\pi} \Omega_0 \gamma_{\rm max}^2 \tag{3.9}$$

where $\alpha = (a-1)/2$ is the radio spectral index between frequencies ν_1 and ν_b, Ω_0 is the non-relativistic gyro-frequency. The parameters ν_1, ν_b and ν_2 correspond to the characteristic frequency emitted by electrons with Lorentz factor $\gamma_{\rm min}$, γ_b and $\gamma_{\rm max}$ in a magnetic field of flux density B, and are therefore identified with the low frequency turn-over, synchrotron cooling break and high frequency cutoff

respectively. The advantage of this formulation, described in §2.5.2, is that it allows the model to be specified in terms of the observed values of ν_1, ν_b and ν_2. The parameters $A_{\rm syn}$ and $A_{\rm ssc}$ are normalization factors for the synchrotron and SSC spectral components respectively.

We estimate best fit values for B, K_e, $\gamma_{\rm min}$, $\gamma_{\rm b}$ and $\gamma_{\rm max}$ using chi-squared minimization with the following three constraints: (1) We fix the electron energy index at $a = 2.06$ so that the spectral index $\alpha = 0.53$ for frequencies $\nu_1 << \nu << \nu_b$ (that is, between about 10 GHz and 100 GHz). This is the electron energy index determined from modeling the hotspot radio spectrum as described in §3.5. The spectral index $\alpha = 0.53$ also agrees with the ratio of peak surface brightness (at the location of the hotspot) in the 17.7GHz and 20.2GHz ATCA images. (2) We fix the radius at R = 320pc. The radio hotspot is elongated in an approximately cylindrical shape of volume $V \approx 4 \times 10^{57}$ m^3. This calculation neglects the effects of projection. Hence, the true volume may be greater than the value used in these calculations. However, for the purposes of the current study, the above mentioned volume is a satisfactory estimate. A radius of 320pc gives a spherical model of equal volume. (3) We fix the break frequency at $\nu_b = 500$ GHz. This is close to the lowest break frequency allowed by the data. Higher break frequencies are permitted but cause a worse fit to the optical data. The break frequency is not well constrained by the data, but the results are not sensitive to the assumed value of the break frequency. (4) We fix the upper cutoff frequency at $\nu_{\rm max} = 10^{14}$ Hz to fit the optical flux densities.

We determined best fit parameter values while fixing the Doppler factor at $\delta = 1, 2$ and 3. The derived model parameters are presented in Table 3.2. The uncertainties in Table 3.2 are determined from the range of parameter values in the set of models having $\chi^2 < \chi^2_{\rm min} + 2.71$. The observed X-ray spectral index was not included in the chi-squared calculations, but the model X-ray spectral index is consistent with the observed value within the uncertainties.

In Figure 3.6 we plot the observed hotspot flux densities with the best fit model spectra (for Doppler factors fixed at $\delta = 1$ and $\delta = 3$) overlaid. The simple one-zone model with a near equipartition magnetic field strength provides a good description of the available data. Hardcastle et al. (2002) used more complicated spectral and spatial models for three sources, and found that this did not have a significant effect on the derived plasma parameters. We are therefore confident in our parameter estimates using this "first-order" one-zone model.

3.5 Modeling the Radio Spectrum of the Entire Radio Galaxy

We now describe a consistency check for the model of the hotspot radio spectrum in terms of a cutoff in the electron energy distribution at $\gamma_{\rm min}$. This check is based

on the observed flattening in the spectrum of the entire radio galaxy (Figure 3.7). In order to test whether the observed flattening is consistent with the inferred low energy cutoff in the electron distribution, we fit a simple two-component model to the radio galaxy spectrum between 408 MHz and 93.5GHz. The model components are: (1) The synchrotron spectrum produced by the electron energy distribution of equation (3.3). This component describes emission from the hotspot. (2) A pure power-law approximating emission from the rest of the source. Note that the core flux density is negligible compared with that of the jets, lobes and hotspots, so that no component is included to represent emission from the AGN.

The synchrotron spectrum of component 1 is calculated using equation (2.91). We assume the same source volume as in §3.4.2, fix the lab frame break frequency at $\nu_{\rm b} = 500$ GHz and the lab frame high frequency cutoff at $\nu_2 = 1.1 \times 10^{14}$ Hz, consistent with the values determined from modeling the hotspot spectrum in §3.4.2. With these assumed values, the parameters ν_b and ν_2 do not affect the shape of the spectrum below about 100 GHz, but they weakly affect the calculation of equipartition magnetic field strength. The spectrum of component 1 is therefore determined by the spectral index α_1, the turn-over frequency ν_1 and the synchrotron amplitude $A_{\rm syn} = K_e \Omega_0^{\alpha_1+1}$. The flux density of the second component is of the form

$$F_{\nu,2} = F_{2.3\,\mathrm{GHz},2} \left(\frac{\nu}{2.3\ \mathrm{GHz}} \right)^{-\alpha_2} \tag{3.10}$$

Chi-squared minimization was used to determine the best fit values for the parameters α_1, $A_{\rm syn}$, $\nu_{\rm min}$, $F_{2.3\,\mathrm{GHz},2}$ and α_2. The resulting model is shown in Figure 3.7. This simple two-component model provides an excellent fit to the radio galaxy spectrum. Component 1 (describing emission from the hotspot) is in good agreement with the LBA flux density measurements at 2.3GHz and 8.4 GHz. We emphasize that the LBA flux density measurements were not included in the fitting process, but are included in Figure 3.7 for comparison with the spectrum of component 1.

Again, we point out that the cutoff in number density per unit Lorentz factor below $\gamma_{\rm min}$ used in our modeling is not physically realistic, it is merely an approximation to an electron energy distribution with a sharp turn-over. The success of this simple model in simultaneously accounting for the flattening in both the hotspot spectrum and the radio galaxy spectrum supports an interpretation of the flattening in terms of a sharp turn-over in the hotspot electron energy distribution at a Lorentz factor of order $\gamma \sim 600$.

3.6 Synchrotron Cooling Break

The magnetic field strength inferred from spectral modeling in section 3.4.2 implies that there should be a synchrotron cooling break in the hotspot radio spectrum at ~ 1 GHz if the electron energy distribution injected at the shock is a pure power

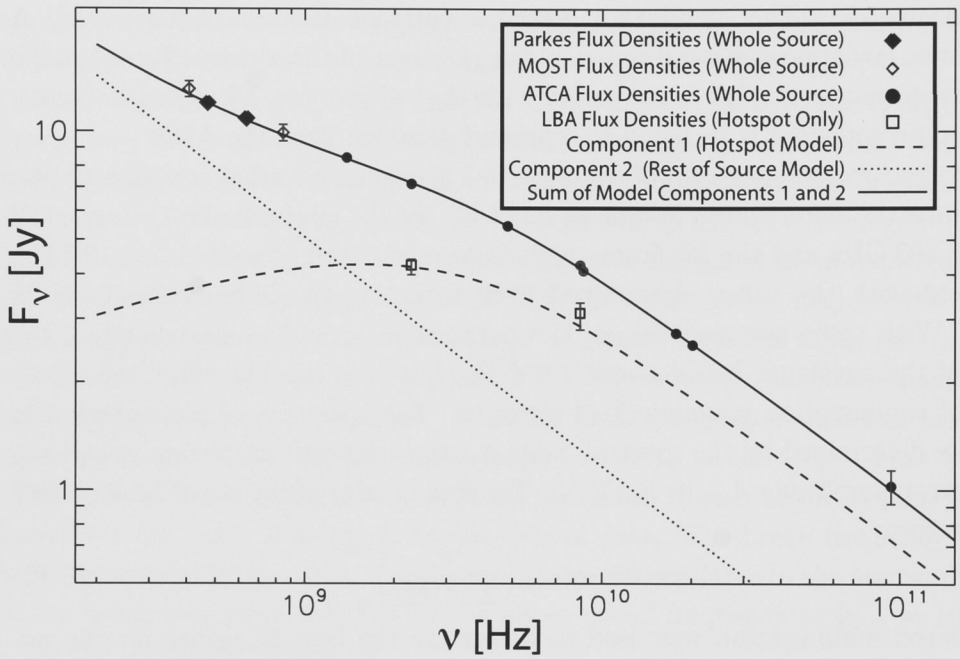

Figure 3.7: Radio spectrum of the radio galaxy PKS 1421–490. Open diamonds represent flux densities of the entire radio galaxy from the Molonglo Synthesis Radio Telescope (MOST). Filled diamonds represent flux densities of the entire radio galaxy from the Parkes telescope. Filled circles represent flux densities of the entire radio galaxy from the ATCA. Open squares represent flux densities of the Northern hotspot from the LBA (see Table 3.1). Also shown is the spectral decomposition described in section 3.5. Component 1 (curved dashed line) is the angle-averaged synchrotron spectrum from a power-law electron distribution of the form $N(\gamma) \propto \gamma^{-2.06}$ with a low energy cutoff at a Lorentz factor corresponding to $\nu_1 = 2.6$ GHz (see equation (3.7)). This component describes emission from the hotspot, and is consistent with the LBA flux densities plotted as open squares. Component 2 (straight dotted line) is a pure power-law with spectral index 0.64. This component is an approximation to the emission from the rest of the source. The solid line is the sum of components 1 and 2. Model parameters are given in Table 3.3.

.

Table 3.3. Model Parameters from Fitting the Radio Spectrum of the Entire Radio Galaxy

Component 1 (Hotspot)					Component 2	
F(2.3GHz) [Jy]	α	ν_1 [GHz]	B_{eq} [Gauss]	γ_{min}^{eq}	F(2.3GHz) [Jy]	α
4.15 ± 0.6	$0.53^{+0.1}_{-0.3}$	$2.6^{+0.3}_{-0.5}$	$2.05^{+0.35}_{-0.1} \times 10^{-3}$	550^{+50}_{-100}	3.0 ± 0.6	0.65 ± 0.1

Note. — The quoted uncertainties on model parameters are an estimate of the level of uncertainty from modelfitting, and correspond to the range of parameter values in the set of models having $\chi^2 < \chi^2_{min} + 2.71$.

law. This is inconsistent with the lower limit on the break frequency estimated from spectral modeling, $\nu_b \gtrsim 500$ GHz. In this section we consider the production of the cooling break, and possible reasons for the inconsistency.

The standard continuous injection hotspot model (Heavens & Meisenheimer, 1987) predicts that the radio spectrum will steepen from α_{in} to $\alpha_{in} + 0.5$ at a frequency, ν_b, corresponding to the electron energy at which the synchrotron cooling time-scale $\tau_{\rm cool}$ is equal to the dynamical time-scale $\tau_{\rm esc}$ for electrons to escape the hotspot. The break frequency is an important constraint on the physics of the hotspot. In general, it depends on the magnetic field strength, hotspot radius, outflow velocity, Doppler factor and the presence or absence of a re-acceleration mechanism within the hotspot. We consider a model in which the escape time-scale τ_{esc} is the time taken for the flow to cross the hotspot and the cooling time-scale is the synchrotron half-life. Let R be the hotspot radius, $v = \beta_{\rm f} c$ the flow velocity within the hotspot (note that this is not the same as the advance velocity of the hotspot), $\delta_{\rm f}$ the corresponding Doppler factor of the flow within the hotspot, and U_B the magnetic field energy density ($U_B = B^2/2\mu_0$ in S.I. units, $U_B = B^2/8\pi$ in c.g.s. units).

$$\tau_{\rm esc} = \frac{2R}{\beta_{\rm f} c} \tag{3.11}$$

$$\tau_{\rm cool} = \frac{\gamma}{|d\gamma/dt|} \tag{3.12}$$

$$= \frac{3 m_e c}{4 \sigma_T U_B \gamma} \tag{3.13}$$

Equating the two time-scales and combining with equation (3.8) for the break frequency in terms of the break Lorentz factor, we obtain the following expression for the break frequency

$$\nu_{\rm b} \approx 60 \frac{\delta_{\rm f}^{\frac{7+4\alpha}{\alpha+1}} \beta_{\rm f}^2}{(1+z)} \left(\frac{B_{\delta_{\rm f}=1}}{\rm mG}\right)^{-3} \left(\frac{R}{\rm kpc}\right)^{-2} \rm GHz \tag{3.14}$$

$$= 60 \frac{\delta_{\rm f}^6 \beta_{\rm f}^2}{(1+z)} \left(\frac{B_{\delta_{\rm f}=1}}{\rm mG}\right)^{-3} \left(\frac{R}{\rm kpc}\right)^{-2} {\rm GHz} \qquad (\alpha = 0.5) \qquad (3.15)$$

where $B_{\delta_{\rm f}=1}$ is the magnetic field strength derived from SSC modeling under the assumption $\delta_{\rm f} = 1$. For a Doppler factor $\delta_{\rm f} = [\Gamma(1 - \beta_{\rm f} \cos\theta)]^{-1}$, the magnetic field strength estimated from SSC modeling is reduced by a factor of approximately $\delta_{\rm f}^{-\frac{\alpha+2}{\alpha+1}}$ (eg. Worrall & Birkinshaw, 2006). Equation (3.15) exhibits a strong dependence on the Doppler factor because of the strong dependence of the break frequency on the magnetic field strength.

Let us first consider the production of the cooling break in a hotspot associated with a strong relativistic normal shock in which the post-shock velocity $\beta_{\rm f} \approx 0.3$, $\delta_{\rm f} \approx 1$, redshift $z = 0.663$, magnetic field $B = 3$ mG (as determined from SSC modeling in §3.4.2) and radius R=0.3kpc (half the geometric mean of the longest and shortest angular sizes of the 2.3GHz LBA image). For such a model, the predicted break frequency is $\nu_b \approx 1$ GHz. This is inconsistent with the lower limit from spectral modeling, $\nu_b \gtrsim 500$ GHz. Moreover, the break frequency estimated from spectral modeling is inconsistent with the proposed correlation between break frequency and equipartition magnetic field strength (eg. Brunetti et al., 2003; Cheung et al., 2005) which also predicts a break frequency $\nu_b \sim 1$ GHz. The discrepancy between predicted break frequency and the observed lower limit would be alleviated if the magnetic field strength were $\lesssim 0.15$ of the value estimated from SSC modeling. However, if this were the case, the model SSC spectrum would over-predict the observed X-ray flux density.

Let us now consider the effect of Doppler beaming on the observed break frequency as a possible means of resolving this difficulty. Assuming a post-shock flow velocity $\beta_{\rm f}^2 \sim (1 - \delta_{\rm f}^{-2})$ and a spectral index of $\alpha \sim 0.5$, a moderate Doppler factor $\delta_{\rm f} \gtrsim 1.9$ is sufficient to increase the predicted break frequency above 500 GHz, while maintaining agreement between the SSC model spectrum and the observed flux densities.

There is also the possibility that distributed re-acceleration within the hotspot is affecting the production of the cooling break. Meisenheimer et al. (1997) have suggested that distributed re-acceleration is required to explain the spectra of the so-called low-loss hotspots. These are hotspots whose spectra are characterized by a power-law with $\alpha \approx 0.6 - 0.8$ that extends to high frequency ($\nu > 10^{12}$ Hz) without the predicted break in the spectrum. Distributed re-acceleration has also been proposed to explain the diffuse infrared/optical emission observed around some hotspots (Prieto et al., 2002; Roeser & Meisenheimer, 1987; Meisenheimer, 2003), as well as the variation in the X-ray spectral index around the hotspots of Cygnus A (Bałucińska-Church et al., 2005), and the existence of flat radio spectrum regions distributed over much of the hotspot area in Cygnus A (Carilli et al., 1999). The favoured mechanism for re-acceleration is stochastic (second order Fermi) acceleration via magnetohydrodynamic turbulence (Meisenheimer et al.,

1997; Prieto et al., 2002; Bałucińska-Church et al., 2005).

Lastly, it is possible that there is more than one site of particle injection, or that the hotspot is not in a steady state.

3.7 Is Doppler Beaming Significant in the Northern Hotspot of PKS 1421–490?

The aim of this section is to assess the likelihood that emission from the the northern hotspot of PKS 1421–490 is Doppler beamed. To do so, in §3.7.1 we lay out the evidence for Doppler beaming in the northern hotspot, then discuss results of numerical simulations and radio studies that indicate Doppler beaming may be significant in hotspots of radio galaxies and quasars. In §3.7.2 we consider the angle to the line of sight of PKS 1421–490, which should be small if Doppler beaming is to be important. In §3.7.3 we estimate the magnitude of the Doppler factor that would be required to account for various properties of the hotspot. In §3.7.4 we discuss two possible arguments against Doppler beaming.

3.7.1 Arguments for Doppler Beaming

The northern hotspot of PKS 1421–490 is extremely luminous at both radio and X-ray wavelengths. The X-ray luminosity between 2 and 10 keV, $L_{2-10\,\mathrm{keV}} = 3 \times 10^{44}\,\mathrm{ergs\,s^{-1}}$, is comparable to the X-ray luminosity of the entire jet of PKS 0637–752, without relativistic corrections. The peak radio surface brightness is hundreds of times greater than that of the brightest hotspot in Cygnus A (Carilli et al., 1999). Consequently, the equipartition magnetic field strength for a Doppler factor of unity is greater by a factor of ∼5 - 10, and the minimum energy density is greater by a factor of ∼50 than values typically evaluated for bright hotspots in other radio galaxies (Meisenheimer et al., 1997; Tavecchio et al., 2005; Kataoka & Stawarz, 2005). The northern hotspot contributes 60% of the total source flux density at 2.3 GHz, and 75% at 8 GHz. Identifying the peak of region C in the ATCA image as the counter hotspot, we estimate the hotspot to counter hotspot flux density ratio to be $R_{hs} \sim 300$ at 20 GHz. In the *Chandra* X-ray band, the counter-hotspot is undetected, and we conservatively estimate $R_{hs} > 100$ at X-ray wavelengths. These are all indications that the hotspot emission may be Doppler beamed. Moreover, we have shown in §3.6 that Doppler beaming may account for the absence of a synchrotron cooling break below 500 GHz. We now discuss the results of numerical simulations and radio studies that indicate Doppler beaming may be important in hotspots of radio galaxies.

Numerical simulations of supersonic jets in 2 and 3 dimensions (eg. Aloy et al., 1999; Norman, 1996; Komissarov & Falle, 1996; Tregillis et al., 2001) suggest that flow speeds in and around hotspots can be much larger than those expected from

the 1D strong shock model, because the shock structure at the jet termination is more complex than a single terminal Mach disk. The simulated jets undergo violent structural and velocity changes near the jet head due to pressure variations in the turbulent cocoon. These violent changes in the jet affect the hotspot structure, and may result in an oblique shock (or shocks) near the hotspot (Aloy et al., 1999; Norman, 1996). The post-shock velocity of an oblique shock can be much higher than the post-shock velocity of a normal shock if the angle between the flow velocity and the shock normal is close to the Mach angle. Therefore, the instantaneous flow velocity through the hotspot may be high enough to produce significant Doppler effects (Aloy et al., 1999).

If the terminal shock is not highly oblique, the post-shock velocity may be relativistic if the jet contains a dynamically important magnetic field. The magnetic field can reduce the shock compression ratio and result in a higher post-shock Lorentz factor than that in an un-magnetized shock (see eg. Double et al., 2004). The post-shock velocity in a magnetized shock depends on the the angle between the magnetic field and the shock plane, the equation of state in the pre- and post-shock plasma, and the magnetization parameter $\sigma = B^2/4\pi\rho c^2$ (Double et al., 2004). In the case where the magnetic field is perpendicular to the jet direction, significant post-shock Lorentz factors ($\Gamma_2 \gtrsim 2$) can be achieved if $\sigma \gtrsim 3$, depending on the equation of state. We suggest that, given the high magnetic field strength in the northern hotspot of PKS 1421–490, magnetic cushioning of the terminal shock due to the presence of a strong magnetic field in the jet may be important.

In addition to the results of numerical simulations, observational evidence also indicates that Doppler beaming of hotspot emission may be significant. For example, the brighter and more compact hotspot is generally found on the side of the source with the brighter kpc-scale jet (eg. Bridle et al., 1994; Hardcastle et al., 1998). This effect is more evident in samples of quasars than in samples including low power sources, which suggests that the observed correlation between hotspot brightness and jet brightness is related to Doppler beaming (Hardcastle et al., 1998). However, Hardcastle (2003) suggest that only moderate hotspot flow velocities ($\beta \sim 0.3$) are required to account for this observed correlation. Dennett-Thorpe et al. (1997) found that regions of high surface brightness in the lobes of radio galaxies have flatter radio spectra on the side corresponding to the brighter jet. They suggest that Doppler shifting of a curved hotspot spectrum may produce such a correlation. Again, only moderate flow speeds of $\beta \lesssim 0.5$ are required to account for this correlation (Ishwara-Chandra & Saikia, 2000). Georganopoulos & Kazanas (2003) have suggested that deceleration of a relativistic flow from $\Gamma \sim 3$ to $\Gamma \sim 1$ in hotspots can explain the wide range of observed hotspot SEDs as being purely an effect of source inclination. However, Hardcastle (2003) and Hardcastle et al. (2004) have contested this interpretation. Rather, they argue, the shape of the hotspot SED depends only on the hotspot radio luminosity.

3.7.2 Jet Inclination Angle

We now consider the angle to the line of sight for PKS 1421–490, if Doppler beaming is to be important.

The active galactic nucleus of PKS 1421–490 exhibits broad emission lines (see §3.3.1). On the basis of the unified scheme for active galaxies, we therefore expect the angle to the line of sight to be less than ~45° (Urry & Padovani, 1995). Another indication of a small angle to the line of sight is the existence of a 60° bend in the northern jet, approximately 5 arcseconds (35kpc) from the AGN at the western end of the ridge of emission extending west from the hotspot in Figure 3.1. Such a large jet deflection is hard to understand if it is indicative of the true bending angle. The well known resolution to this problem is that the jet is viewed close to the line of sight, and the effect of projection causes a relatively small jet deflection to appear much larger than it actually is.

3.7.3 Estimates of the Doppler Factor

We now consider the magnitude of the Doppler factor that would be required to account for the various observed properties.

Let R_{hs} be the hotspot to counter hotspot flux density ratio, β_{hs} the bulk flow velocity in the hotspot divided by the speed of light, θ the jet angle to the line of sight, and α the spectral index. If the two hotspots of PKS 1421–490 are identical, and the difference in flux density is purely the result of relativistic beaming, then

$$\beta_{hs} \cos\theta = \frac{R_{hs}^{\frac{1}{2+\alpha}} - 1}{R_{hs}^{\frac{1}{2+\alpha}} + 1} \tag{3.16}$$

(eg. de Young, 2002, pg. 73).

The observed hotspot to counter-hotspot flux density ratio is $R_{hs} \sim 300$ at 20.2 GHz, hence: $\beta_{hs} \cos\theta \sim 0.81$, $\Gamma_{hs} > 1.7$, and $\theta < 36°$. A moderate Lorentz factor of $\Gamma_{hs} \gtrsim 1.7$ can account for the observed hotspot flux density ratio. The bend in the northern jet means that we cannot assume the same inclination angle for the jet and counter-jet, so equation (3.16) does not strictly apply, but the above calculations serve to illustrate that the required Lorentz factor is not large. If the jet is angled close to the line of sight, the real difference in inclination angle between jet and counter-jet may not be large.

It should be noted that there is a difference between the times at which we see the two hotspots. In the case of PKS 1421–490 this difference is approximately $(3 \times 10^5 / \tan\theta)$ yrs, where θ is the angle to the line of sight. In equation (3.16) there is an implicit assumption that the brightness of the hotspots remain constant over a time-scale of approximately $10^5 - 10^6$ years.

We summarize below the estimates of the Doppler factor required to account for various properties of the hotspot.

1. A bulk Lorentz factor $\Gamma \gtrsim 1.7$ is required to account for the observed hotspot to counter hotspot flux density ratio of $R_{hs} \sim 300$. If the bend in the Northern jet is such that a decrease in inclination angle is produced, the required bulk Lorentz factor is lower.

2. A Doppler factor $\delta \gtrsim 1.9$ is required to account for the observed lower limit on the break frequency $\nu_b \gtrsim 500$ GHz (see §3.6).

3. A Doppler factor $\delta \sim 3$ is required to reduce the SSC model magnetic field strength to a value comparable to that calculated for other radio galaxies ($\sim 100 - 500\,\mu$G) (Kataoka & Stawarz, 2005). However, such agreement is not essential since some variation in the radio galaxy population would be expected.

3.7.4 Arguments Against Doppler Beaming

In §3.4.1 we argued that the broad emission to the west of the hotspot peak (region HS2) may be associated with turbulent back-flow in the cocoon, and therefore cannot be Doppler beamed. As further discussed in §3.4.1, if the high surface brightness of region HS2 is not the result of Doppler beaming, then it seems unreasonable to argue that the high surface brightness of region HS1 is the result of Doppler beaming.

Another possible argument against Doppler beaming comes from interpreting the radio polarization. Figure 3.8 is a contour map of the linearly polarized intensity at 20 GHz in the vicinity of the hotspot, with polarization position angle indicated by the vectors overlaid. The main peak in the contour map is associated with the hotspot (regions HS1 and HS2). The offset of the secondary peak relative to the main peak places it at the same position as region J1 in Figure 3.3. The position angle of the E-vectors in the hotspot indicate that the magnetic field (perpendicular to the E-vectors) is aligned nearly perpendicular to the jet direction. The magnetic field direction is often identified with the shock plane, because the component of the magnetic field in the plane of the shock is amplified, while the component of magnetic field perpendicular to the shock plane is conserved. Figure 3.8 therefore indicates that the terminal shock is not highly oblique. If the terminal shock is not highly oblique the post-shock velocity cannot be highly relativistic unless the magnetic field is dynamically important (see §3.7.1 and Double et al. (2004)). If the magnetic field is dynamically important, this argument against Doppler beaming based on the polarization position angle is not valid.

Could it be the case that the brightness asymmetry between the two hotspots is due to environmental differences? Choi et al. (2007) studied three-dimensional hydrodynamic interactions of relativistic jets with dense clouds using a wide range of jet and cloud properties. They found that indeed the peak surface brightness of the hotspot increased steeply as the jet hit the cloud, but only by a factor of $\lesssim 10$.

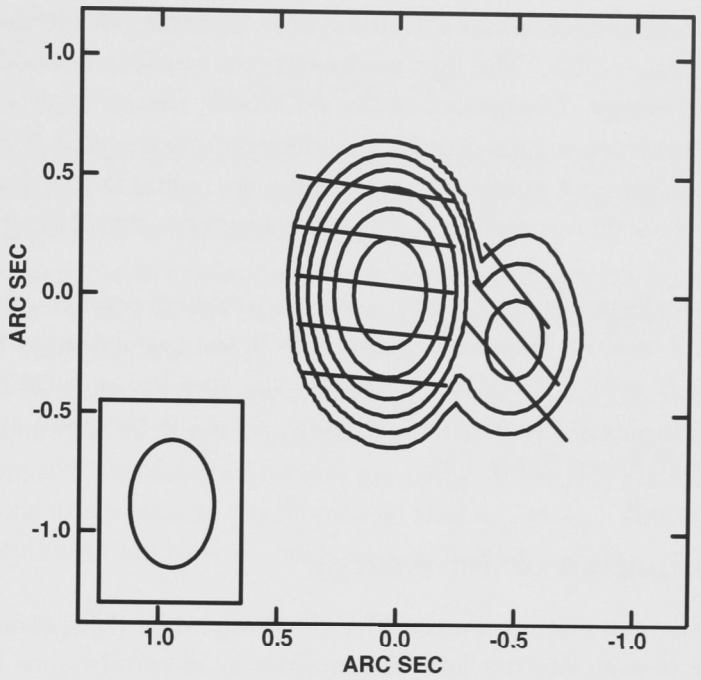

Figure 3.8: 20.16GHz ATCA contours of polarized intensity with polarization E-vectors overlaid. The length of the polarization E-vectors is proportional to the fractional polarization, with 1 arcsecond corresponding to 15% fractional polarization. The polarization vectors have been rotated by -1.8 degrees to account for the observed rotation measure of $\sim$ 140 rad/m^2. The main peak corresponds to the hotspot (regions HS1 and HS2), while the secondary peak is associated with region J1 in Figure 3.3, presumably associated with a jet knot. Both regions are approximately 8% – 10% polarized. The map peak is 0.19 Jy/beam. Contour levels: 3.5 mJy/beam $\times$ (1, 2, 4, 8, 16, 32, 64). Beam FWHM: 0.54 $\times$ 0.36 arcsec. The scale of this image is 7.0 kpc/arcsecond.

In addition, the one dimensional relativistic shock jump conditions suggest that for very light jets the hotspot pressure is insensitive to the properties of the external medium (see Safouris et al., 2008). Therefore, it is unlikely that environmental differences play a significant role in the brightness asymmetry between the hotspot and counter-hotspot.

3.8 Interpreting the Low Frequency Flattening in the Radio Spectrum of the Northern Hotspot

The aim of this section is to consider the implications of the observed flattening in the hotspot radio spectrum discussed in §3.4.2 and illustrated in Figure 3.5. We

consider two possible mechanisms for producing a flattening in the electron energy distribution at $\gamma_{\rm min} \sim 650$. The first mechanism we consider is the dissipation of jet bulk kinetic energy. Dissipation of the jet kinetic energy depletes low energy particles and produces a turn-over in the electron spectrum at a characteristic energy that depends on a number of parameters, including the jet Lorentz factor. The second mechanism we consider is a transition between two distinct acceleration mechanisms.

We note that the inferred value of $\gamma_{\rm min}$ is only weakly dependent on the assumed Doppler factor δ because Doppler beaming affects the calculation of the magnetic field strength ($B \propto \delta^{-(2+\alpha)/(1+\alpha)}$) as well as the rest frame emission frequency corresponding to $\gamma_{\rm min}$ ($\nu' \propto \delta^{-1}\nu$). The value of $\gamma_{\rm min}$ is therefore approximately proportional to $\delta^{1/3}$ (see Table 3.2).

3.8.1 Dissipation of Jet Energy

As an illustrative calculation, we consider the dissipation of jet energy in a cold, un-magnetised proton/electron jet. The analysis is effectively done in two steps: First, we use the conservation of energy and particles to calculate the mean Lorentz factor in the hotspot as a function of jet Lorentz factor. We then relate the mean electron Lorentz factor to the peak Lorentz factor by assuming a particular form for the electron energy distribution. We do not specify the process by which the electrons and protons equilibrate. However, recent particle-in-cell simulations demonstrate that protons and electrons equilibrate in un-magnetised collisionless shocks (Spitkovsky, 2008).

The aim of this calculation is to estimate the jet Lorentz factor required to produce a turn-over in the electron energy distribution at $\gamma_{\rm min} \sim 650$ if the jet bulk kinetic energy is carried by protons and efficiently transfered to electrons in the hotspot. This analysis can easily be extended to include different jet compositions, different proton to electron energy density ratios and the effects of the magnetic field.

Model Assumptions and Definitions

The relevant quantities are defined as follows: γ is the Lorentz factor of an individual particle measured in the plasma rest frame, γ_p is the electron Lorentz factor at the peak of the electron energy distribution, Γ is the bulk Lorentz factor of the plasma, $\beta = \sqrt{1-\Gamma^{-2}}$ is the corresponding plasma speed in units of the speed of light c, θ is the angle between the plasma velocity and the line of sight, $\delta = [\Gamma(1-\beta\cos\theta)]^{-1}$ is the Doppler factor, $N(\gamma)$ is the number density of electrons per unit Lorentz factor, $\langle\gamma\rangle = \int \gamma N(\gamma)d\gamma / \int N(\gamma)d\gamma$ is the mean Lorentz factor, $n = \int N(\gamma)d\gamma$ is the number density, $\epsilon = (\langle\gamma\rangle - 1)\,nmc^2$ is the internal energy density, $\rho = nm$ is the rest mass density in the plasma rest frame, p is the pressure

and w is the relativistic enthalpy density. The relativistic enthalpy density is

$$w = \epsilon + p + \rho c^2 \tag{3.17}$$

We assume the plasma is comprised of electrons (subscript e) and protons (subscript p). Quantities with the subscript 1 refer to the jet plasma, while quantities with a subscript 2 refer to the hotspot plasma.

We assume that the relativistic enthalpy density in the jet is dominated by the rest mass energy density of the the proton component, so that $w_1 \approx \rho_{1,p}c^2$. This assumption is valid provided $\langle\gamma\rangle_{1,e} << m_p/m_e$.

We assume that the electron population is ultra-relativistic ($\epsilon_e = 3p_e$), and that the proton population in the hotspot plasma is, at best, only mildly relativistic, and can be approximated as a thermal gas ($p_{2,p} = \frac{2}{3}\epsilon_{2,p}$). We further assume that the protons and electrons equilibrate so that $\epsilon_{2,p} = \epsilon_{2,e}$. Hence, the hotspot pressure and enthalpy are $p_2 = \epsilon_{2,e}$ and $w_2 = \rho_2 c^2 + 3\epsilon_{2,e}$.

Conservation Equations

The equations for the conservation of energy and particles are, respectively

$$A_1\Gamma_1^2\beta_1 w_1 = A_2\Gamma_2^2\beta_2 w_2 \tag{3.18}$$

$$A_1\Gamma_1\beta_1 n_1 = A_2\Gamma_2\beta_2 n_2 \tag{3.19}$$

where A is the jet cross-sectional area. Dividing equation (3.18) by equation (3.19), we can write:

$$\Gamma_1 \frac{w_1}{\rho_1 c^2} = \Gamma_2 \frac{w_2}{\rho_2 c^2} \tag{3.20}$$

Peak Lorentz Factor

Combining equation (3.20) with our model assumptions described above we find

$$\Gamma_1 \approx \Gamma_2 \left(1 + \frac{3\epsilon_{2,e}}{\rho_2 c^2}\right) \tag{3.21}$$

$$\approx \Gamma_2 \left(1 + 3\frac{m_e}{m_p}\langle\gamma\rangle\right) \tag{3.22}$$

where we have made the substitution $\rho_2 \approx n_p m_p$ and $\epsilon_{2,e} = \langle\gamma\rangle n_e m_e c^2$.

Let us introduce the parameter $\chi \equiv \langle\gamma\rangle/\gamma_p$ which is the ratio of the mean electron Lorentz factor in the hotspot ($\langle\gamma\rangle$) to the electron Lorentz factor at the peak of the electron energy distribution (γ_p). Then

$$\gamma_p = \frac{1}{3}\frac{m_p}{m_e}\left(\frac{\Gamma_1}{\Gamma_2} - 1\right)\chi^{-1} \tag{3.23}$$

In order to estimate the parameter χ we assume that the electron distribution below γ_p can be approximated by the low energy tail of a relativistic Maxwellian,

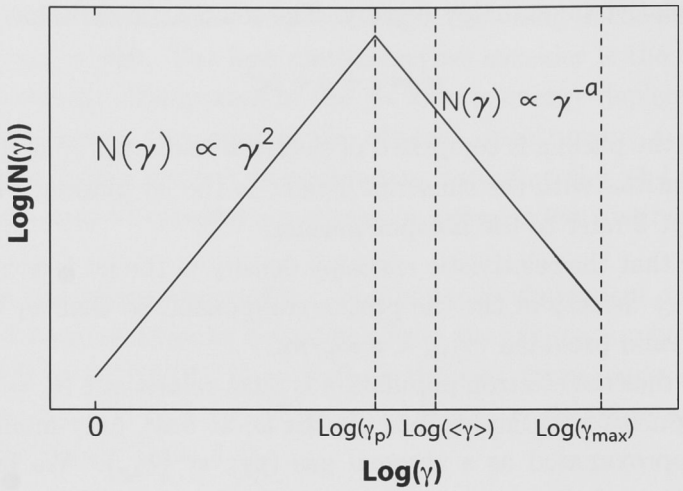

Figure 3.9: Plot of the assumed form of the electron energy distribution used to relate the mean of the distribution $\langle\gamma\rangle$ to the mode $\gamma_{\rm p}$ (see equations (3.24) and (3.25)). In §3.4.2, when modeling the hotspot spectrum, we approximated the electron energy distribution with a broken power law between $\gamma_{\rm min}$ and $\gamma_{\rm max}$, and number density set to zero outside this range. Here we assume that initially the (injected) electron spectrum is a single (un-broken) power-law between $\gamma_{\rm p}$ and $\gamma_{\rm max}$, with $N(\gamma) \propto \gamma^2$ below $\gamma_{\rm p}$. The instantaneous cutoff at $\gamma_{\rm min}$ used for spectral modeling is an approximation to the turnover in the electron energy distribution. We identify $\gamma_{\rm min}$ with the peak of the electron energy distribution, which here we define as γ_p.

and above γ_p the electron distribution (before cooling via synchrotron emission) is a power-law extending from the peak to a maximum Lorentz factor $\gamma_{\rm max}$ (see Figure 3.9).

$$N(\gamma) = \begin{cases} K_e \gamma_{\rm p}^{-(a+2)} \gamma^2 & 1 < \gamma < \gamma_{\rm p} \\ K_e \gamma^{-a} & \gamma_{\rm p} < \gamma < \gamma_{\rm max} \\ 0 & \gamma > \gamma_{\rm max} \end{cases} \tag{3.24}$$

Using this particular form for the energy distribution, the value of χ is a function of the three parameters a, γ_p and $\gamma_{\rm max}$. If $a = 2$, the ratio of mean Lorentz factor to the peak Lorentz factor reduces to the following simple algebraic form

$$\chi \approx \frac{3}{16} + \frac{3}{4} \ln\left(\frac{\gamma_{\rm max}}{\gamma_{\rm p}}\right) \tag{3.25}$$

provided $\gamma_{\rm p} >> 1$. From our analysis of the spectrum of the northern hotspot of PKS 1421–490 in §3.4.2 we have $\gamma_p \approx 650$, $\gamma_{\rm max} \approx 1.2 \times 10^5$ and $a = 2.06$ so that $\chi \approx 4$. Therefore in order to produce a turn-over in the electron energy distribution at $\gamma_{\rm min} \sim 650$ the jet must have a bulk Lorentz factor $\Gamma_1 \gtrsim 5$. This

value of jet Lorentz factor is consistent with jet Lorentz factors inferred from modeling the radio to X-ray spectra of quasar jets on kpc-scales (Tavecchio et al., 2000b; Schwartz et al., 2006; Kataoka & Stawarz, 2005). If $\Gamma_2 > 1$, or the jet contains some fraction of positron/electron pairs, or the electrons do not reach equilibrium with the protons, or we consider the effect of the magnetic field, then the energy requirements increase, and so too must Γ_1.

It was noted in §3.1 that while only a small number of hotspots have provided direct estimates of $\gamma_{\rm min}$, they are all distributed around a value of $\gamma_{\rm min} \approx 600$ to within a factor of 2 (excluding the value $\gamma_{\rm min} \sim 10^4$ indirectly estimated by Blundell et al. (2006)). The value of the parameter χ is weakly dependent on the electron spectrum, and in general should be within the range $\chi \sim 2-6$. Therefore, dissipation of bulk kinetic energy associated with relativistic proton/electron jets with bulk Lorentz factors of order $\Gamma_1 \gtrsim 5$ can provide a natural explanation for the inferred turn-overs in electron spectra at $\gamma_{\rm min} \sim 300 - 1000$.

Our analysis indicates that the value of $\gamma_{\rm min} \sim 10^4$ inferred by Blundell et al. (2006) for the hotspot of the radio galaxy 6C0905+3955 would require a jet Lorentz factor $\Gamma_{\rm jet} \gtrsim 16\chi + 1$. If $\chi \gtrsim 2$ (note that $\alpha \sim 0.7$ for this hotspot, and the synchrotron spectrum extends from radio through to soft X-ray frequencies (Erlund et al., 2008)), then the required jet Lorentz factor is $\Gamma_{\rm jet} \gtrsim 35$.

Electron/Positron Jet

Let us now consider the case of a pure electron/positron jet. In this case, assuming an ultra-relativistic equation of state in the jet and hotspot, the ratio of equations (3.18) and (3.19) implies

$$\Gamma_1 \gtrsim \frac{\langle\gamma\rangle_{2,e}}{\langle\gamma\rangle_{1,e}} \tag{3.26}$$

Uchiyama et al. (2005) estimate a mean Lorentz factor of $\langle\gamma\rangle_{1,e} \approx 50$ in the jet of PKS 0637–752. If a similar mean Lorentz factor applies to the jet of PKS 1421–490 then the required jet bulk Lorentz factor is $\Gamma_1 \gtrsim 50$.

3.8.2 Pre-Acceleration: Cyclotron Resonant Absorption?

We now consider an alternative explanation for the flattening of the electron energy distribution. The observed change in slope may be the result of a transition between two different acceleration mechanisms: a pre-acceleration process producing a relatively flat electron spectrum at low energy, and diffusive shock acceleration acting at higher energy producing an electron distribution $N(\gamma) \propto \gamma^{-a}$ with $a \sim 2$. We have not modeled the spectrum in terms of such a scenario, but this model cannot yet be ruled out.

One interesting candidate for the pre-acceleration mechanism is that described by Hoshino et al. (1992) and Amato & Arons (2006). They have shown that in a relativistic, magnetized, collisionless shock with an electron-positron-proton

plasma there can be efficient transfer of energy from protons to leptons via the resonant emission and absorption of electromagnetic waves at high harmonics of the proton cyclotron frequency. This process produces a particle distribution described by a relativistic Maxwell distribution at low energies ($\gamma < \Gamma_{\rm jet}$) and a relatively flat ($a < 2$) power-law component extending from $\sim \Gamma_{\rm jet}$ to $\sim \Gamma_{\rm jet}(m_p/m_e)$. The electron energy index of the power-law component is sensitive to the plasma composition. The theoretical maximum Lorentz factor attained via this acceleration mechanism ($\sim \Gamma_{\rm jet}(m_p/m_e)$) is set by resonance with the fundamental proton cyclotron frequency. However, the upper cutoff energy determined from the results of particle-in-cell simulations is somewhat lower than the theoretical maximum (Amato & Arons, 2006). Therefore, the observed flattening in the hotspot radio spectrum may be associated with a transition between the cyclotron resonant absorption mechanism and diffusive shock acceleration. Stawarz et al. (2007) have suggested this interpretation for the hotspot spectra in Cygnus A.

3.9 Summary

Long Baseline Array (LBA) imaging of the z=0.663 broad line radio galaxy PKS 1421–490 has revealed a compact (400 pc diameter), high surface brightness hotspot at a projected distance of approximately 40 kpc from the active galactic nucleus. The isotropic X-ray luminosity of the hotspot, $L_{2-10\,\rm keV} = 3 \times 10^{44}\,\rm ergs\,s^{-1}$, is comparable to the isotropic X-ray luminosity of the entire X-ray jet of PKS 0637–752, and the peak radio surface brightness is hundreds of times greater than that of the brightest hotspot in Cygnus A. We successfully modeled the radio to X-ray spectral energy distribution using a standard one-zone synchrotron self Compton model with a near equipartition magnetic field strength of 3 mG. There is a strong brightness asymmetry between the approaching and receding hotspots, and the hot spot spectrum remains flat ($\alpha \approx 0.5$) well beyond the predicted cooling break for a 3 mG magnetic field, indicating that the hotspot emission may be Doppler beamed. We suggest that a high plasma velocity beyond the terminal jet shock could be the result of a dynamically important magnetic field in the jet, resulting in Doppler boosted hotspot emission. However, some aspects of the hotspot morphology may argue against an interpretation involving significant Doppler beaming. LBA observations at 1.4 GHz will be required to further investigate the hotspot morphology.

There is a change in the slope of the hotspot radio spectrum at GHz frequencies. We successfully modeled this feature by incorporating a cutoff in the electron energy distribution at $\gamma_{\rm min} \sim 650$ (assuming a Doppler factor of unity). If the hotspot emission is Doppler beamed with Doppler factor δ, the low energy cutoff is $\gamma_{\rm min} \approx 650\ \delta^{1/3}$. We have made use of the equations for the conservation of energy and particles in an un-magnetised proton/electron jet to obtain a general expression that relates the peak in the hotspot electron energy distribution to the

jet bulk Lorentz factor. We have shown that a sharp decrease in electron number density below a Lorentz factor of about 650 would arise from the dissipation of bulk kinetic energy in an electron/proton jet with bulk Lorentz factor $\Gamma_{\rm jet} \gtrsim 5$. This value of jet Lorentz factor is consistent with jet Lorentz factors inferred from modeling the radio to X-ray spectra of quasar jets on kpc-scales (Tavecchio et al., 2000b; Schwartz et al., 2006; Kataoka & Stawarz, 2005). These results are of particular interest given that similar values of $\gamma_{\rm min}$ have been estimated for several other hotspots. Our analysis indicates that the value of $\gamma_{\rm min} \sim 10^4$ inferred by Blundell et al. (2006) for the hotspot of the radio galaxy 6C0905+3955 would require a jet Lorentz factor $\Gamma_{\rm jet} \gtrsim 35$.

An alternative explanation for the low frequency flattening in the radio spectrum of the northern hotspot of PKS 1421–490 may be that it is associated with the transition between a pre-acceleration mechanism, such as the cyclotron resonant process described by Hoshino et al. (1992) and Amato & Arons (2006), and diffusive shock acceleration.

Future LBA observations at 1.4GHz will help to constrain the low energy end of the electron energy distribution, and infra-red observations are required to constrain the high frequency end of the synchrotron spectrum. More sophisticated models of the electron energy distribution will be required in future studies, to test the hypothesis that the flattening in the radio spectrum is associated with a transition between two distinct acceleration mechanisms.

Chapter 4

A Multi-Wavelength Study of the Quasar Jet Source PKS 2101–490

PKS 2101-490 was first reported as a bright flat spectrum radio source by Ekers (1969). Studies at the Australia Telescope Compact Array (ATCA) later revealed significant radio emission on arcsecond scales (Lovell, 1997). For this reason, PKS 2101–490 was included in a *Chandra* survey of flat spectrum radio quasars with arcsecond scale radio jets (Marshall et al., 2005). Marshall et al. (2005) presented an 8.6 GHz ATCA image along with a 5 kilosecond snapshot *Chandra* image that revealed significant X-ray emission associated with the 13″ eastern radio jet. The authors assigned a tentative redshift of $z = 1.04$ to this object based on a spectrum obtained at the Magellan telescope. Here we present detailed physical analysis of the jet and lobes of this source based on new ATCA, *Chandra* and HST images.

4.1 Observations and Data Reduction

4.1.1 Overview

Figures 4.1 and 4.2 illustrate the radio structure of the source and the naming convention used for the various features in the radio maps. In order to study the evolution of the radio to X-ray spectral energy distribution along the jet, we have extracted radio, optical and X-ray flux densities from the seven major emission regions identified in Figure 4.2. In this section we describe the observations in each waveband, as well as the methods used to measure flux densities and sizes for the individual jet knots. Table 4.1 lists the observational information for all data used in this study.

4.1.2 Radio

PKS 2101–490 was observed with the ATCA at 4.8GHz and 8.64GHz in two configurations, 1.5A and 6A on May 25 2000 and September 2 2000 respectively, and in a

Table 4.1. Observation Information

Instrument	Waveband/Frequency	Configuration/Observing Mode	Date Observed	Resolution
ATCA	4.8 GHz	1.5A/6A	May 25/Sep 2 2000	1.″8
ATCA	8.64 GHz	1.5A/6A	May 25/Sep 2 2000	1.″25
ATCA	17.73 GHz	6C	May 10 2004	0.″54
ATCA	20.16 GHz	6C	May 10 2004	0.″47
HST	F814W	ACS/WFC	Mar 8 2005	0.″1
HST	F475W	ACS/WFC	Mar 8 2005	0.″1
Chandra	0.5 – 7 keV	ACIS-S3	Dec 17 2004	0.″8

single configuration (6C) at 17.7GHz and 20.2GHz on May 10 2004. In each case, a full 12 hour synthesis was obtained, recording 128MHz bandwidth in all four polarization products. Regular scans on the nearby phase calibrator PKS 2106–413 were scheduled throughout the observations, as well as scans on the ATCA flux calibrator PKS 1934-638. Standard calibration and editing procedures were followed using the MIRIAD data analysis package. Following calibration, the data were exported to DIFMAP and several imaging/self-calibration iterations were performed. The data were both phase and amplitude self-calibrated. The resulting Stokes I images have dynamic range (ratio of map peak to residual map rms) of order $5 \times 10^3 - 10^4$. The 17 and 20GHz maps have off-source rms close to the theoretical noise limit[1]. The lower frequency maps are dynamic range limited and have off-source rms approximately 3 - 5 times the theoretical noise limit due to difficulty in modeling the bright core at these frequencies. This may be due to the combination of two different array configurations at 8.6 and 4.8 GHz.

Flux Density Meausrements

Radio flux densities for individual knots were measured by summing the pixel values within a region encompassing the knot. Let $I_\nu^{i,j}$ be the surface brightness (in Jy/beam) at pixel (i, j), $L_{\rm pix}$ the pixel length, and $\phi_{x/y}$ the FWHM of the restoring beam in the x/y direction. Then the flux density

$$F_\nu = \sum_{\rm i,j} I_\nu^{\rm i,j} \times \frac{\text{pixel area}}{\text{effective beam area}} \tag{4.1}$$

$$= \sum_{\rm i,j} I_\nu^{\rm i,j} \times \frac{L_{\rm pix}^2}{(\pi/4\ln 2)\phi_x\phi_y} \tag{4.2}$$

In practice the pixel values within a region were summed using the "Counts in region" function of the ds9 image analysis software. Alternatively the flux density can be obtained using the interactive display in DIFMAP.

[1]Theoretical noise limit calculated using the ATCA sensitivity calculator `http://www.atnf.csiro.au/observers/docs/at_sens/` which makes use of equations given in the ATNF memo AT/01.17/025 available at `http://www.narrabri.atnf.csiro.au/observing/AT-01.17-025.pdf`

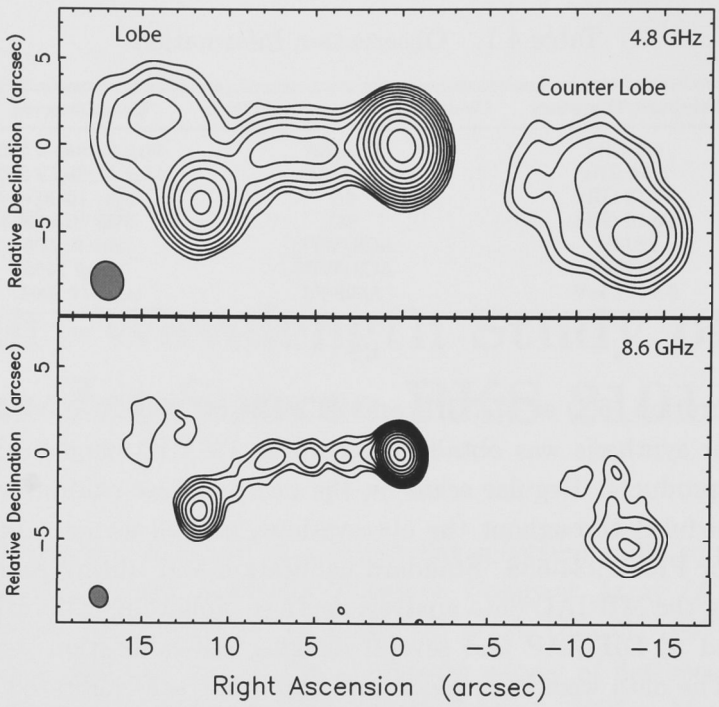

Figure 4.1: ATCA images at 4.8GHz (top) and 8.6GHz (bottom) showing large scale radio structure of PKS 2101–490. The scale of this image is 8.1 kpc/″. Contours are separated by a factor of 2 in surface brightness. 4.8GHz: Lowest contour 0.42 mJy/beam. Beam FWHM $2\farcs24 \times 1\farcs84$. 8.6GHz: Lowest contour 0.64 mJy/beam. Beam FWHM $1\farcs25 \times 1\farcs04$.

The spectrum of the entire jet (excluding lobe emission) between 4.8GHz and 20.2GHz is well described by a power-law with spectral index $\alpha = 0.81 \pm 0.01$. Each of the four flux density measurements are within 1% of the best fit power-law, giving confidence in the flux density and spectral index measurements for the entire jet. However, inspection of individual knot spectra indicate that the uncertainty in flux density measurements for individual knots is greater than the off-source RMS. The 8.6, 17.7 and 20.2GHz flux density measurements have significant scatter about a power-law fit to the three data points. In some cases the 20.2GHz flux density measurement is greater than that at 17.7GHz — suggesting significant systematic uncertainties are present in the flux density measurements for individual knots. For this reason, we are unable to accurately determine the spectral index for each individual knot, and are instead forced to assume that each knot has the same spectral index as that of the entire jet, which is accurately determined. There are a number of factors contributing to the systematic uncertainty in the radio flux density measurements, which we now discuss.

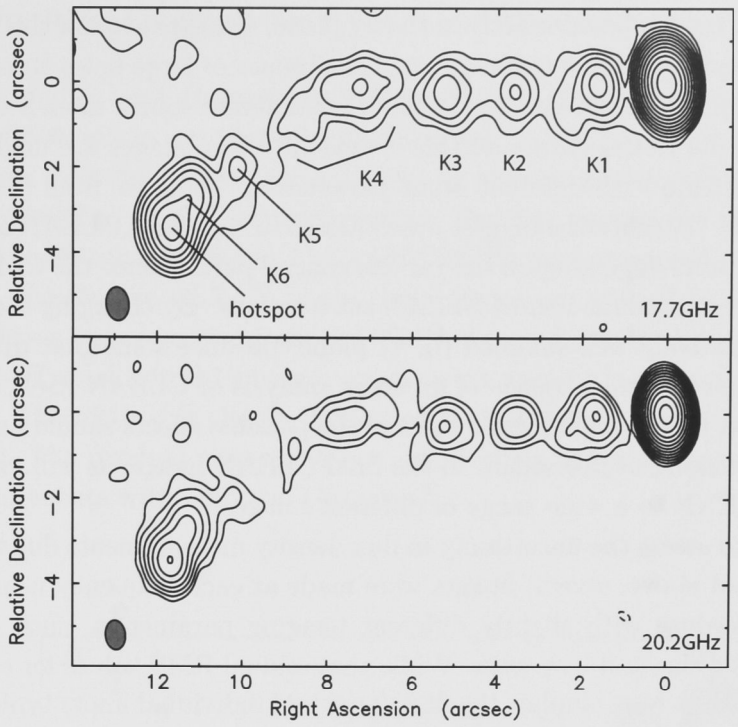

Figure 4.2: ATCA images at 17.7GHz (top) and 20.2GHz (bottom) showing structure of the jet of PKS 2101–490. Also shown is the naming convention used for various components of the jet. The scale of this image is 8.1 kpc/″. Contours are separated by a factor of 2 in surface brightness. 17.7GHz: Lowest contour 0.15 mJy/beam. Beam FWHM $0\farcs79 \times 0\farcs54$. 20.2GHz: Lowest contour 0.17 mJy/beam. Beam FWHM $0\farcs7 \times 0\farcs47$. In each case, the lowest contour is 3 times the residual map rms.

Systematic Errors Affecting Radio Spectral Index Measurements

The flux density of the individual knots is less than 1% of the core flux density. While it is possible to push the dynamic range towards 10^4 using a careful self-calibration and imaging procedure, the accuracy of the resulting map may not be as high as suggested by such high dynamic range, particularly in regions of low signal-to-noise. This is a well known problem in radio astronomy, and is commonly referred to as the "uniqueness problem". To quote from Zensus et al. (1995, chap. 8) "[The uniqueness problem] is the result of incomplete (u, v) coverage. It is easily seen when studies are made of the imaging capabilities of various array configurations using fake data based on a source of known structure. When images of such data are subtracted from the input image, the errors are strongly concentrated in the regions where there is emission. It is clear that the offsource noise level is not a good indication of errors in the relative strength of regions with emission. This is simply an effect of the inability of the imaging

algorithms to interpolate perfectly in the uv plane. The presence of this effect is the reason why dense uv plane coverage and the absence of large holes is so desirable." The uniqueness problem refers to the fact that different source models can produce equally good fits to the data, and this is evident when images are made using the CLEAN algorithm with different input parameters. To quote from (Taylor et al., 1999, chap. 8) "Perhaps the biggest drawback to to the use of CLEAN is the way in which the answers depend upon the various control parameters: the CLEAN boxes, the loop gain and the number of CLEAN subtractions. By changing these one can, even for a relatively well sampled (u, v) plane, produce somewhat different final CLEAN images. In the absence of an error analysis of CLEAN itself, one can do nothing about this problem. Awareness of the possible effects should however keep you from becoming overconfident in the final CLEAN image, as will experience of applying CLEAN to a wide range of different images."

In order to assess the uncertainty in flux density measurements due to the problems described above, several images were made at each frequency using the same imaging procedure with slightly different imaging parameters, such as CLEAN windows, pixel size and loop gain. While the residual RMS values for each map at a given frequency were similar, the flux density of individual knots typically varied by 5 - 10% between images.

Another source of systematic error in flux density measurements for individual knots is due to the different (u, v) coverage at each frequency. Inter-knot emission is picked up to varying degrees by the different arrays, and this inter-knot emission contributes varying amounts to the knot flux densities at different frequencies. Finally, some of the knots at 8.6GHz are only marginally resolved.

We estimate the uncertainty in individual knot flux density measurements to be 10%. This uncertainty in flux density measurements results in an uncertainty in spectral index of $\Delta\alpha \gtrsim 0.1$.

The flux density measurements for the entire jet do not suffer from the same systematic errors as the measurement of flux density for individual knots, largely due to the greater signal to noise ratio and the fact that the measurements of the total jet flux density are not greatly affected by the uniqueness problem. The uniqueness problem refers to the relative flux densities of individual components of an image. The CLEAN algorithm will account for all the flux in an image, though the components may have different relative flux densities depending on the imaging strategy. As discussed above, the jet flux at each frequency (4.8, 8.6, 17.7 and 20.2GHz), regardless of flux extraction region and imaging parameters, were consistently found to lie within 1% of a power law fit with spectral index $\alpha = 0.81$. This is the same spectral index as the jet of PKS 0637–752 (Schwartz et al., 2000).

Flux Density Measurements for Knot 6 and the Hotspot

There is a strong jet knot approximately 0.″9 upstream from the terminal hotspot. These two bright regions are partially blended even at 20GHz, and it is not possible to measure their flux densities accurately by summing pixel values and using the method described in the previous section. For this reason, the flux densities and sizes of the hotspot and K6 at 17.7 and 20.2GHz were measured in the following manner: Firstly, the CLEAN components associated with the emission from these two regions were removed from the CLEAN model, leaving two peaks in the residual map. Two elliptical Gaussian components were fit to the residuals in the (u, v)-plane. The method is clearly illustrated by the "before" and "after" images of Figure 4.3. The residual maps were not significantly degraded by replacing the CLEAN components with elliptical Gaussians.

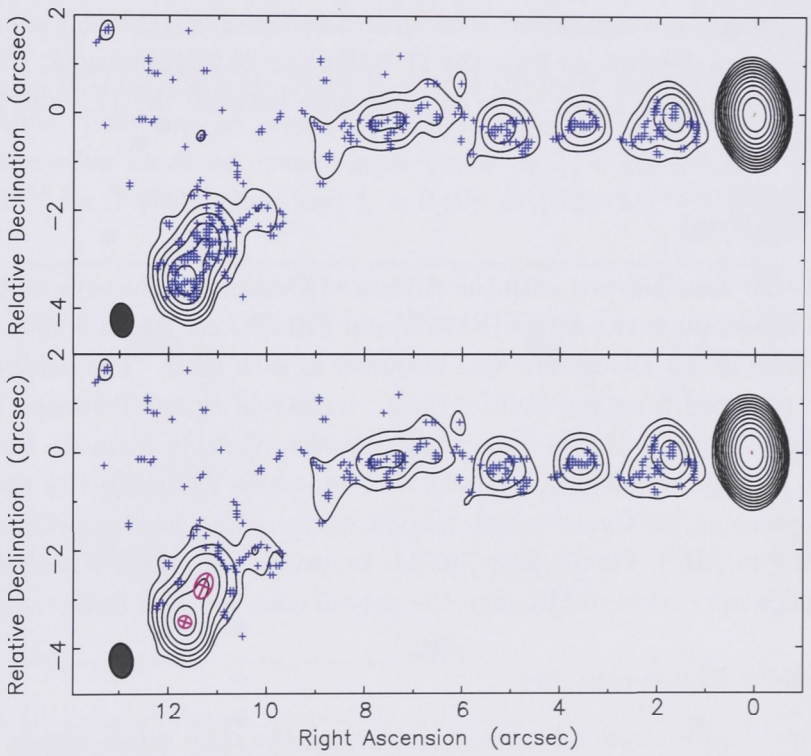

Figure 4.3: Top: PKS 2101–490 ATCA 20GHz image showing the CLEAN model. Bottom: PKS 2101–490 ATCA 20GHz image showing the modified CLEAN model, with elliptical gaussian model fits to knot 6 and the hotspot.

Size Measurements

The knot volume is a required input to the IC/CMB model. With the new 15mm ATCA images, the individual radio knots are resolved and it is possible to constrain the knot volume. The jet radius is a particularly important parameter to constrain, since the jet power scales as jet radius squared.

Knot sizes (for K1 - K4) were measured by fitting 2D Gaussian models to jet knots using the AIPS task JMFIT. Knot volumes were calculated by approximating each knot as a cylinder. For each knot, the length and diameter of the cylinder were equated with the FWHM of the Gaussian component along the major and minor axes respectively. Both the 17.7GHz and 20.2GHz images were used to measure knot sizes.

The size estimates from the 17.7GHz and 20.2GHz images were consistent for some knots. However, in some cases the knot dimensions differed by as much as a factor of 2. This is another indication that image fidelity is questionable in the high frequency maps, and systematic errors resulting from the deconvolution/self-calibration process are significant. The knot sizes listed in Table 4.3 are averages of the parameters determined from the 17.7GHz and 20.2GHz images. The uncertainties in knot size are taken to be the difference between the 17.7 and 20.2GHz measurements.

4.1.3 Optical

PKS 2101–490 was observed with the Advanced Camera for Surveys on the Hubble Space Telescope in two filters (F475W and F814W) on March 8 2005. A total exposure time of 2.3 kiloseconds was obtained in each filter. The calibrated images were retrieved from the Multi-mission Archive at Space Telescope (MAST) website[2] and aligned with the radio images in the following manner: Firstly, the radio core position was found by fitting a point source component to the core in the (u, v)-plane. A 2D Gaussian was then fit to the optical core position using the task JMFIT in AIPS. Finally, the CRVAL keywords in the FITS header of each optical image were corrected to align the optical core with the radio core.

Flux Density Measurements

Optical flux densities were measured by summing the pixel values within an aperture encompassing the region of interest. Let $f_\nu(P)$ be the mean flux density (Jy) in the bandpass P, x_s the source count rate (electrons per second) within the aperture, U(P) the inverse sensitivity in units of ergs s^{-1} $Å^{-1}$ $electrons^{-1}$ (listed as the PHOTFLAM keyword in the FITS header), λ_p the pivot wavelength in units of Å(listed as the PHOTPLAM keyword in the FITS header), c the speed of light in units of $Ås^{-1}$, EE the encircled energy for the given aperture size and A(P) the

[2]HST archive `http://archive.stsci.edu/`

extinction correction in magnitudes for the passband in question. Calculations of flux density were performed as follows

$$f_\nu(P) = 10^{23} \times U(p)\, x_s\, \frac{\lambda_p^2}{c} \left(\frac{1}{EE}\right) 10^{0.4\,A(P)}\ \mathrm{Jy} \tag{4.3}$$

(Sirianni et al., 2005, section 7.2). The leading factor 10^{23} is the conversion factor from ergs s^{-1} cm^{-2} Hz^{-1} to Jy. The appropriate aperture corrections were taken from Sirianni et al. (2005) Table 3, and the appropriate extinction corrections were taken from Sirianni et al. (2005) Table 14 assuming E(B-V) = 0.039 at the position of PKS 2101–490. This value for E(B-V) was obtained using the NASA Extragalactic Database extinction calculator[3]. The background was subtracted by calculating the mean ($\bar{x}_b$) and rms (σ_b) of 1000 background pixels near the jet. The background count rate (x_b) in an aperture encompassing N pixels can then be estimated as $x_b = N\bar{x}_b \pm \sigma_b$. The source count rate was calculated as follows

$$x_s = (x_{tot} - N\bar{x}_b) \pm \sqrt{\sigma_b^2 + \sigma_{poisson}^2} \tag{4.4}$$

where $\sigma_{poisson} = \sqrt{x_{tot}/\Delta t}$ is the Poisson error in the total count rate, and Δt is the exposure time. Only one jet knot (K6) was detected in the HST images (Figure 4.4). For the other knots we obtain upper limits via $x_s < 3\sigma_b$ giving $f_\nu < 2.5$ nJy at 6.32×10^{14} Hz (F475W filter) and $f_\nu < 3$ nJy at 3.72×10^{14} Hz (F814W filter).

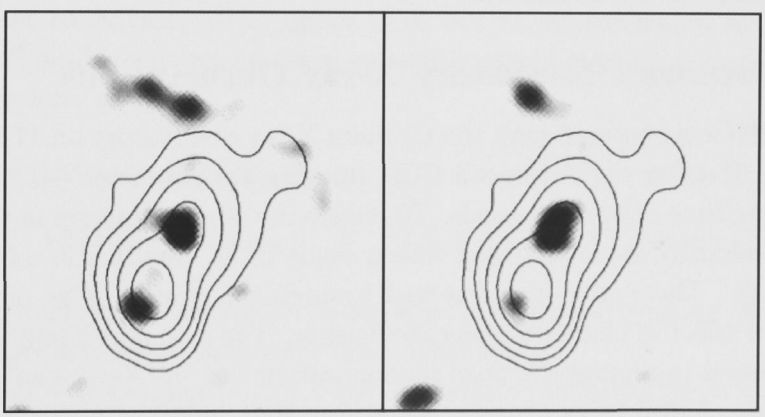

Figure 4.4: Optical images smoothed with 0.″5 Gaussian and heavily biased greyscale to emphasize low level optical emission. ATCA 20GHz contours are overlaid. Left: F814W. Right: F475W. Knot 6 is clearly detected in both filters. The emission near the tip of the hotspot has spectral index $\alpha_o = -0.3 \pm 0.7$ which is inconsistent with the radio spectral index $\alpha_r \approx 0.8$. This emission is therefore associated with a foreground object.

[3]NASA Extragalactic Database extinction calculator
`http://nedwww.ipac.caltech.edu/forms/calculator.html`

Table 4.2. Positions and sizes of optical knots

Object	Filter	(RA, Dec)	Major Axis	Minor Axis	Position Angle
Star	F475W	(21:05:01.792, -48:48:57.82)	0.″14	0.″12	128°
Star	F814W	(21:05:01.793, -48:48:57.81)	0.″15	0.″13	110°
α_o	4.9 ± 0.1				
Core	F475W	(21:05:01.1545, -48:48:46.485)	0.″14	0.″1	152°
Core	F814W	(21:05:01.1545, -48:48:46.485)	0.″22	0.″18	164°
α_o	0.6 ± 0.2				
K6	F475W	(21:05:02.296, -48:48:49.27)	$0.''3 \pm 0.''2$	$0.''25 \pm 0.''15$	$170° \pm 80°$
K6	F814W	(21:05:02.303, -48:48:49.203)	$0.''42 \pm 0.''02$	$0.''14 \pm 0.''02$	$93° \pm 1°$
α_o	1.3 ± 0.3				

Size Measurements

Elliptical Gaussian models were fit to the optical images of knot 6, the core and a nearby star using the AIPS task JMFIT. The positions and sizes of the Gaussian models are given in Table 4.2. The quoted sizes are the major and minor axes of the Gaussian fits to the data. The true knot size must be corrected for the PSF: $\mathrm{FWHM_{true}} = \sqrt{\mathrm{FWHM^2_{obs}} - \mathrm{FWHM^2_{PSF}}}$. Due to the low signal to noise ratio in these data, it is difficult to obtain a precise estimate of the optical knot size. However, it is clear that the optical emission from knot 6 is significantly smaller than the associated radio emission.

4.1.4 Chandra Observatory X-ray Observations

PKS 2101–490 was observed with the *Chandra* X-ray observatory on 17 December 2004 (Cycle 6) using the Advanced CCD Imaging Spectrometer (ACIS-S) for a total exposure time of 42 kiloseconds. To reduce the effect of pile-up in the quasar core, a 1/4 subarray mode was used with a single CCD, resulting in a frame time of 0.8 seconds. The source was observed towards the readout edge of the CCD to reduce the effect of charge transfer inefficiency. The standard Event 2 data file was re-processed to remove the pixel randomization and the X-ray and radio core positions were aligned using a similar method to that described above for aligning the optical and radio images. The data were restricted to the energy range 0.5 - 7keV. In this energy range, the X-ray background is relatively low and the ACIS calibration is most precise.

X-ray Flux Density Measurements

There are too few counts in the jet to allow spectral fitting to individual knots. Therefore, the X-ray flux densities for individual knots were calculated by summing the counts within an aperture encompassing the knot. Let G be the inverse sensitivity in Jy/counts, x_{tot} the total counts associated with a particular region of

the source, N the number of pixels within the extraction region and $\bar{x}_b$ the average background count rate in counts/pixel. The flux densities were obtained using the following formula:

$$F_{1keV} = G\,(x_{tot} - N\bar{x}_b)\ \text{Jy} \tag{4.5}$$

The background count rate was calculated using several regions near the source.

The inverse sensitivity was estimated using the PIMMS *Chandra* proposal planning toolkit for *Chandra* Cycle 6[4]. For a galactic neutral hydrogen column density fixed at 3.4×10^{20} cm^{-2} (as determined from the COLDEN column density calculator[5] provided by the *Chandra* X-ray Center, using data from Dickey & Lockman (1990)) and source spectral index of $\alpha = 0.5, 0.8, 1.0, 1.5$ the inverse sensitivity is $G = 0.88, 0.99, 1.05, 1.15\,\mu$Jy/count/s respectively. The inverse sensitivity was verified using the spectrum of the entire jet (see below).

The uncertainties on individual flux density measurements were calculated as follows:

$$\frac{\Delta F_{1\text{keV}}}{F_{1\text{keV}}} = \sqrt{\left(\frac{\Delta G}{G}\right)^2 + \left(\frac{\Delta(x_{\text{tot}} - N\bar{x}_b)}{x_{\text{tot}} - N\bar{x}_b}\right)^2} \tag{4.6}$$

$$\tag{4.7}$$

When dealing with Poisson distributed data with only a small number of events, the lower and upper confidence levels are not equal. For n observed events, the 1σ equivalent confidence (84%) upper limit can be approximated by $\Delta n_{upper} \approx 1+\sqrt{n+0.75}$ while the lower limit can be approximated by $\Delta n_{lower} \approx \sqrt{n}$ (Gehrels, 1986). Therefore, we use

$$(\Delta(x_{\text{tot}} - N\bar{x}_b)_{\text{upper}})^2 = \left(1 + \sqrt{x_{\text{tot}} + 0.75}\right)^2 + N\bar{x}_b \tag{4.8}$$

$$(\Delta(x_{\text{tot}} - N\bar{x}_b)_{\text{lower}})^2 = \left(1 + \sqrt{N\bar{x}_b + 0.75}\right)^2 + x_{tot} \tag{4.9}$$

In practice, rounding uncertainties to one significant figure obscures this difference between upper and lower confidence limit calculations.

Figure 4.5(a) is a comparison of X-ray and radio structure in the jet of PKS 2101–490. Figure 4.5(b) illustrates the regions used to extract X-ray counts for the knots. In an ideal situation, the extraction regions should be large enough to encompass all the emission from a given jet knot, but small enough that the background and emission from nearby jet regions do not affect the results. In the case of PKS 2101–490, the knots are only marginally resolved in the *Chandra* image, and assigning counts to a given region is difficult. This is especially the case with the outer part of the jet — knots 5, 6 and the hotspot. The regions shown in Figure 4.5(b)

[4] *Chandra* proposal toolkit available at `http://cxc.harvard.edu/toolkit/pimms.jsp`

[5] COLDEN column density calculator available at `http://cxc.harvard.edu/toolkit/colden.jsp`

(except for the hotspot extraction region — this region is discussed further below) have sides $\gtrsim 1\farcs6$. The *Chandra* PSF is a strong function of photon energy, and the encircled energy fraction is therefore a function of spectral index. The quasar core has a similar spectral index to the jet, and therefore provides a useful test for the encircled energy within the flux extraction regions used in this analysis. The counts fraction for the core within a box of side $1\farcs6 \times 1\farcs6$ is $\sim 85\%$. The flux extraction regions are therefore large enough that the aperture corrections are small relative to the Poisson errors, and aperture corrections are therefore neglected entirely for the jet knots.

In order to estimate the counts associated with the hotspot and avoid contamination from knot 6, a region encompassing only one side of the hotspot is used (the side furthest from knot 6). An aperture correction of 2 is used when calculating the flux density for this region. However, it should be noted that due to the background in the vicinity of the hotspot and the possibility of contamination from knot 6, the few counts within this aperture may not be associated with the hotspot, and therefore the flux density estimate for the hotspot is an upper limit.

In the *Chandra* image, knot 1 is blended with the wings of the X-ray core, so that a precise estimate of X-ray flux density is not possible. To place a limit on the X-ray flux density from knot 1, a "Panda region" centered on the core was used, as shown in Figure 4.5(b). The background was estimated using the section of the annulus excluding knot 1. The count rate within the section of the annulus including knot 1 was not greater than the count rate within the rest of the annulus. The data are therefore consistent with zero counts from knot 1. Close inspection of the core plus jet profile in the X direction support the upper limit on X-ray flux density estimated using the Panda region.

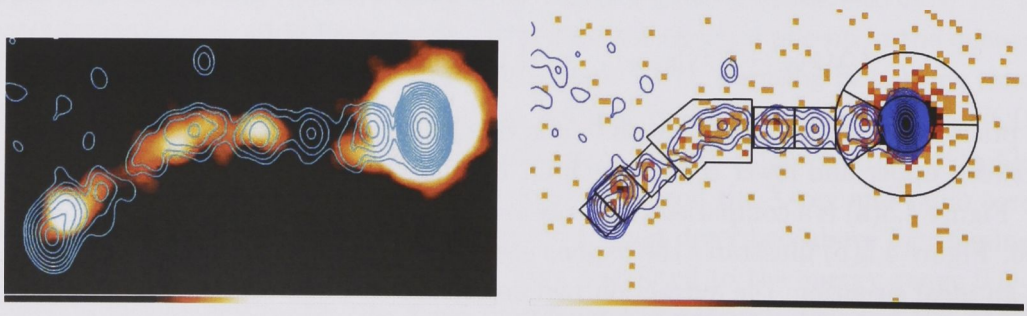

(a) (b)

Figure 4.5: (a) X-ray image binned to $0\farcs0492$ pixels and smoothed with an $0\farcs7$ Gaussian with 17.7GHz ATCA contours overlaid. (b) Raw X-ray counts image binned to half a *Chandra* pixel width ($0\farcs246$) with 17.7GHz radio contours overlaid. The black boxes mark the flux extraction regions used to calculate X-ray flux densities associated with individual knots.

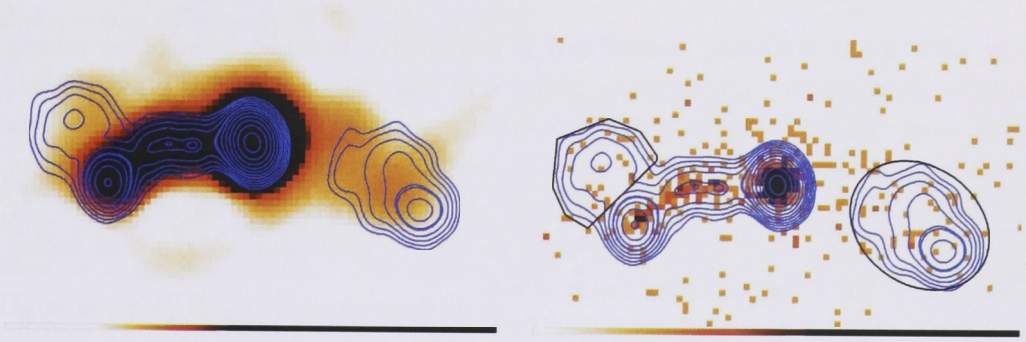

(a) (b)

Figure 4.6: (a) X-ray image binned to 0.″246 pixels and smoothed with 0.″7 Gaussian. Blue contours are from the 4.8GHz ATCA image. (b) Raw X-ray counts image with 4.8GHz radio contours overlaid. The black boxes mark the flux extraction regions used to calculate X-ray flux densities associated with the lobes.

Jet and Lobe X-ray Spectra: Verifying the Inverse Sensitivity

In order to compare the X-ray spectral index of the whole jet and lobe with the radio spectral indices, absorbed power-law model spectra were fit to the observed jet and lobe spectra. In doing so, we were able to verify the inverse sensitivity estimated using the PIMMS proposal planning toolkit.

The X-ray spectra of the jet and lobe were fit using the Sherpa software package by minimizing the Cash statistic (Log Likelihood). The instrument response functions (RMF and ARF) were determined from the CALDB calibration database appropriate for the position of the source on the ACIS-S3 chip. For the whole eastern jet of PKS 2101–490 we extracted a total of 138 counts having energies in the range 0.5keV to 7.0keV. Fitting an absorbed power law to the spectrum (with neutral Hydrogen column density fixed at 3.4×10^{20} cm^{-2}) gives flux density $F_{1keV} = 3.3 \pm 0.4$ nJy and spectral index $\alpha_X = 0.85 \pm 0.2$. The inverse sensitivity for the jet is therefore $G_{\rm jet} = 1.0 \pm 0.1$ μJy/Count/s — consistent with the prediction of the *Chandra* proposal toolkit.

In the counter lobe we extracted a total of 55 counts in the energy range 0.5keV to 7.0keV. Following the same procedure as for the jet, we find flux density $F_{1keV} = 1.5 \pm 0.2$ nJy and spectral index $\alpha = 1.3 \pm 0.3$ for the counter lobe. The inverse sensitivity for the counter-lobe is therefore $G_{\rm lobe} = 1.2 \pm 0.2$ μJy/count/s — again, consistent with the prediction from the *Chandra* proposers toolkit.

The uncertainties for the spectral index and flux density were calculated using the "covariance" routine in Sherpa. The results of this routine are valid provided the surface of Log Likelihood is approximately shaped like a paraboloid. The "Interval-Projection" routine in Sherpa was used to verify that this condition is met.

X-ray Knot Sizes

Only knot 6 has sufficient counts and is sufficiently isolated from other strong knots to allow an accurate estimate of the knot size. Using the CIAO task dmlist, events were extracted from a 0.″8 radius circular aperture centered on knot 6. This region was chosen to be large enough to include a large fraction of the counts from knot 6, but small enough to avoid contamination from neighbouring regions of the jet. Note that the encircled energy fraction within a circular aperture of radius 0.″8 is $\gtrsim 85\%$ for a spectral index of $\alpha \sim 0.8$.

A total of 29 events were extracted from knot 6. The physical (X, Y) coordinates of the individual events were rotated to a new coordinate system (X', Y') with the X′ axis aligned with the jet at knot 6. We assume, for simplicity, that the knot surface brightness profile and the inner 0.″8 of the *Chandra* PSF are both approximately Gaussian with variances $\sigma^2_{\rm source}$ and $\sigma^2_{\rm PSF,\,0.''8}$ respectively. We can then assume that the event coordinates have been sampled from a Gaussian distribution with variance $\sigma^2_{\rm obs} = \sigma^2_{\rm PSF,\,0.''8} + \sigma^2_{\rm source}$. The standard deviation of this distribution ($\sigma_{\rm obs}$) is measured using the standard deviation of the event coordinates, $s_{\rm obs}$, where

$$s_{\rm obs} = \sqrt{\Sigma_{i=1}^{N} \left(X_i' - \mu\right)^2 / N} \tag{4.10}$$

N is the number of events, and μ is the mean of the distribution.

The *Chandra* PSF is not exactly Gaussian shaped, hence the variance of the *Chandra* PSF depends on the radius of the extraction region. As mentioned above, we are forced to use a relatively small aperture because using a larger aperture results in an overestimate of the size of knot 6 due to the inclusion of events associated with knot 5. We estimate the variance ($\sigma^2_{\rm PSF,\,0.''8}$) of the *Chandra* PSF within an 0.″8 radius aperture by extracting events within an 0.″8 circular aperture centered on the core, and calculating the standard deviation of event coordinates. This comparison between core and jet PSF is valid since the core and jet X-ray spectral indices are similar, and the core is not significantly affected by pile-up.

I find $s_{\rm obs} = 0.''27$ in the jet direction, $s_{\rm obs} = 0.''29$ in the cross jet direction, and $s_{\rm PSF,\,0.''8} = 0.''29 \pm 0.''1$. Hence knot 6 is unresolved.

The background within the 0.″8 aperture is predicted to be less than one count. However, there may exist one or two counts within the aperture that are sampled from a uniform background. To quantify the likely magnitude of the effect of the background, we randomly selected either 1 or 2 events and removed these from the event list before re-calculating $s_{\rm obs}$. The distribution of these hypothetical background subtracted $s_{\rm obs}$ gave an estimate of the likely magnitude of the effect of background photons on the measured standard deviation. The removal of a single event resulted in an change $\Delta s_{\rm obs} < 0.''006$ 95% of the time, and the removal of two events resulted in a change $\Delta s_{\rm obs} < 0.''01$ 95% of the time. We therefore conclude that background photons, if present, have little effect on the significance of the upper limit calculated below.

To obtain an upper limit to the size of knot 6 we use the standard deviation distribution (Kennedy & Keeping, 1951)[6]

$$P(s;\sigma) = 2\left(\frac{N}{2\sigma^2}\right)^{(N-1)/2} e^{-Ns^2/(2\sigma^2)} s^{N-2}/\Gamma[(N-1)/2] \tag{4.11}$$

and integrate from $s_{\rm obs}$ to ∞ for a various values of σ. The 99% confidence upper limit on $\sigma_{\rm obs}$ is obtained when the integral $\int_{s_{\rm obs}}^{\infty} P(s;\sigma)ds = 0.99$. The 99% upper limit is $\sigma_{\rm obs,\,upper} = 0\farcs4$. The upper limit to the size of knot 6 (taken as the Gaussian FWHM) is then calculated as

$$\begin{aligned} \phi_{k6} &< 2\sqrt{2ln2}\sqrt{\sigma^2_{\rm obs,\,upper} - \sigma^2_{\rm PSF,\,0\farcs8}} && (4.12)\\ &< 0\farcs6 && (4.13) \end{aligned}$$

in both the jet and cross jet directions. This result is of great interest — it clearly indicates that the X-ray emission is no more extended than the radio emission for this knot, which has strong implications for models of the jet knot and the X-ray emission mechanism, as discussed in §1.4.1.

[6]See http://mathworld.wolfram.com/StandardDeviationDistribution.html

Table 4.3. Characteristics of Spatially Resolved Jet Knots and Lobes

Knot ID	Flux Densities							Guassian Fit Parameters			
	$F_{4.8\,GHz}$ mJy	$F_{8.6\,GHz}$ mJy	$F_{17.7\,GHz}$ mJy	$F_{20.2\,GHz}$ mJy	$F_{3.72\times10^{14}\,Hz}$ nJy	$F_{6.32\times10^{14}\,Hz}$ nJy	$F_{1\,keV}$ nJy	ϕ_{Maj} mas	ϕ_{Min} mas	P.A. degrees	Vol cm^3
Knot 1	—	—	5.1 ± 0.5	4.7 ± 0.5	< 3	< 3	< 0.2	400 ± 100	250 ± 10	$90° \pm 15°$	3×10^{65}
Knot 2	—	4.6 ± 0.5	2.3 ± 0.2	2.2 ± 0.2	< 3	< 3	< 0.15	400 ± 100	<150	$90° \pm 5°$	1×10^{65}
Knot 3	—	5.1 ± 0.5	3.5 ± 0.3	2.8 ± 0.3	< 3	< 3	0.5 ± 0.15	550 ± 100	330 ± 100	$110° \pm 10°$	7×10^{65}
Knot 4	—	9 ± 1	4.7 ± 0.5	4.2 ± 0.4	< 3	< 3	1.3 ± 0.3	2500 ± 500	300 ± 50	$103° \pm 1°$	3×10^{66}
Knot 5	—	—	1.0 ± 0.2	0.8 ± 0.2	< 3	< 3	0.2 ± 0.1	400 ± 100	300 ± 100	$120° \pm 20°$	4×10^{65}
Knot 6	—	11 ± 1	6.5 ± 0.6	6.3 ± 0.6	180 ± 20	90 ± 10	0.75 ± 0.2	600 ± 50	400 ± 20	$140° \pm 10°$	1×10^{66}
hotspot	—	30 ± 3	16 ± 1.5	14 ± 1.5	< 3	< 3	< 0.16	340 ± 30	240 ± 20	$55° \pm 15°$	2×10^{65}
Lobe	16 ± 2	8 ± 1	4.5 ± 0.4	4 ± 0.4	< 3	< 3	0.5 ± 0.2	6000	4700		9×10^{69}
Counter-Lobe	65 ± 6	33 ± 3	17 ± 2	14 ± 1	< 3	< 3	1.5 ± 0.2	4300	3200		3×10^{69}

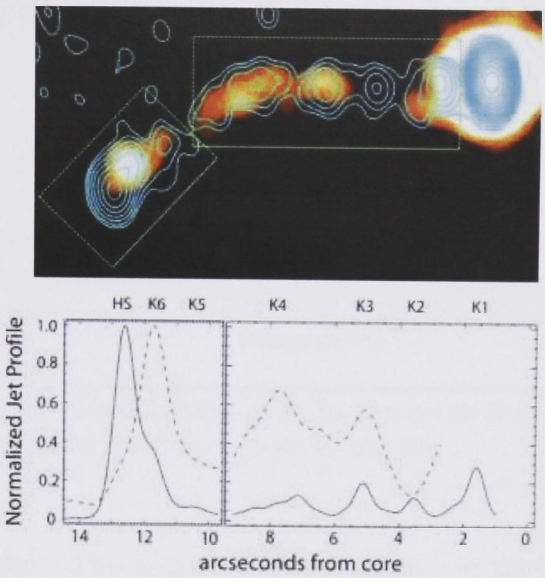

Figure 4.7: Top: X-ray image binned with 1/10 *Chandra* pixel width (0.″0492) and smoothed with a 0.″8 FWHM Gaussian to emphasize the X-ray jet structure. The resolution of the resulting image is approximately 1.″1. 17.7GHz ATCA contours are overlaid. Also shown are the projection regions used to obtain the radio and X-ray jet profiles. Jet emission is integrated along the axis perpendicular to the jet direction within the rectangles shown in this image to produce the longitudinal jet profiles. Bottom: X-ray and radio longitudinal jet profiles. Note that the X-ray resolution (approximately 1.″1) and radio resolution (approximately 0.″65) are not equal. However, these profiles serve to illustrate the differences in jet structure at each wavelength.

4.2 Results

In this section we present a comparison of the radio and X-ray images; we describe the methods used to model the radio to X-ray SEDs of individual knots; and we present the results of spectral modeling.

4.2.1 Radio/X-ray longitudinal jet profiles

Figure 4.7 illustrates the radio and X-ray longitudinal jet profiles. It can be seen that the X-ray surface brightness increases with distance from the core. This trend is opposite to that which is often observed in quasar jet sources (eg. Jorstad & Marscher, 2004; Georganopoulos & Kazanas, 2004, and references therein).

4.2.2 Modeling the Spectral Energy Distributions of Spatially Seperated Knots

The spectral energy distributions of the jet knots are typical of quasar jets such as PKS 0637–752 (see Figure 4.8). It is clear that a single power-law is unable to fit the entire radio to X-ray SED. The X-ray spectral index of the entire jet $\alpha_{0.5\,\mathrm{keV}}^{7.0\,\mathrm{keV}} = 0.85 \pm 0.2$ is consistent with the radio spectral index of the entire jet $\alpha_R = 0.81 \pm 0.01$, and the data are therefore consistent with an inverse Compton interpretation for the X-ray emission.

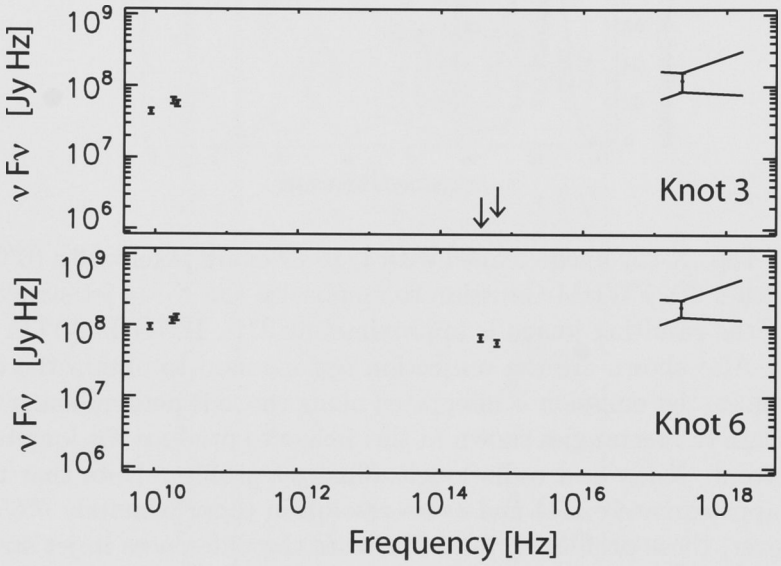

Figure 4.8: Spectral energy distributions for knots 3 and 6. These figures serve to illustrate that the general shape of the SEDs are similar to those observed in other quasar jets. The solid lines around the X-ray data point illustrate the 1σ range of allowed X-ray spectral slopes determined by fitting the counts spectrum of the entire jet.

SSC Modeling

We first attempt to model the knot SEDs in terms of synchrotron self Compton emission from a mildly-relativistic jet with $\delta \approx 1$. An example fit to the multi-wavelength data for one of the knots is shown in Figure 4.9. The synchrotron spectrum is not well constrained. We assume the electron energy distribution is a single power-law with energy index $a = 2.6$ and high energy cutoff at $\gamma_{\mathrm{min}} = 10^5$. The low energy cutoff γ_{min} is constrained by the HST optical upper limits.

The results of the synchrotron self Compton fits for each knot are given in Table 4.4. These results indicate that if the X-ray emission is produced purely via the SSC mechanisms, then the jet plasma must be particle dominated and

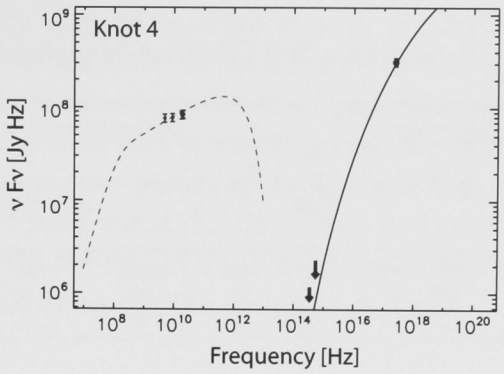

Figure 4.9: Synchrotron self Compton fit to the spectral energy distribution of knot 4. The parameters of the fit are given in the text.

far from equipartition. The magnetic field strengths in the knots derived from synchrotron self Compton modeling are a factor of ~50 below the equipartition (minimum energy) values. If the jet is Doppler beamed, the difference between the two magnetic field estimates increases.

The electron energy distribution must be truncated at a Lorentz factor $\gamma_{\rm min} > 5 \times 10^3$, otherwise the SSC emission from low energy particles lies above the optical upper limits. It should also be noted that the model X-ray spectral index is $\alpha_{0.5\,\rm keV}^{7.0\,\rm keV} \approx 0.6$ if $\gamma_{\rm min} = 5 \times 10^3$ and is lower if $\gamma_{\rm min}$ is higher. The model X-ray spectral index is relatively low as a result of the high value of $\gamma_{\rm min}$. The model X-ray spectral index is inconsistent with the X-ray spectral index of the entire jet $\alpha_{0.5\,\rm keV}^{7.0\,\rm keV} = 0.85 \pm 0.2$. We do not consider the one-zone SSC model any further.

IC/CMB Modeling

We next attempt to model the knot X-ray emission in terms inverse Compton scattering of CMB photons in a highly relativistic jet directed close to the line of sight.

Assumed form of the electron energy distribution: In order to apply the analytic one-zone IC/CMB model equations, we must assume a single power-law electron energy distribution $N(\gamma) = K_e \gamma^{-a}$ between some minimum and maximum Lorentz factor, $\gamma_{\rm min}$ and $\gamma_{\rm max}$. The X-ray spectral index and radio spectral index of the entire jet are 0.85 ± 0.2 and 0.81 ± 0.01 respectively. We therefore assume $a = 2.6$. It remains only to specify values for $\gamma_{\rm min}$ and $\gamma_{\rm max}$.

As is the case for other IC/CMB candidates (eg. Tavecchio et al., 2000b), the optical upper limits constrain the low energy cutoff in the electron spectrum. This constraint is possible because an extrapolation of the IC/CMB spectrum from X-ray to optical frequencies lies above the optical upper limits. The IC/CMB spec-

Table 4.4. Synchrotron Self Compton Modeling Results

	Fixed Parameters		Derived Parameters				
Knot ID	α	$\gamma_{\rm max}$	B $[\mu G]$	$\frac{B_{\rm eq}}{B}$	$\gamma_{\rm min}$	n_e $[\times 10^{-6}$ cm$^{-3}]$	$L_{\rm jet}^{\Gamma=2}$ [ergs/s]
Knot 3	0.8	10^5	3.2	40	> 3800	11	10^{48}
Knot 4	0.8	10^5	1.5	60	> 5500	6	5×10^{47}
Knot 6	0.8	10^5	3.2	35	> 4300	5	5×10^{47}

trum must therefore cutoff at a frequency above the HST observing frequencies. Let β_j be the jet velocity as a fraction of the speed of light, θ_j be the angle between the jet and the line of sight in the lab frame, and let θ'_j be the corresponding angle in the jet frame, such that

$$\cos\theta'_j = \frac{\cos\theta_j - \beta_j}{(1 - \beta_j \cos\theta_j)} \tag{4.14}$$

The electron energy responsible for IC/CMB emission observed at frequency $\nu_{\rm IC}$ is (Harris & Krawczynski, 2002)

$$\gamma = \frac{6.25 \times 10^{-12} \nu_{\rm IC}}{\left(1 + \cos\theta'_j\right) \delta\Gamma} \tag{4.15}$$

For relevant values of the parameters θ_j ($2^\circ \lesssim \theta_j \lesssim 10^\circ$) and Γ ($5 \lesssim \Gamma \lesssim 10$), and applying the constraint 6.32×10^{14} Hz $< \nu_{\rm IC\,min} < 1.2 \times 10^{17}$ Hz, we find $5 < \gamma_{\rm min} < 100$. In the following treatment we assume $\gamma_{\rm min} = 10$. A similar constraint is found for the jet of PKS 0637–752 (Tavecchio et al., 2000b). However, Mueller & Schwartz (2008) suggest $\gamma_{\rm min} \approx 50 - 80$ based on the results of spectral fitting to the X-ray spectrum of the jet of PKS 0637–752.

In addition to constraining the low energy cutoff, the optical upper limits constrain the high energy cutoff in the electron energy distribution because, in all except knot 6, an extrapolation of the synchrotron spectrum from radio to optical frequencies lies well above the optical upper limits. The synchrotron spectrum must therefore cutoff below the HST observing frequencies. The electrons responsible for the synchrotron emission observed at frequency $\nu_{\rm syn}$ have Lorentz factors $\gamma \sim (\pi \nu'_{\rm syn}/\Omega_0)^{1/2}$. Assuming $B < 100\ \mu G$ and $\delta \lesssim 10$ we find the maximum Lorentz factor $\gamma_{\rm max}$ can be anywhere below 2.5×10^5. In the following treatment we assume $\gamma_{\rm max} = 10^5$ for all knots. Note that the results of IC/CMB modeling (namely the magnetic field strength and jet Lorentz factor) are insensitive to the assumed value for $\gamma_{\rm max}$.

The Model: For each of the jet knots, we applied the one zone IC/CMB model using standard formulae (Dermer, 1995; Harris & Krawczynski, 2002, — see also

§2.6.1). The jet knots may be separate moving portions (i.e. "blobs") of jet material (eg. Stawarz et al., 2004) or stationary shocks in a continuous flow. The assumed geometry affects the calculation of jet parameters due to the difference in the dependence of flux density on Doppler factor in each case (see §2.2). Therefore we calculate the jet parameters assuming both jet and blob geometries. Using the jet parameters derived from the IC/CMB model, we have also calculated the jet kinetic energy flux in the the case of a purely leptonic and electron/proton jet. To calculate the jet kinetic luminosity we assume $\Gamma \approx \delta$ and

$$L_{jet}^{e^-e^+} \approx \pi R^2 \Gamma^2 c \left(\frac{\left[\frac{B}{\text{Gauss}}\right]^2}{3\pi} \right) \quad \text{ergs/s} \tag{4.16}$$

$$L_{jet}^{e^-p} \approx \pi R^2 \Gamma^2 c \left(\left(\frac{\Gamma - 1}{\Gamma}\right) n_e m_p c^2 + \frac{\left[\frac{B}{\text{Gauss}}\right]^2}{3\pi} \right) \quad \text{ergs/s} \tag{4.17}$$

The results from the IC/CMB modeling are given in Table 4.5 and plotted in Figure 4.10. The input parameters were fixed at $\gamma_{\text{min}} = 10$, $\gamma_{\text{max}} = 10^5$ and $\alpha = 0.8$. The uncertainties were determined by taking account of the uncertainty in flux density and volume measurements as well as the uncertainty in spectral index assumed to be $\Delta\alpha = 0.05$. The uncertainties in $\gamma_{\text{min,max}}$ were not taken into account, so that the quoted uncertainties are underestimates. Furthermore, we have not taken account of the possibility of a large systematic error associated with the model assumptions such as enforcing equipartition between the particle and magnetic energy densities (see Schwartz et al., 2006).

4.2.3 Synchrotron Spectrum of knot 6: Broken Power-Law?

The radio through optical spectrum for knot 6 can be fit using a broken power-law with a break of $\Delta\alpha = 0.5$. This suggests that radiative cooling may be responsible for the steeper spectrum at optical frequencies. In this section we consider whether the jet parameters derived from IC/CMB modeling are consistent with this interpretation of the radio to optical spectrum of knot 6.

Figure 4.11 illustrates the broken power-law fit to the SED of knot 6. The parameters of this fit are $\alpha = 0.8$, $\nu_{\text{b}} = 8 \times 10^{12}$ Hz and $\nu_{\text{max}} = 10^{16}$ Hz. The cooling break occurs at a frequency, ν_{b}, corresponding to the electron energy at which the cooling time-scale, τ'_{cool}, is equal to the dynamical time-scale, τ'_{esc}, for electrons to escape the knot, measured in the jet rest frame. The cooling time-scale

$$\tau'_{\text{cool}} = \frac{\gamma}{|d\gamma/dt'|} = \frac{3 m_e c}{4\sigma_T \left(U_{\text{rad}} + U_B\right) \gamma} \tag{4.18}$$

where U_{rad} is the CMB energy density in the rest frame of the jet plasma ($U_{\text{rad}} = 4 \times 10^{-13}(1+z)^4\Gamma^2$ ergs/cm^3), and U_B is the magnetic energy density ($U_B =$

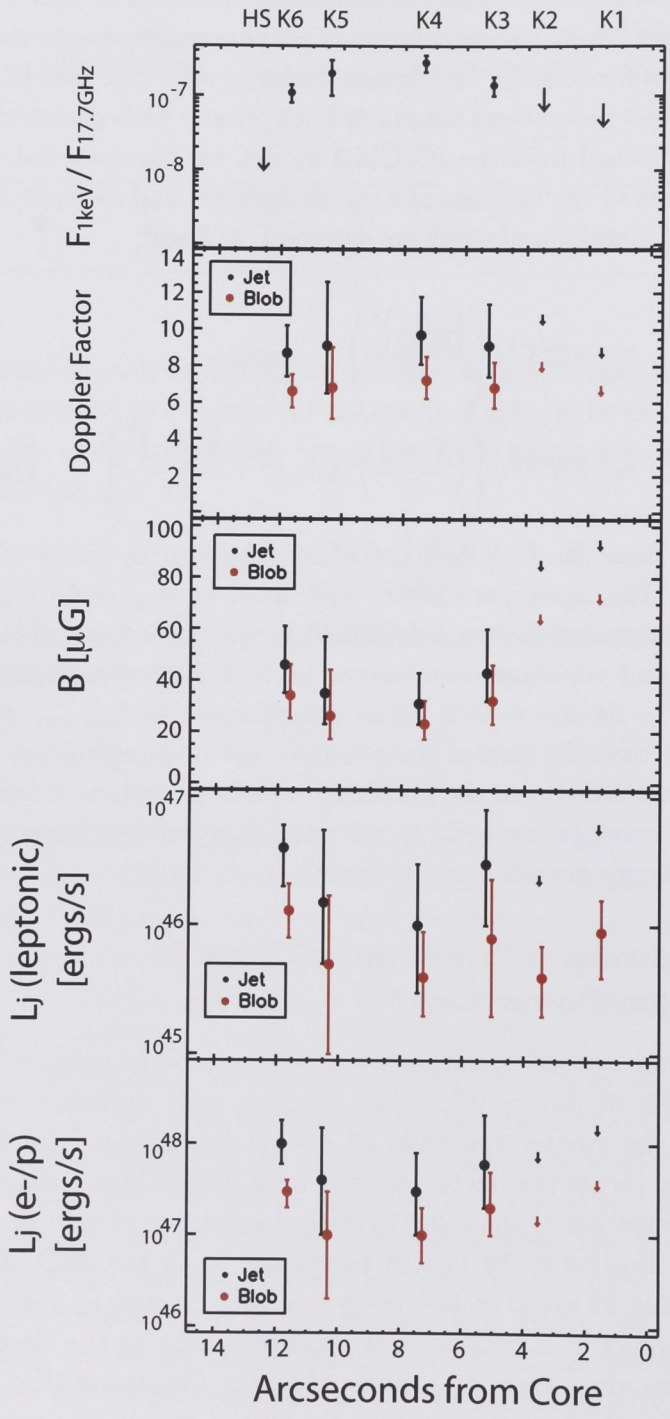

Figure 4.10: Plot of jet parameters for each knot derived from IC/CMB modeling. These results are given in Table 4.5

Table 4.5. Inverse Compton Modeling Results

Knot ID	Assumed Geometry	$\frac{F_{1keV}}{F_{17.7\ GHz}}$ $[\times 10^{-8}]$	$B_{eq}^{\delta=1}$ $[\mu G]$	δ	B $[\mu G]$	n_e $[\times 10^{-6}\ cm^{-3}]$	$L_{jet}^{e^-e^+}$ $[\times 10^{46}\ ergs\ s^{-1}]$	$L_{jet}^{e^-p}$ $[\times 10^{46}\ ergs\ s^{-1}]$
Knot 1	Jet	< 4	300^{+90}_{-60}	< 8	> 55	> 6	< 5	< 120
	Blob	< 4	"	< 6	> 40	> 5	$0.9^{+0.8}_{-0.4}$	< 30
Knot 2	Jet	< 6.5	320^{+100}_{-70}	< 10	> 50	> 5	< 2	< 60
	Blob	< 6.5	"	< 7.5	> 40	> 4	$0.4^{+0.3}_{-0.2}$	< 12
Knot 3	Jet	14 ± 4	220^{+70}_{-50}	9 ± 2	40^{+20}_{-10}	$3^{+4}_{-1.5}$	3^{+5}_{-2}	60^{+150}_{-40}
	Blob	14 ± 4	"	7 ± 1	30 ± 10	2^{+2}_{-1}	$0.8^{+1.5}_{-0.6}$	20^{+30}_{-10}
Knot 4	Jet	28 ± 7	170^{+50}_{-40}	$10^{+2}_{-1.5}$	30 ± 10	2^{+2}_{-1}	$1^{+2}_{-0.7}$	30^{+50}_{-20}
	Blob	28 ± 7	"	7 ± 1	20^{+10}_{-5}	$1^{+1}_{-0.5}$	$0.4^{+0.5}_{-0.2}$	10^{+10}_{-5}
Knot 5	Jet	20 ± 10	180^{+80}_{-50}	9 ± 3	40^{+20}_{-10}	$2^{+4}_{-1.5}$	1.5^{+4}_{-1}	40^{+110}_{-30}
	Blob	20 ± 10	"	7 ± 2	30^{+20}_{-10}	$1^{+3}_{-0.6}$	$0.5^{+1.2}_{-0.4}$	10^{+20}_{-8}
Knot 6	Jet	11 ± 3	230^{+50}_{-40}	9 ± 1.5	50 ± 10	$4^{+4}_{-1.5}$	4 ± 2	100^{+80}_{-40}
	Blob	11 ± 3	"	6.5 ± 1	30 ± 10	2^{+2}_{-1}	$1.3^{+0.8}_{-0.5}$	30 ± 10
HS	Jet	< 1	400 ± 80	< 6	—	—	—	—
	Blob	< 1	"	< 5	—	—	—	—

$B^2/8\pi$ ergs/cm^3). The jet parameters derived from the IC/CMB model for this knot imply that inverse Compton losses dominate over synchrotron losses, since the CMB energy density in the jet rest frame is greater than the magnetic energy density.

The escape time-scale in the lab frame is $\tau_{esc} = L/\beta_{jet}c \approx L/c$ where L is the length of the knot in the observer's frame. Accounting for time-dilation, the escape time-scale in the rest frame of the jet plasma is

$$\tau'_{esc} = \frac{L}{\Gamma c} \tag{4.19}$$

The break frequency is related to the break Lorentz factor via

$$\nu_b = \frac{\delta}{(1+z)} \frac{3}{4\pi} \Omega_0 \gamma_b^2 \tag{4.20}$$

Hence, inverse Compton cooling results in a cooling break at an observed frequency

$$\nu_b = \left[\frac{27}{64\pi} \frac{m_e q c^3}{\sigma_T^2} \frac{1}{U_{rad,0}^2} \right] (1+z)^{-9} L^{-2} B \delta \Gamma^{-2} \tag{4.21}$$

$$\approx \left[\frac{27}{64\pi} \frac{m_e q c^3}{\sigma_T^2} \frac{1}{U_{rad,0}^2} \right] (1+z)^{-9} L^{-2} B \Gamma^{-1} \tag{4.22}$$

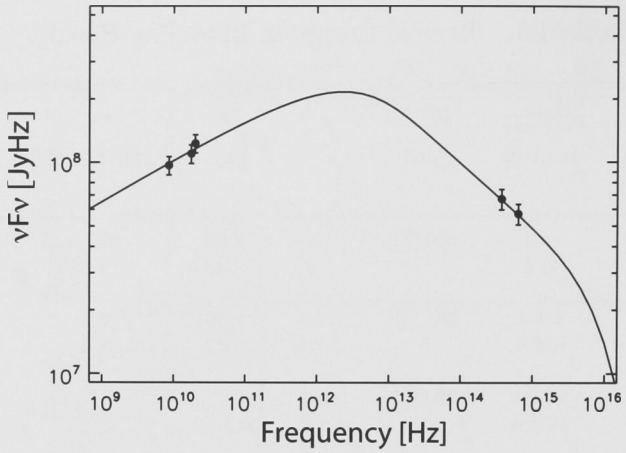

Figure 4.11: Broken power-law synchrotron spectrum fit to the radio to optical spectral energy distribution of knot 6. The parameters of the fit are: $\alpha = 0.8$, $\nu_b = 7 \times 10^{12}$ Hz, $\nu_{\rm max} = 10^{16}$ Hz.

where $U_{\rm rad,0} = 4 \times 10^{-13}$ ergs/s is the CMB energy density at z=0. In the case of continuous flow ("jet" geometry) the IC/CMB model parameters calculated for knot 6 are: $\Gamma = 9$, B=50μG. The estimation of the knot length from the observed knot size is not straightforward, as it depends on the geometry of the knot and the orientation of the jet. Often, when modeling jet knots, a spherical geometry is assumed with the spherical radius equal to the jet radius, even when the jet knots are known to be elongated in the jet direction (eg. Sambruna et al., 2001). Following this procedure, using the observed jet diameter for the knot length, we have $L \approx 0\farcs4 \approx 3$ kpc $\approx 10^{22}$ cm, and the predicted break frequency is $\nu_b \approx 2 \times 10^{15}$ Hz; two orders of magnitude greater than the observed value. However, the radio knot is marginally resolved in the 20GHz ATCA image and found to be elongated in the jet direction with length $L \sim 0\farcs6$. Note that the upper limit to the size of the X-ray knot is $0\farcs6$. The maximum allowed viewing angle for $\delta = 9$ is $\theta_{\rm max} \approx 6.4°$, therefore, the de-projected knot length is $L > 0\farcs6/\sin\theta_{\rm max} \approx 5'' \approx 40$ kpc $\approx 10^{23}$ cm. In this case, the predicted break frequency is $\nu_b \sim 2 \times 10^{13}$ Hz: within a factor of 3 of the observed break frequency. Hence, the jet parameters derived from IC/CMB modeling of knot 6 are broadly consistent with the break frequency estimated by fitting a broken power-law to the radio and optical data points.

4.2.4 Spectral Analysis of the Quasar Core

For the spectral analysis of the quasar core, events were extracted using a circular aperture of radius $2''$ centered on the core position. A total of 3687 events were extracted with energies in the range 0.5-7keV. The pile-up fraction is estimated

Table 4.6. Results of model fits to the X-ray spectrum of the quasar core.

Model	α	$F_{1\mathrm{keV}}$ [nJy]	Neutral Hydrogen Column Density [cm^{-2}]	Line Equivalent Width [eV]	Line Redshift	χ^2 (d.o.f.)
0	0.73 ± 0.05	79 ± 3	10^{15} cm^{-2}	—	—	141.3 (146)
1	0.84 ± 0.05	87 ± 3	3.41×10^{20} cm^{-2} (fixed)	—	—	146.4 (147)
2	0.85 ± 0.05	87 ± 3	3.41×10^{20} cm^{-2} (fixed)	140 ± 60 eV	1.07 ± 0.02	134.7 (145)

using the PIMMS Proposal Planning Toolkit to be 2%, and is therefore neglected in the following analysis. Spectral analysis was performed in Sherpa. The pulse-height amplitude spectrum was re-binned to have a minimum of 20 counts per bin, so that the χ^2 statistic could be applied.

We first fit the spectrum using an absorbed power-law. The results of this fit are given in Table 4.6 (model 1). Inspection of the residuals of the power-law fit revealed an excess of emission around 3.1 keV. This energy is consistent with redshifted Fe Kα emission, which has rest energy 6.4 keV. To model the line, a Gaussian component was added using the XSZGAUSS model in Sherpa. The spectral resolution of the ACIS S3 chip is approximately $\sigma \sim 0.2$ keV at 3 keV (Figure 6.8 of the *Chandra* Proposers' Observatory Guide[7]). The line was found to be unresolved, therefore the intrinsic line width was fixed at $\sigma = 0.01$ keV, a value much less than the instrument spectral resolution. The rest energy of the line was fixed at 6.4 keV, and the line normalization and redshift were allowed to vary. The results of the model fit including the emission line component are given in table 4.6 (model 2). An F-test was performed using the Sherpa function FTEST to determine the significance of the line detection. The results of the F-test indicate that the line is detected at the 99.8% level.

Marshall et al. (2005) assigned a tentative redshift of z=1.04 to this object based on a spectrum obtained at the Magellan telescope. The redshifted Fe Kα emission line is consistent with this redshift.

4.2.5 Lobes

Within the lobes, the radiation energy density of the CMB ($U_{\mathrm{CMB}} = 7 \times 10^{-11}$ ergs cm^{-3}) is greater than the energy density of the locally generated synchrotron radiation. Note that for the lobes $\delta = 1$. We therefore model the X-ray emission from the radio lobes in terms of inverse Compton scattering of the CMB. In modeling the radio lobe emission we follow Croston et al. (2005) by assuming a broken power-law with $\gamma_{\mathrm{min}} = 10$ and $\gamma_{\mathrm{max}} = 10^5$ and we use the radio and X-ray flux densities to normalize the synchrotron and inverse Compton components respectively. The

[7] *Chandra* Proposers' Observatory Guide available at `http://cxc.harvard.edu/proposer/POG/html/`

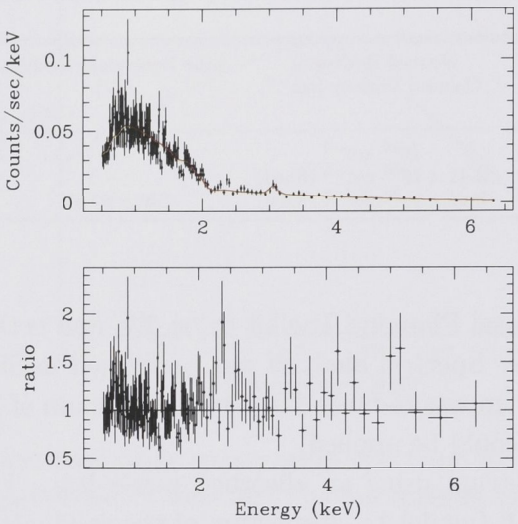

Figure 4.12: Observed ACIS-S spectrum of the core of PKS 2101–490 with model spectrum (absorbed power-law with Fe Kα emission line at 3.1 keV) overlaid. Also shown are the residuals of the fit, expressed as the ratio of the data to the model in each bin.

radio spectral index of the lobe is $\alpha_{\rm r} \approx 1.05 \pm 0.1$. We therefore assume an electron energy index $a = 2.1$, so that the slope of the model synchrotron spectrum above the break matches the observed slope. The X-ray spectral index in the lobe is $\alpha_{\rm X-ray} = 1.3 \pm 0.3$. The inverse Compton X-ray emission in the *Chandra* X-ray band (0.5 - 7 keV) is produced by $\gamma \approx 600 - 2000$ electrons. The steep X-ray spectrum therefore indicates that the Lorentz factor corresponding to the cooling break must be $\gamma_b \lesssim 600$. We assume $\gamma_{\rm b} = 400$. To model the X-ray emission, we use equation (2.61) for the inverse Compton emissivity, with

$$n(\nu_0) = \frac{8\pi\nu_0^2}{c^3}\left(e^{\frac{h\nu_0}{kT}} - 1\right)^{-1} \tag{4.23}$$

for the number density of the microwave background, as appropriate for a black-body radiation field of temperature T. We use $T = (1+z)T_0$ K where $T_0 = 2.7$ K is the temperature of the CMB at z=0.

Figure 4.13 shows the model fit to the radio and X-ray data for the counter lobe. We perform a similar fit to the lobe SED, with the same assumed $\gamma_{\rm min}$, $\gamma_{\rm b}$, $\gamma_{\rm max}$ and α. The results are given in table 4.7. We find that the lobes are far from equipartition conditions with the magnetic field more than a factor of 5 below the equipartition magnetic field strength. The particle energy density is more than two orders of magnitude greater than the magnetic energy density.

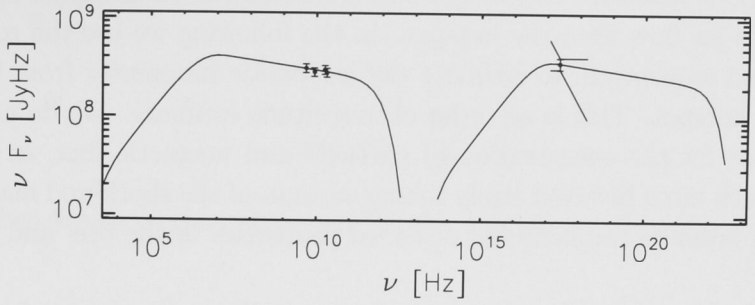

Figure 4.13: Counter-lobe spectral energy distribution. The solid line is the best fit synchrotron plus IC/CMB model. The parameters of the fit are: $\alpha = 0.55$, $\gamma_{\rm min} = 10$, $\gamma_{\rm b} = 400$, $\gamma_{\rm max} = 10^5$, $B = 15\,\mu$G, $K_e = 1.8 \times 10^3\,{\rm m}^{-3}$, $V = 9 \times 10^{63}\,{\rm m}^3$

Table 4.7. Results of model fits to the lobe spectra.

	$B_{\rm eq}$ [μG]	$B_{\rm obs}$ [μG]	U_e/U_B	Total Energy ergs
Counter-lobe	85	15	450	4×10^{55}
Lobe	80	13	600	1.5×10^{55}

4.3 Comparison of the Jet and Hotspot of PKS 2101–490

After 10 years of dedicated *Chandra* observations and theoretical work, many questions regarding the knot production mechanism, particle acceleration mechanism and X-ray emission mechanism remain unanswered. Further constraints are required to help improve this situation — simply applying one-zone models to more and more objects is not fruitful. In this section we use a simple model of the hotspot to constrain the jet energy flux. The energy flux determined from modeling the hotspot is then compared with the jet energy flux estimated from modeling the jet X-ray emission using the one-zone IC/CMB model.

4.3.1 Estimating the Jet Energy Flux from Hotspot Parameters

In this section we consider the conservation of energy and momentum across the terminal jet shock in order to estimate the jet energy flux required to account for the observed hotspot emission.

The relativistic Rankine-Hugoniot equations express the conservation of par-

ticles, energy, momentum and magnetic flux across the terminal jet shock which separates the jet flow from the hotspot. In the following we use the conservation of energy and momentum to estimate the jet kinetic luminosity from the parameters of the hotspot. This is an order of magnitude estimate. We do not consider the equations for the conservation of particles and magnetic flux, as this would require a much more involved study taking account of the shock and magnetic field obliquity in order to reconcile the observed properties in the pre- and post-shock plasma.

The flux of energy and momentum along a uniform jet of area A, relativistic enthalpy w, magnetic field components perpendicular and parallel to the flow direction $B_\perp$ and $B_{||}$, speed βc and corresponding bulk Lorentz factor Γ are (eg. Double et al., 2004):

$$\text{Energy Flux} \quad F_E = A\Gamma^2\beta c\left(w + \frac{B_\perp^2}{4\pi}\right) \tag{4.24}$$

$$\text{Momentum Flux} \quad F_M = A\left[\Gamma^2\beta^2\left(w + \frac{B_\perp^2}{4\pi}\right) + p + \frac{B_\perp^2 - B_{||}^2}{8\pi}\right] \tag{4.25}$$

Let ϵ be the particle energy density, p the pressure, and ρ the mass density. The relativistic enthalpy is $w = \epsilon + p + \rho c^2$.

In the jet, where $\Gamma >> 1$, we have $F_{E,1} \approx F_{M,1}c$. Hence, from the conservation of momentum across the terminal shock, we have $F_{E,1} \approx F_{M,2}c$. This equality holds regardless of assumptions about the jet characteristics such as composition or the ratio of magnetic to particle energy densities in the jet or hotspot. We can therefore estimate the jet kinetic luminosity in terms of the hotspot parameters simply by calculating the momentum flux in the hotspot.

Electron Positron Jet

In the following, we assume that in the hotspot the magnetic energy density is in equipartition with the particle energy density. This assumption is justified by the observational evidence that high luminosity hotspots are generally close to equipartition (Hardcastle et al., 2004), and the fact that this hotspot has a high radio luminosity ($L_{8\text{GHz}} = 10^{26}$ W Hz^{-1} Sr^{-1}). We further assume that the magnetic field is perpendicular to the jet direction, as indicated by the radio polarization, and that the leptons have an ultra-relativistic equation of state. For the hotspot, the model assumptions are summarized as follows:

$$B_{\perp,2} = B_2 \tag{4.26}$$

$$B_{||,2} = 0 \tag{4.27}$$

$$\epsilon_2 >> \rho_2 c^2 \tag{4.28}$$

$$p_2 = \frac{1}{3}\epsilon_2 \tag{4.29}$$

$$w_2 = \frac{4}{3}\epsilon_2 \tag{4.30}$$

$$\epsilon_2 = \frac{B_2^2}{8\pi} \tag{4.31}$$

Hence, the two terms in the expression for the momentum flux (equation (4.25)) are

$$\Gamma^2\beta^2\left(w_2 + \frac{B_{\perp,2}^2}{4\pi}\right) = \Gamma^2\beta^2\frac{10}{3}\epsilon_2 \tag{4.32}$$

$$\text{and} \qquad p_2 + \frac{B_{\perp,2}^2}{8\pi} = \frac{4}{3}\epsilon_2 \tag{4.33}$$

Therefore, provided $\beta_2 \lesssim 0.3$, the term involving β^2 in the expression for momentum flux (equation (4.25)) can be neglected. Combining equations (4.25) and (4.33), the jet kinetic luminosity in the purely leptonic case is

$$L_{\rm jet}^{e^\pm} \approx \frac{4\,c}{3}A_2\epsilon_{e,2} \tag{4.34}$$

Applying the assumption of equipartition between particle and magnetic energy densities, we obtain

$$L_{\rm jet}^{e^\pm} = \frac{c}{6\pi}A_2B_2^2 \tag{4.35}$$

Proton Electron Jet

Let us now consider the case of an electron/proton jet. We assume that the electron population has an ultra-relativistic equation of state, while the proton population is at best mildly relativistic and can be described with a non-relativistic equation of state. We assume that the electron and proton populations equilibrate in the hotspot, as suggested by the results of chapter 3. For the hotspot, the model assumptions are summarized as follows:

$$B_{\perp,2} = B_2 \tag{4.36}$$

$$B_{||,2} = 0 \tag{4.37}$$

$$p_{e,2} = \frac{1}{3}\epsilon_{e,2} \tag{4.38}$$

$$p_{p,2} = \frac{2}{3}\epsilon_{p,2} \tag{4.39}$$

$$\epsilon_{e,2} = \epsilon_{p,2} \tag{4.40}$$

$$\frac{B_2^2}{8\pi} = \epsilon_2 = \epsilon_{e,2} + \epsilon_{p,2} \tag{4.41}$$

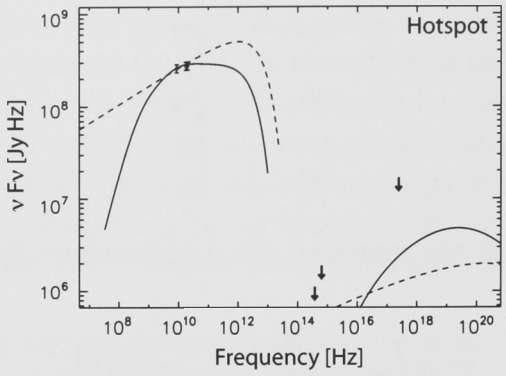

Figure 4.14: Synchrotron spectrum fits to the hotspot radio data. Also shown is the equipartition SSC spectrum corresponding to each of the synchrotron spectra. The synchrotron spectrum is not well constrained. We fit two "extreme" models to the data, and expect that the parameters of these models bound the true parameters.

Hence,

$$w_2 = \frac{4}{3}\epsilon_{e,2} + \frac{5}{3}\epsilon_{p,2} + \rho c^2 \tag{4.42}$$

$$= \epsilon_{e,2}\left(3 + \frac{\rho c^2}{\epsilon_e}\right) \tag{4.43}$$

$$= \epsilon_{e,2}\left(3 + \frac{1}{\langle\gamma_e\rangle}\frac{m_p}{m_e}\right) \tag{4.44}$$

and

$$F_{M,2} = A_2\epsilon_{e,2}\left(\Gamma^2\beta^2\left(7 + \frac{1}{\langle\gamma_e\rangle}\frac{m_p}{m_e}\right) + 3\right) \tag{4.45}$$

As with the previous case, if $\beta \lesssim 0.3$ and $\langle\gamma_e\rangle \gtrsim 200$ in the hotspot, the term involving β^2 in the expression for momentum flux can be neglected, and we simply have

$$L_{\rm jet} \approx 3cA_2\epsilon_{e,2} \tag{4.46}$$

$$= \frac{3c}{8\pi}A_2B_2^2 \tag{4.47}$$

4.3.2 Comparison of Energy Flux Estimates

We have modeled the hotspot synchrotron spectrum under the assumption of equipartition. The synchrotron spectrum is not well constrained. For this reason we fit two "extreme" models to the radio spectrum, and expect that the true parameters lie between the parameters of these two "extreme" models. Using this method we find that $B_{2,\rm eq}$ is in the range $270 \pm 100\,\mu$G (see Figure 4.14 and Table

Table 4.8. Equipartition Synchrotron Modeling Results for the hotsot

Fixed Parameters				Derived Parameters	
α	$\gamma_{\rm min}$	$\gamma_{\rm b}$	$\gamma_{\rm max}$	$B_{\rm eq}$ [μG]	$n_{e_{\rm eq}}$ [$\times 10^{-6}$ cm^{-3}]
0.8	10	10^5	10^5	370	130
0.5	10^3	5×10^3	10^5	170	0.23

4.8). Taking $A_2 = 6 \pm 1 \times 10^{43}$ cm^2 as determined from the 20GHz ATCA image, we find:

$$L_{\rm jet}^{e^\pm} = 7 \pm 4 \times 10^{45} \, {\rm ergs/s} \quad (4.48)$$

$$L_{\rm jet}^{e/p} = 1.5 \pm 0.8 \times 10^{46} \, {\rm ergs/s} \quad (4.49)$$

These energy flux estimates are broadly consistent with those obtained for other radio galaxies using different methods, for example through estimates of source ages and the total energy contained in radio lobes (Rawlings & Saunders, 1991) or modeling Blazar emission (Celotti, 2003).

The jet energy flux derived from IC/CMB models for knot 6 are listed in Table 4.9. Note that these energy flux estimates are obtained under the assumption of a stationary flow pattern (i.e. "jet" geometry). We do not consider the estimates obtained under the assumption of a blob geometry (i.e. a discrete moving portion of jet material), since in that case we do not expect conservation of energy between the jet and hotspot. For the leptonic jet, the two estimates of kinetic luminosity agree to within an order of magnitude (note the large errors on jet energy flux estimates), while in the case of the proton/electron jet, the energy flux estimates differ by nearly two orders of magnitude. There are a number of ways to interpret these results, which we now discuss.

The closer agreement between the two energy flux estimates in the case of the leptonic jet may be taken as evidence in favour of an electron/positron plasma. However, there are numerous studies that favour an electron/proton plasma in AGN jets. (eg. Mehta et al., 2008; Tavecchio et al., 2000a, see also Chapter 3 of this thesis). If the jets are composed of electron/proton plasma, then there are a number of possibilities for the discrepancy between energy flux estimates. Firstly, the energy flux estimate based on the hotspot parameters may be an underestimate. In the above calculations, we assumed that the hotspot plasma is in a state of equipartition between particle and magnetic energy densities, and that the energy density in protons is equal to the energy density in electrons. It was argued that these assumptions are justified. However, if the hotspot is far from equipartition, or the proton energy density is much greater than the electron energy density, then the estimated kinetic luminosity based on the hotspot parameters is

Table 4.9. Comparison of Jet Kinetic Luminosity Estimates

Jet Component	$L_{jet}^{e^{\pm}}$ [ergs/s]	$L_{jet}^{e/p}$ [ergs/s]
Knot 6 (IC/CMB modeling)	$4 \pm 2 \times 10^{46}$	$1.0^{+0.8}_{-0.4} \times 10^{48}$
Hotspot (Conservation equations)	$7 \pm 4 \times 10^{45}$	$1.5 \pm 0.8 \times 10^{46}$

an under-estimate. In this context it should be noted that the lobes were found to be far from equipartition conditions based on inverse Compton modeling.

Alternatively, the discrepancy between the two energy flux estimates may be explained if the energy flux estimated from IC/CMB modeling is an over-estimate. The kinetic luminosity of an electron/proton jet estimated from IC/CMB modeling (10^{48} ergs/s) is extremely high, and is equal to the Eddington luminosity of a 10^{10} solar mass black hole. Some authors are uncomfortable with the high kinetic luminosities implied by the IC/CMB model for jet X-ray emission (see eg. Atoyan & Dermer, 2004). Indeed, the results of this analysis suggest that the one zone IC/CMB model may over predict the jet kinetic luminosity if the jet is composed of protons and electrons.

In summary, we have identified a discrepancy between two jet energy flux estimates in the case of a proton/electron jet which is not present when a leptonic jet composition is assumed. This may support the hypothesis of a leptonic jet composition, or it may be indicative of the inadequacies of the one-zone IC/CMB model for jet X-ray emission. In this context, the following section is highly relevant.

Inspection of equations (4.35) and (4.47) shows that the simple hotspot model predicts a linear correlation between $L_{\rm jet}$ estimated from IC/CMB modeling and B_2^2, where B_2 is the hotspot magnetic field strength. It may be possible to look for this correlation in existing data if there are a sufficient number of suitable objects in the literature for which $L_{\rm jet}$ can be estimated from IC/CMB modeling of jet X-ray emission, and B_2 can be estimated from radio images. The existence of such a correlation would provide strong support for the IC/CMB model.

Lastly, it should be emphasized that the method described here to estimate the jet kinetic luminosity based on the hotspot parameters can be used to test and/or constrain alternative models of jet X-ray emission.

4.4 The Size of Knot 6 in PKS 2101–490

A detailed discussion of the issues associated with X-ray emission from jet knots was presented in §1.4.1. One of the major issues is related to the knot size. Tavecchio et al. (2003) have argued that the interpretation of jet knots in terms of strong shocks in a continuous flow is incompatible with the observations that the X-ray

surface brightness drops rapidly outside the knots, and the knot brightness profiles are largely frequency independent. In the IC/CMB model for jet X-ray emission, the rapid drop in X-ray brightness is unexpected because the cooling time-scale of X-ray emitting ($\gamma \sim 100$) electrons is much longer than the escape time-scale for particles to escape the knot. Tavecchio et al. (2003) argue that if a knot is homogeneously filled by a single relativistic particle population, radiative and adiabatic losses alone cannot account for the rapid drop in X-ray brightness outside the knot, and cannot explain the frequency independent brightness profiles.

This issue may be important for knot 6 of PKS 2101–490. The radio emission from knot 6 was estimated to have a major axis (Gaussian FWHM) of 0.″6 extended along the jet direction, while the X-ray emission was shown to have a Gaussian FWHM no greater than 0.″6. Hence, the size of the X-ray knot is less than or equal to the size of the radio knot. As with the knots of 3C 273 and other quasar jets, this observation may pose a serious problem for the IC/CMB model for the X-ray emission associated with this knot.

Two alternative models have been proposed to resolve this issue of the rapid drop in X-ray brightness outside the knots. Tavecchio et al. (2003) propose that knots in kpc-scale jets are composed of many small (unresolved) clumps, associated with sites of particle acceleration, that are hotter and more dense than their surroundings. These clumps can expand much faster than a single homogenous knot, thereby allowing for rapid adiabatic cooling that would produce a rapid drop in brightness, and a frequency independent knot profile.

Stawarz et al. (2004) have suggested an alternative explanation for the existence of jet knots with frequency independent brightness profiles. They suggest that the knots represent separate moving portions of a relativistic jet with excess kinetic power and argue that such a situation is expected if the activity of central engine is intermittent or highly modulated. In this model, Stawarz et al. (2004) postulate a synchrotron origin for the X-ray emission in quasar jets. Such a model requires particle acceleration acting over an extended volume rather than occurring at a single shock front, since the synchrotron X-ray emitting electrons have extremely short cooling timescales. In this case, the knot sizes are related to the size of the particle acceleration sites and not to the cooling length of the electrons, as in the single-shock IC/CMB and SSC models.

Further consideration of the knot production mechanism and the X-ray emission mechanism, taking account of the limits on X-ray and radio sizes for knot 6, is required in future studies of PKS 2101–490.

Chapter 5

Conclusions

5.1 Synchrotron Self Compton Spectrum

There is an apparently common misconception that the synchrotron self Compton spectrum produced by a power-law electron energy distribution of the form $N(\gamma) \propto \gamma^{-a}$ is a power-law with spectral index $\alpha = (a-1)/2$ over a broad range of frequencies. I have presented a detailed analysis of the synchrotron self Compton emission spectrum produced by a power-law electron energy distribution, clearly describing why the SSC spectrum does not match the analytic power-law approximation over a broad range of frequencies.

5.2 The Luminous Hotspot of PKS 1421–490

My investigations carried out in this thesis have identified for the first time an exceptional hotspot in the radio galaxy PKS 1421–490. This hotspot, which has until now been interpreted as an active galactic nucleus, has intrinsic brightness (after accounting for cosmological effects) more than 1000 times greater than the hotspots in Cygnus A. It is by far the most luminous X-ray hotspot to have been observed, with an isotropic X-ray luminosity comparable to that of the whole jet of PKS 0637–752. Observations were made using the Long Baseline Array and the Australia Telescope Compact Array and were combined with previously published radio, optical and X-ray flux densities in order to construct the hotspot spectrum.

We successfully modeled the radio to X-ray spectral energy distribution of the luminous hotspot using a standard one-zone synchrotron self Compton model with a near equipartition magnetic field strength of 3 mG. There is a strong brightness asymmetry between the approaching and receding hotspots, and the hot spot spectrum remains flat ($\alpha \approx 0.5$) well beyond the predicted cooling break for a 3 mG magnetic field, indicating that the hotspot emission may be Doppler beamed. We suggest that a high plasma velocity beyond the terminal jet shock could be the result of a dynamically important magnetic field in the jet, resulting in Doppler boosted hotspot emission. However, some aspects of the hotspot morphology may

argue against an interpretation involving significant Doppler beaming. LBA observations at 1.4 GHz will be required to further investigate the hotspot morphology.

There is a significant change in the slope of the hotspot radio spectrum at GHz frequencies. We successfully modeled this feature by incorporating a cutoff in the electron energy distribution at $\gamma_{\rm min} \sim 650$ (assuming a Doppler factor of unity). If the hotspot emission is Doppler beamed with Doppler factor δ, the low energy cutoff is $\gamma_{\rm min} \approx 650\ \delta^{1/3}$. We have used the equations for the conservation of energy and particles in an un-magnetised proton/electron jet to obtain a general expression that relates the peak in the hotspot electron energy distribution to the jet bulk Lorentz factor. We have shown that a sharp decrease in electron number density below a Lorentz factor of about 650 would arise from the dissipation of bulk kinetic energy in an electron/proton jet with bulk Lorentz factor $\Gamma_{\rm jet} \gtrsim 5$. This value of jet Lorentz factor is consistent with jet Lorentz factors inferred from modelling the radio to X-ray spectra of quasar jets on kpc-scales (Tavecchio et al., 2000b; Schwartz et al., 2006; Kataoka & Stawarz, 2005). These results are of particular interest given that similar values of $\gamma_{\rm min}$ have been estimated for several other hotspots. Our analysis indicates that the value of $\gamma_{\rm min} \sim 10^4$ inferred by Blundell et al. (2006) for the hotspot of the radio galaxy 6C0905+3955 would require a jet Lorentz factor $\Gamma_{\rm jet} \gtrsim 35$.

An alternative explanation for the low frequency flattening in the radio spectrum of the northern hotspot of PKS 1421–490 may be that it is associated with the transition between a pre-acceleration mechanism, such as the cyclotron resonant process described by Hoshino et al. (1992) and Amato & Arons (2006), and diffusive shock acceleration.

Future LBA observations at 1.4 GHz will help to constrain the low energy end of the electron energy distribution, and infra-red observations are required to constrain the high frequency end of the synchrotron spectrum. More sophisticated models of the electron energy distribution will be required in future studies, to test the hypothesis that the flattening in the radio spectrum is associated with a transition between two distinct acceleration mechanisms.

5.3 The X-ray Jet of PKS 2101–490

I have presented an analysis of deep X-ray (*Chandra*), optical (HST) and radio (ATCA) observations of PKS 2101–490.

The 13″ long radio jet of PKS 2101–490 consists of several discrete knots. The X-ray to radio flux density ratio of individual knots is greatest in the outer parts of the jet. This trend is opposite to that which is often observed in quasar jets. Only one knot is detected in the optical images. However, the optical upper limits in the undetected knots place strong constraints on the knot spectra.

Radio to X-ray spectral energy distributions were extracted from seven distinct

regions of the jet, and we modeled the jet X-ray emission in terms of inverse Compton scattering of the cosmic microwave background (IC/CMB). This model implies that the jet remains highly relativistic hundreds of kpc from the nucleus, with a bulk Lorentz factor $\Gamma \sim 8$. The jet magnetic field strength is of order 30μG.

The X-ray emission peaks in a jet knot several kpc upstream from the terminal hotspot. This knot is the only one detected at optical wavelengths. The radio to optical spectrum of the brightest X-ray knot is well modeled by a broken power law with a cooling break at $\nu_b \approx 8 \times 10^{12}$ Hz. The observed break frequency is consistent with the predictions of a shock model for the knot in which the jet has bulk Lorentz factor $\Gamma \sim 9$ and is in a state of equipartition between magnetic and particle energy densities. However, we find that the size of the X-ray knot is no greater than the size of the radio knot. This observation may be inconsistent with models involving a single shock in a continuous flow.

In order to provide an additional constraint on models of jet X-ray emission, we have combined the observed hotspot parameters with the equations for the conservation of energy and momentum across a strong shock to estimate the jet energy flux. We have compared this estimate with the jet energy flux derived from IC/CMB modeling of jet X-ray emission, and find that in the case of a leptonic jet, the two energy flux estimates ($L_j \sim 10^{46}$ ergs/s) are comparable, but in the case of an electron/proton plasma, the energy flux estimate from IC/CMB modeling ($L_j \sim 10^{48}$ ergs/s) is nearly two orders of magnitude greater than the estimate based on the hotspot parameters. There are a number of ways to interpret this result. It may provide evidence in favour of an electron/positron jet, or it may be indicative of the inadequacies of the one-zone IC/CMB model for quasar jet X-ray emission. In this context we should again point out that the extent of the X-ray emission from the brightest X-ray knot is less than or equal to the extent of the corresponding radio emission. Tavecchio et al. (2003) have shown that such a situation poses a significant problem for the standard one-zone IC/CMB model for jet X-ray emission. Further consideration of the knot production mechanism and the X-ray emission mechanism, taking account of the limits on X-ray and radio sizes for the brightest X-ray knot, will be required in future studies of PKS 2101–490.

We have modeled the X-ray emission from the lobes in terms of inverse Compton scattering of the microwave background and find that the lobes are far from equipartition conditions, with a magnetic field strength more than a factor of 5 below the equipartition magnetic field strength.

Marshall et al. (2005) quote a tentative redshift of z=1.04 for PKS 2101–490 based on an optical spectrum from the Magellan telescope. An Fe Kα emission line is observed in the X-ray spectrum of the quasar core, with redshift $z = 1.07 \pm 0.02$. This result is consistent with the redshift quoted by Marshall et al. (2005).

5.4 Future Work

As discussed in Chapter 3, the hotspot radio spectra in some radio galaxies are observed to flatten towards low frequency, with the spectrum becoming flatter than the canonical $f_\nu \propto \nu^{-0.5}$ spectrum of diffusive shock acceleration. The onset of flattening in each of these sources corresponds to emission from electrons with Lorentz factors $\gamma \approx 300 - 1000$. This suggests that flattening of the electron energy distribution at $\gamma \sim 300 - 1000$ is a common feature in hotspots. Until now we have only been able to observe the spectrum begin to flatten, but how flat does the spectrum become? Is the low frequency spectrum consistent with a turnover in the electron energy distribution, or does the onset of flattening mark the transition between two distinct acceleration mechanisms (eg. Stawarz et al., 2007)? To address this question we must sample the electron energy distribution at lower energies than is currently achieved. To sample the low energy electron distribution we must observe high luminosity (hence high magnetic field strength) hotspots at low frequency. These observations must also be at high angular resolution so that the emission from the freshly accelerated particles in the hotspot can be isolated from the surrounding emission.

I suggest observing a sample of high luminosity hotspots in the northern hemisphere at high resolution over a wide frequency range with matched resolution using the VLBA (327 MHz and 610 MHz), MERLIN (1.5 GHz — 5 GHz) and the VLA (8 GHz — 43 GHz), so as to construct accurate hotspot spectra down to a frequency of 327 MHz. For hotspots with high magnetic field strengths (of order several mG as has been estimated for example in PKS 1421–490 and 3C351N) this corresponds to emission from electrons with Lorentz factors down to $\gamma \sim 150$. Hardcastle et al. (2004) have shown that the magnetic field strengths in high luminosity hotspots are close to the equipartition values. Therefore a direct relationship between frequency and electron energy can be evaluated using the equipartition magnetic field strength. In those objects where Chandra X-ray data exists or can be obtained, synchrotron self Compton modelling will provide a more robust estimate of the magnetic field strength (note that the conversion from frequency to energy is not highly sensitive to the magnetic field strength $\gamma \propto B^{-1/2}$).

Why is high angular resolution required? Scheuer & Williams (1968) showed that if a spherical region of plasma adiabatically expands by a factor of f, then the spectrum is shifted down in frequency by a factor of f^{-4}. This serves to illustrate that, if the hotspot spectrum is curved like the synchrotron model (solid line) shown in Figure 5.1, expansion of the plasma as it leaves the hotspot results in a significant steepening of the spectrum at a given frequency. At low resolution, the hotspot spectrum is contaminated by the steeper spectrum of the surrounding plasma. It is therefore vital to obtain high resolution images with matched resolution over a wide range of frequency. The VLBA (327 MHz, 610 MHz), MERLIN (1.5 GHz - 5 GHz) and the VLA (8 GHz - 43 GHz) provide the perfect combi-

nation for matched, high resolution (~0.1 - 0.2 arcsecond) imaging over a wide frequency range, extending to low frequency, that will allow the construction of accurate hotspot radio spectra as a means to answer the following questions:

- Is the low energy flattening in the electron energy distribution at $\gamma \sim 300 - 1000$ a common feature in hotspots?
- Is the low frequency flattening more likely due to a turn-over in the electron energy distribution, or a transition between two distinct acceleration mechanisms?
- Does the particle energy corresponding to the onset of flattening correlate with other properties of the source such as core dominance, source luminosity, hotspot luminosity etc.
- Do some hotspots have electron energy distributions that continue with the same slope down to $\gamma << m_p/m_e$?

The last point in effect refers to a null result. That is, the observation of a hotspot spectrum that continues with the same slope even at the lowest frequencies. This will be an important observation, as some models of particle acceleration predict a change in slope of the electron energy distribution at $\gamma \approx \Gamma \frac{m_p}{m_e} \gtrsim 2000$ where Γ is the jet Lorentz factor. For example, Fermi acceleration at a strong shock in an electron/proton plasma has an associated "injection problem" (Eilek & Hughes, 1991). The injection problem refers to the fact that in order for electrons to undergo first order Fermi acceleration, the particles' gyro-radius must be greater than the shock thickness. The shock thickness is approximated by the gyro-radius of the dominant protons in the post-shock plasma, which have energy $\Gamma m_p c^2$. Hence, Fermi acceleration is inefficient for electrons with energy $\gamma \lesssim \Gamma m_p/m_e$, and therefore this model predicts a change in slope of the electron spectrum at $\gamma \sim \Gamma m_p/m_e$.

Note that Cai et al. (2002) have demonstrated the capability of the VLBA to image hotspots of radio galaxies at 327 MHz achieving 0.1 arcsecond resolution and sensitivity $3\sigma \sim 3.5$ mJy/beam.

5.4.1 3C295 NW: An Illustrative Example

Harris et al. (2000) found that the radio spectrum of the north west hotspot of 3C295 is strongly curved at GHz frequencies in low resolution radio data, suggesting a turn-over in the hotspot electron distribution at a Lorentz factor $\gamma \sim 700$. Therefore, this bright hotspot makes a perfect test case for the proposed observing program.

Figure 5.1 displays the peak surface brightness of the hotspot 3C295 NW measured at 0.1 arcsecond resolution, along with a model synchrotron spectrum with low energy cutoff at $\gamma_{\rm min} = 700$ (solid line). The filled circles represent data points taken from the literature (Taylor & Perley, 1992), and the filled squares are fake

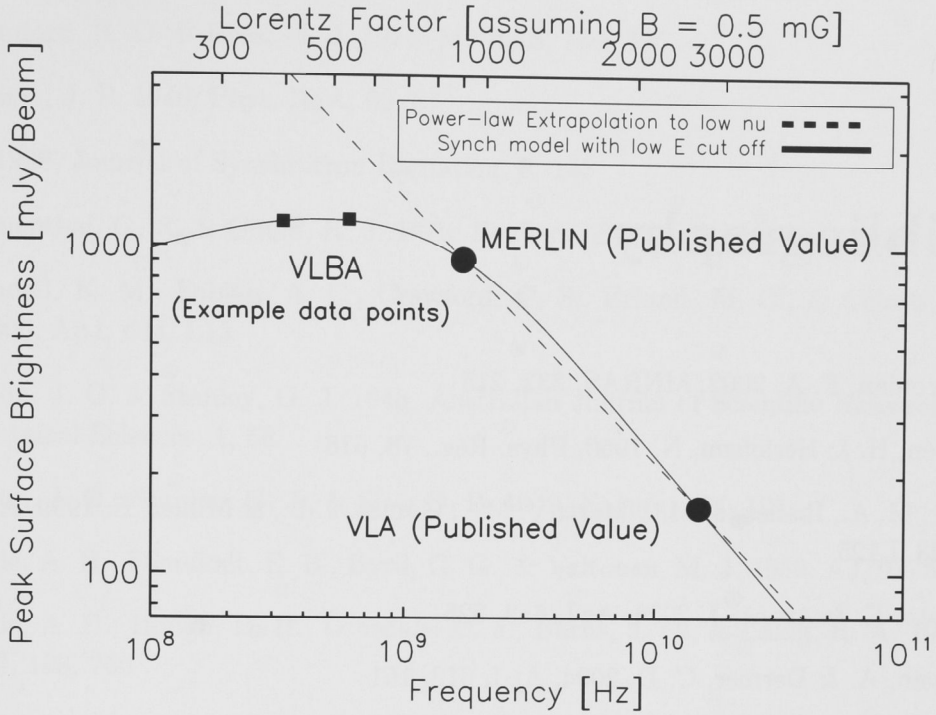

Figure 5.1: The radio spectrum of the north west hotspot of 3C295 at 0.1 arcsecond resolution. The filled circles represent data points taken from the literature (Taylor & Perley, 1992). The solid line is a synchrotron model for a plasma with magnetic field B=0.5mG and a power-law electron energy distribution with low energy cutoff at $\gamma_{\rm min} = 700$, as has been suggested for this source based on lower resolution radio images (Harris et al., 2000). The dashed line is an extrapolation of a power law fit to the two data points from the literature. The filled squares are fake VLBA data points at 327 MHz and 610 MHz chosen to lie on the model spectrum, and are included to illustrate the constraints that will be provided by the VLBA. Note that at 327 MHz the VLBA can reach a sensitivity in the order of a few mJy/beam (Cai et al., 2002).

VLBA data points at 327 MHz and 610 MHz. The fake VLBA data points are included to illustrate the constraints that will be provided by the VLBA. Note that at 327 MHz the VLBA can reach a sensitivity in the order of a few mJy/beam (Cai et al., 2002). This plot serves to illustrate that the hotspot will be detected with very high signal to noise, and the VLBA will provide useful constraints on the hotspot spectrum. Hotspots with higher magnetic field strength will allow us to probe even lower energy electrons - in some cases as low as $\gamma \sim 150$.

Bibliography

Aharonian, F. A. 2002, MNRAS, 332, 215

Alfvén, H. & Herlofson, N. 1950, Phys. Rev., 78, 616

Aloy, M. A., Ibáñez, J. M. ., Martí, J. M. ., Gómez, J.-L., & Müller, E. 1999, ApJ, 523, L125

Amato, E. & Arons, J. 2006, ApJ, 653, 325

Atoyan, A. & Dermer, C. D. 2004, ApJ, 613, 151

Baade, W. 1956, ApJ, 123, 550

Baade, W. & Minkowski, R. 1954, ApJ, 119, 215

Bahcall, N. A. & Chokshi, A. 1992, ApJ, 385, L33

Bałucińska-Church, M., Ostrowski, M., Stawarz, ł., & Church, M. J. 2005, MNRAS, 357, L6

Begelman, M. C., Blandford, R. D., & Rees, M. J. 1984, Reviews of Modern Physics, 56, 255

Belsole, E., Worrall, D. M., & Hardcastle, M. J. 2006, MNRAS, 366, 339

Bennett, A. S. 1962, MmRAS, 68, 163

Best, P. N., Kauffmann, G., Heckman, T. M., Brinchmann, J., Charlot, S., Ivezić, Ž., & White, S. D. M. 2005, MNRAS, 362, 25

Best, P. N., von der Linden, A., Kauffmann, G., Heckman, T. M., & Kaiser, C. R. 2007, MNRAS, 379, 894

Bicknell, G. V. 1994, ApJ, 422, 542

—. 1995, ApJS, 101, 29

Bicknell, G. V. & Begelman, M. C. 1996, ApJ, 467, 597

Blandford, R. D. & Koenigl, A. 1979, Astrophys. Lett., 20, 15

Blandford, R. D. & Rees, M. J. 1974, MNRAS, 169, 395

Blewett, J. P. 1946, Phys. Rev., 69, 87

—. 1998, Journal of Synchrotron Radiation, 5, 135

Blumenthal, G. R. & Gould, R. J. 1970, Reviews of Modern Physics, 42, 237

Blundell, K. M., Fabian, A. C., Crawford, C. S., Erlund, M. C., & Celotti, A. 2006, ApJ, 644, L13

Bolton, J. G. & Stanley, G. J. 1948, Australian Journal of Scientific Research A Physical Sciences, 1, 58

Bolton, J. G., Stanley, G. J., & Slee, O. B. 1949, Nature, 164, 101

Bridle, A. H., Fomalont, E. B., Byrd, G. G., & Valtonen, M. J. 1989, AJ, 97, 674

Bridle, A. H., Hough, D. H., Lonsdale, C. J., Burns, J. O., & Laing, R. A. 1994, AJ, 108, 766

Bridle, A. H., Perley, R. A., & Henriksen, R. N. 1986, AJ, 92, 534

Brunetti, G. 2000, Astroparticle Physics, 13, 107

Brunetti, G., Bondi, M., Comastri, A., & Setti, G. 2002, A&A, 381, 795

Brunetti, G., Mack, K.-H., Prieto, M. A., & Varano, S. 2003, MNRAS, 345, L40

Burbidge, G. R. 1956, ApJ, 124, 416

Cai, Z., Nan, R., Schilizzi, R. T., Miley, G. K., Bremer, M. A. R., van Dam, B., Röttgering, H. J. A., Liang, H., Chambers, K. C., Gurvits, L. I., & Zhang, H. Y. 2002, A&A, 381, 401

Campbell-Wilson, D. & Hunstead, R. W. 1994, Proceedings of the Astronomical Society of Australia, 11, 33

Carilli, C. L., Dreher, J. W., Perley, R. A., Leahy, P., & Muxlow, T. 1988, in Bulletin of the American Astronomical Society, Vol. 20, Bulletin of the American Astronomical Society, 734–+

Carilli, C. L., Kurk, J. D., van der Werf, P. P., Perley, R. A., & Miley, G. K. 1999, AJ, 118, 2581

Carilli, C. L., Perley, R. A., Dreher, J. W., & Leahy, J. P. 1991, ApJ, 383, 554

Celotti, A. 2003, Ap&SS, 288, 175

Celotti, A., Ghisellini, G., & Chiaberge, M. 2001, MNRAS, 321, L1

Chartas, G., Worrall, D. M., Birkinshaw, M., Cresitello-Dittmar, M., Cui, W., Ghosh, K. K., Harris, D. E., Hooper, E. J., Jauncey, D. L., Kim, D.-W., Lovell, J., Mathur, S., Schwartz, D. A., Tingay, S. J., Virani, S. N., & Wilkes, B. J. 2000, ApJ, 542, 655

Cheung, C. C. 2004, ApJ, 600, L23

Cheung, C. C., Wardle, J. F. C., & Chen, T. 2005, ApJ, 628, 104

Choi, E., Wiita, P. J., & Ryu, D. 2007, ApJ, 655, 769

Clarke, D. A., Bridle, A. H., Burns, J. O., Perley, R. A., & Norman, M. L. 1992, ApJ, 385, 173

Coppi, P. S. & Blandford, R. D. 1990, MNRAS, 245, 453

Croston, J. H., Hardcastle, M. J., Harris, D. E., Belsole, E., Birkinshaw, M., & Worrall, D. M. 2005, ApJ, 626, 733

Curtis, H. D. 1918, Publications of Lick Observatory, 13, 55

De Young, D. S. 1972, ApJ, 177, 573

—. 2002, New Astronomy Review

de Young, D. S. 2002, The physics of extragalactic radio sources (The physics of extragalactic radio sources, by David S. De Young. Chicago, Ill. : University of Chicago Press, 2002.)

Dennett-Thorpe, J., Bridle, A. H., Scheuer, P. A. G., Laing, R. A., & Leahy, J. P. 1997, MNRAS, 289, 753

Dermer, C. D. 1995, ApJ, 446, L63+

Dermer, C. D. & Atoyan, A. M. 2002, ApJL, 568, L81

Dermer, C. D. & Schlickeiser, R. 1993, ApJ, 416, 458

Dickey, J. M. & Lockman, F. J. 1990, ARA&A, 28, 215

Dombrovsky, V. A. 1954, Doklady Acad. Sci. USSR, 94, 1021

Double, G. P., Baring, M. G., Jones, F. C., & Ellison, D. C. 2004, ApJ, 600, 485

Drury, L. O. 2004, Journal of Korean Astronomical Society, 37, 393

Edge, D. O., Shakeshaft, J. R., McAdam, W. B., Baldwin, J. E., & Archer, S. 1959, MmRAS, 68, 37

Eilek, J. A. & Hughes, P. A. 1991, Particle acceleration and magnetic field evolution, ed. P. A. Hughes, 428–+

Ekers, J. A. 1969, Australian Journal of Physics Astrophysical Supplement, 7, 3

Elder, F. R., Gurewitsch, A. M., Langmuir, R. V., & Pollock, H. C. 1947, Phys. Rev., 71, 829

Elder, F. R., Langmuir, R. V., & Pollock, H. C. 1948, Phys. Rev., 74, 52

Erlund, M. C., Fabian, A. C., & Blundell, K. M. 2008, MNRAS, 386, 1774

Fanaroff, B. L. & Riley, J. M. 1974, MNRAS, 167, 31P

Francis, P. J., Hewett, P. C., Foltz, C. B., Chaffee, F. H., Weymann, R. J., & Morris, S. L. 1991, ApJ, 373, 465

Gambill, J. K., Sambruna, R. M., Chartas, G., Cheung, C. C., Maraschi, L., Tavecchio, F., Urry, C. M., & Pesce, J. E. 2003, A&A, 401, 505

Gehrels, N. 1986, ApJ, 303, 336

Gelbord, J. M., Marshall, H. L., Worrall, D. M., Birkinshaw, M., Lovell, J. E. J., Ojha, R., Godfrey, L., Schwartz, D. A., Perlman, E. S., Georganopoulos, M., Murphy, D. W., & Jauncey, D. L. 2005, ApJ, 632, L75

Georganopoulos, M. & Kazanas, D. 2003, ApJ, 589, L5

—. 2004, ApJ, 604, L81

Georganopoulos, M., Kirk, J. G., & Mastichiadis, A. 2001, ApJ, 561, 111

Ghisellini, G. & Celotti, A. 2001, MNRAS, 327, 739

Gopal-Krishna, Biermann, P. L., & Wiita, P. J. 2004, ApJ, 603, L9

Gurvits, L. I., Schilizzi, R. T., Miley, G. K., Peck, A., Bremer, M. N., Roettgering, H., & van Breugel, W. 1997, A&A, 318, 11

Hardcastle, M. J. 2001, A&A, 373, 881

—. 2003, New Astronomy Review, 47, 649

Hardcastle, M. J., Alexander, P., Pooley, G. G., & Riley, J. M. 1998, MNRAS, 296, 445

—. 1999, MNRAS, 304, 135

Hardcastle, M. J., Birkinshaw, M., & Worrall, D. M. 2001, MNRAS, 323, L17

Hardcastle, M. J., Harris, D. E., Worrall, D. M., & Birkinshaw, M. 2004, ApJ, 612, 729

Hargrave, P. J. & Ryle, M. 1974, MNRAS, 166, 305

Harris, D. E., Carilli, C. L., & Perley, R. A. 1994, Nature, 367, 713

Harris, D. E. & Krawczynski, H. 2002, ApJ, 565, 244

—. 2006, ARA&A, 44, 463

Harris, D. E., Nulsen, P. E. J., Ponman, T. J., Bautz, M., Cameron, R. A., David, L. P., Donnelly, R. H., Forman, W. R., Grego, L., Hardcastle, M. J., Henry, J. P., Jones, C., Leahy, J. P., Markevitch, M., Martel, A. R., McNamara, B. R., Mazzotta, P., Tucker, W., Virani, S. N., & Vrtilek, J. 2000, ApJ, 530, L81

Heavens, A. F. & Meisenheimer, K. 1987, MNRAS, 225, 335

Heckman, T. M., Smith, E. P., Baum, S. A., van Breugel, W. J. M., Miley, G. K., Illingworth, G. D., Bothun, G. D., & Balick, B. 1986, ApJ, 311, 526

Hey, J. S., Parsons, S. J., & Phillips, J. W. 1946, Nature, 158, 234

Hill, G. J. & Lilly, S. J. 1991, ApJ, 367, 1

Hoshino, M., Arons, J., Gallant, Y. A., & Langdon, A. B. 1992, ApJ, 390, 454

Ishwara-Chandra, C. H. & Saikia, D. J. 2000, MNRAS, 317, 658

Jansky, K. G. 1932, Proc. IRE, 20, 1920

—. 1933, Nature, 132, 66

Jeyakumar, S. & Saikia, D. J. 2000, MNRAS, 311, 397

Jones, T. W. & Odell, S. L. 1977, A&A, 61, 291

Jorstad, S. G. & Marscher, A. P. 2004, ApJ, 614, 615

Kapahi, V. K. & Schilizzi, R. T. 1979, Nature, 277, 610

Kataoka, J. & Stawarz, Ł. 2005, ApJ, 622, 797

Kataoka, J., Stawarz, Ł., Harris, D. E., Siemiginowska, A., Ostrowski, M., Swain, M. R., Hardcastle, M. J., Goodger, J. L., Iwasawa, K., & Edwards, P. G. 2008, ApJ, 685, 839

Kennedy, J. F. & Keeping, E. S. 1951, The Distribution of the Standard Deviation, ed. N. J. Van Norstrand, 170–173

Kirk, J. G. & Duffy, P. 1999, Journal of Physics G Nuclear Physics, 25, 165

Komissarov, S. S. & Falle, S. A. E. G. Astronomical Society of the Pacific Conference Series, Vol. 100, , Energy Transport in Radio Galaxies and Quasars, ed. P. E. HardeeA. H. Bridle & J. A. Zensus, 327–+

Komissarov, S. S. & Falle, S. A. E. G. 1998, MNRAS, 297, 1087

Laing, R. in , Lecture Notes in Physics, Berlin Springer Verlag, Vol. 327, Hot Spots in Extragalactic Radio Sources, ed. K. MeisenheimerH.-J. Roeser, 27–43

Large, M. I., Mills, B. Y., Little, A. G., Crawford, D. F., & Sutton, J. M. 1981, MNRAS, 194, 693

Lazio, T. J. W., Cohen, A. S., Kassim, N. E., Perley, R. A., Erickson, W. C., Carilli, C. L., & Crane, P. C. 2006, ApJ, 642, L33

Leahy, J. P., Muxlow, T. W. B., & Stephens, P. W. 1989, MNRAS, 239, 401

Ledlow, M. J. & Owen, F. N. 1995a, AJ, 110, 1959

—. 1995b, AJ, 109, 853

—. 1996, AJ, 112, 9

Lienard, A. 1898, L'Eclairage Elec., 16, 5

Lind, K. R. & Blandford, R. D. 1985, ApJ, 295, 358

Linfield, R. P., Levy, G. S., Ulvestad, J. S., Edwards, C. D., Dinardo, S. J., Stavert, L. R., Ottenhoff, C. H., Whitney, A. R., Cappallo, R. J., Rogers, A. E. E., Hirabayashi, H., Morimoto, M., Inoue, M., Jauncey, D. L., & Nishimura, T. 1989, ApJ, 336, 1105

Liu, F. K. & Xie, G. Z. 1992, A&AS, 95, 249

Liu, F. K. & Zhang, Y. H. 2002, A&A, 381, 757

Lonsdale, C. J. & Barthel, P. D. 1998, AJ, 115, 895

Lovell, J. E. J. 1997, Publications of the Astronomical Society of Australia, 14, 290

Marscher, A. P. 1988, ApJ, 334, 552

Marshall, H. L., Harris, D. E., Grimes, J. P., Drake, J. J., Fruscione, A., Juda, M., Kraft, R. P., Mathur, S., Murray, S. S., Ogle, P. M., Pease, D. O., Schwartz, D. A., Siemiginowska, A. L., Vrtilek, S. D., & Wargelin, B. J. 2001, ApJ, 549, L167

Marshall, H. L., Jester, S., Harris, D. E., & Meisenheimer, K. 2006, in ESA Special Publication, Vol. 604, The X-ray Universe 2005, ed. A. Wilson, 643–+

Marshall, H. L., Schwartz, D. A., Lovell, J. E. J., Murphy, D. W., Worrall, D. M., Birkinshaw, M., Gelbord, J. M., Perlman, E. S., & Jauncey, D. L. 2005, ApJS, 156, 13

McLure, R. J., Kukula, M. J., Dunlop, J. S., Baum, S. A., O'Dea, C. P., & Hughes, D. H. 1999, MNRAS, 308, 377

McLure, R. J., Willott, C. J., Jarvis, M. J., Rawlings, S., Hill, G. J., Mitchell, E., Dunlop, J. S., & Wold, M. 2004, MNRAS, 351, 347

Mehta, K. T., Georganopoulos, M., Perlman, E. S., Padgett, C. A., & Chartas, G. 2008, ArXiv e-prints

Meier, D. L. 1999, ApJ, 522, 753

Meisenheimer, K. 2003, New Astronomy Review, 47, 495

Meisenheimer, K., Roser, H.-J., Hiltner, P. R., Yates, M. G., Longair, M. S., Chini, R., & Perley, R. A. 1989, A&A, 219, 63

Meisenheimer, K., Yates, M. G., & Roeser, H.-J. 1997, A&A, 325, 57

Miley, G. & De Breuck, C. 2008, A&A Rev., 15, 67

Miley, G. K., Hogg, D. E., & Basart, J. 1970, ApJ, 159, L19

Miller, N. A., Owen, F. N., Burns, J. O., Ledlow, M. J., & Voges, W. 1999, AJ, 118, 1988

Mueller, M. & Schwartz, D. A. 2008, ArXiv e-prints

Niemiec, J., Ostrowski, M., & Pohl, M. 2006, ApJ, 650, 1020

Norman, M. L. Astronomical Society of the Pacific Conference Series, Vol. 100, , Energy Transport in Radio Galaxies and Quasars, ed. P. E. HardeeA. H. Bridle & J. A. Zensus, 319–+

Owen, F. N. in , Lecture Notes in Physics, Berlin Springer Verlag, Vol. 421, Jets in Extragalactic Radio Sources, ed. H.-J. RöserK. Meisenheimer, 273–+

Owen, F. N. & Ledlow, M. J. Astronomical Society of the Pacific Conference Series, Vol. 54, , The Physics of Active Galaxies, ed. G. V. BicknellM. A. Dopita & P. J. Quinn, 319–+

Padovani, P., Perlman, E. S., Landt, H., Giommi, P., & Perri, M. 2003, ApJ, 588, 128

Perley, R. A. in , Lecture Notes in Physics, Berlin Springer Verlag, Vol. 327, Hot Spots in Extragalactic Radio Sources, ed. K. MeisenheimerH.-J. Roeser, 1–26

Perucho, M. & Martí, J. M. 2007, MNRAS, 382, 526

Prestage, R. M. & Peacock, J. A. 1988, MNRAS, 230, 131

Preston, R. A., Jauncey, D. L., Meier, D. L., Tzioumis, A. K., Ables, J., Batchelor, R., Faulkner, J., Gates, J., Greene, B., Hamilton, P. A., Harvey, B. R., Haynes, R. F., Johnson, B., Lambeck, K., Louie, A. P., McCulloch, P., Moorey, G., Morabito, D. D., Nicolson, G. D., Niell, A. E., Robertson, J. G., Royle, G. R., Skjerve, L., Slade, M. A., Slee, O. B., Stolz, A., Watkinson, A., Wehrle, A. E., & Wright, A. E. 1989, AJ, 98, 1

Prieto, M. A., Brunetti, G., & Mack, K.-H. 2002, Science, 298, 193

Rawlings, S. & Saunders, R. 1991, Nature, 349, 138

Rayner, D. P., Norris, R. P., & Sault, R. J. 2000, MNRAS, 319, 484

Reber, G. 1940, ApJ, 91, 621

—. 1944, ApJ, 100, 279

Rees, M. J. 1978, MNRAS, 184, 61P

Reynolds, J. 1994, ATNF Internal Report, AT/39.3/040

Reynolds, S. P. 1982, ApJ, 256, 38

Roeser, H.-J. & Meisenheimer, K. 1987, ApJ, 314, 70

Rybicki, G. B. & Lightman, A. P. 1979, Radiative processes in astrophysics (New York, Wiley-Interscience, 1979. 393 p.)

Safouris, V., Subrahmanyan, R., Bicknell, G. V., & Saripalli, L. 2008, MNRAS, 385, 2117

Sahayanathan, S. & Misra, R. 2005, ApJ, 628, 611

Sambruna, R. M., Gambill, J. K., Maraschi, L., Tavecchio, F., Cerutti, R., Cheung, C. C., Urry, C. M., & Chartas, G. 2004, ApJ, 608, 698

Sambruna, R. M., Maraschi, L., Tavecchio, F., Urry, C. M., Cheung, C. C., Chartas, G., Scarpa, R., & Gambill, J. K. 2002, ApJ, 571, 206

Sambruna, R. M., Urry, C. M., Tavecchio, F., Maraschi, L., Scarpa, R., Chartas, G., & Muxlow, T. 2001, ApJ, 549, L161

Sanders, R. H. 1983, ApJ, 266, 73

Saxton, C. J., Sutherland, R. S., Bicknell, G. V., Blanchet, G. F., & Wagner, S. J. 2002, A&A, 393, 765

Scheuer, P. A. G. 1974, MNRAS, 166, 513

Scheuer, P. A. G. & Williams, P. J. S. 1968, ARA&A, 6, 321

Schmidt, M. 1972, ApJ, 176, 289

Schott, G. A. 1912, Electromagnetic Radiation (Cambridge University Press)

Schreier, E. J., Feigelson, E., Delvaille, J., Giacconi, R., Grindlay, J., Schwartz, D. A., & Fabian, A. C. 1979, ApJ, 234, L39

Schwartz, D. A. 2002, ApJ, 569, L23

Schwartz, D. A., Marshall, H. L., Lovell, J. E. J., Murphy, D. W., Bicknell, G. V., Birkinshaw, M., Gelbord, J., Georganopoulos, M., Godfrey, L., Jauncey, D. L., Perlman, E. S., & Worrall, D. M. 2006, ApJ, 640, 592

Schwartz, D. A., Marshall, H. L., Lovell, J. E. J., Piner, B. G., Tingay, S. J., Birkinshaw, M., Chartas, G., Elvis, M., Feigelson, E. D., Ghosh, K. K., Harris, D. E., Hirabayashi, H., Hooper, E. J., Jauncey, D. L., Lanzetta, K. M., Mathur, S., Preston, R. A., Tucker, W. H., Virani, S., Wilkes, B., & Worrall, D. M. 2000, ApJ, 540, L69+

Seymour, N., Stern, D., De Breuck, C., Vernet, J., Rettura, A., Dickinson, M., Dey, A., Eisenhardt, P., Fosbury, R., Lacy, M., McCarthy, P., Miley, G., Rocca-Volmerange, B., Röttgering, H., Stanford, S. A., Teplitz, H., van Breugel, W., & Zirm, A. 2007, ApJS, 171, 353

Shabala, S. S., Ash, S., Alexander, P., & Riley, J. M. 2008, MNRAS, 388, 625

Shepherd, M. C. in , Astronomical Society of the Pacific Conference Series, Vol. 125, Astronomical Data Analysis Software and Systems VI, ed. G. HuntH. Payne, 77–+

Shields, G. A. 1999, PASP, 111, 661

Siemiginowska, A., Bechtold, J., Aldcroft, T. L., Elvis, M., Harris, D. E., & Dobrzycki, A. 2002, ApJ, 570, 543

Siemiginowska, A., Stanghellini, C., Brunetti, G., Fiore, F., Aldcroft, T. L., Bechtold, J., Elvis, M., Murray, S. S., Antonelli, L. A., & Colafrancesco, S. 2003, ApJ, 595, 643

Siemiginowska, A., Stawarz, Ł., Cheung, C. C., Harris, D. E., Sikora, M., Aldcroft, T. L., & Bechtold, J. 2007, ApJ, 657, 145

Sirianni, M., Jee, M. J., Benítez, N., Blakeslee, J. P., Martel, A. R., Meurer, G., Clampin, M., De Marchi, G., Ford, H. C., Gilliland, R., Hartig, G. F., Illingworth, G. D., Mack, J., & McCann, W. J. 2005, PASP, 117, 1049

Spitkovsky, A. 2008, ApJ, 673, L39

Stawarz, L. 2003, Chinese Journal of Astronomy and Astrophysics Supplement, 3, 383

Stawarz, Ł., Cheung, C. C., Harris, D. E., & Ostrowski, M. 2007, ApJ, 662, 213

Stawarz, Ł. & Ostrowski, M. 2002, ApJ, 578, 763

Stawarz, Ł., Sikora, M., Ostrowski, M., & Begelman, M. C. 2004, ApJ, 608, 95

Swain, M. R., Bridle, A. H., & Baum, S. A. 1998, ApJ, 507, L29

Tavecchio, F., Cerutti, R., Maraschi, L., Sambruna, R. M., Gambill, J. K., Cheung, C. C., & Urry, C. M. 2005, ApJ, 630, 721

Tavecchio, F., Ghisellini, G., & Celotti, A. 2003, A&A, 403, 83

Tavecchio, F., Maraschi, L., Ghisellini, G., Celotti, A., Chiappetti, L., Comastri, A., Fossati, G., Grandi, P., Pian, E., Tagliaferri, G., Treves, A., Raiteri, C. M., Sambruna, R., & Villata, M. 2000a, ApJ, 543, 535

Tavecchio, F., Maraschi, L., Sambruna, R. M., & Urry, C. M. 2000b, ApJ, 544, L23

Taylor, G. B., Carilli, C. L., & Perley, R. A., eds. 1999, Astronomical Society of the Pacific Conference Series, Vol. 180, Synthesis Imaging in Radio Astronomy II

Taylor, G. B. & Perley, R. A. 1992, A&A, 262, 417

Tingay, S. J., Lenc, E., Brunetti, G., & Bondi, M. 2008, AJ, 136, 2473

Tregillis, I. L., Jones, T. W., & Ryu, D. 2001, ApJ, 557, 475

Tsang, O. & Kirk, J. G. 2007, A&A, 463, 145

Uchiyama, Y., Urry, C. M., Van Duyne, J., Cheung, C. C., Sambruna, R. M., Takahashi, T., Tavecchio, F., & Maraschi, L. 2005, ApJ, 631, L113

Urry, C. M. & Padovani, P. 1995, PASP, 107, 803

Vlahakis, N. & Königl, A. 2004, ApJ, 605, 656

Wardle, J. F. C. 1977, Nature, 269, 563

Wardle, J. F. C. & Aaron, S. E. 1997, MNRAS, 286, 425

Wardle, J. F. C., Gobielle, D., & Cheung, C. C. 2008

Wardle, J. F. C., Homan, D. C., Ojha, R., & Roberts, D. H. 1998, Nature, 395, 457

Wills, B. J. 1975, Australian Journal of Physics Astrophysical Supplement, 38, 1

Worrall, D. M. & Birkinshaw, M. 2006, in Lecture Notes in Physics, Berlin Springer Verlag, Vol. 693, Physics of Active Galactic Nuclei at all Scales, ed. D. Alloin, 39

Worrall, D. M., Birkinshaw, M., & Hardcastle, M. J. 2001, MNRAS, 326, L7

Young, A. J., Wilson, A. S., Tingay, S. J., & Heinz, S. 2005, ApJ, 622, 830

Zensus, J. A., Diamond, P. J., & Napier, P. J., eds. 1995, Astronomical Society of the Pacific Conference Series, Vol. 82, Very Long Baseline Interferometry and the VLBA

Zirbel, E. L. 1997, ApJ, 476, 489